



Numerical and experimental studies of high-temperature superconducting systems

by

© **Bradley D. E. McNiven**

A thesis submitted to the School of Graduate Studies in partial fulfillment of the requirements for the degree of Doctor of Philosophy.

Department of Physics & Physical Oceanography
Memorial University

March 2024

St. John's, Newfoundland and Labrador, Canada

Abstract

The objective of this thesis is to study the correlated behaviour of electron and lattice dynamics in the high-temperature cuprate superconductors. In particular, we are interested in the lattice (i.e., structural and phonon) and electronic dynamics in these systems and how they may influence the driving mechanisms of high- T_c superconductivity. We do this through two methods: numerical calculations on the two-dimensional Hubbard model and inelastic light scattering experiments.

For the numerical component of this work, we compute the static and dynamical longitudinal charge and spin susceptibilities as functions of real frequency on a two-dimensional square lattice with weak-coupling for the $t - t' - U$ Hubbard model via a perturbative, diagrammatic approach. In the static case, the spin susceptibility is dominated by $q = (\pi, \pi)$ spin fluctuations that are largest near half-filling, while the charge susceptibility has a clear multi-peak structure with a minimum located at the van Hove singularity of the non-interacting dispersion, a feature not observed in the commonly employed random-phase approximation. For dynamical charge and spin susceptibilities, we plot the dispersion for each respective collective electronic excitation on the real frequency axis. These excitations were found to split into separate modes surrounding the van Hove singularity, only to merge again in the long-wavelength limit. From an experimental standpoint, these results will prove useful for those studying electronic excitations as our calculations indicate that electron doped cuprates should be probed at higher energies in order to detect spin and charge excitations in comparison to the hole doped cuprates.

For the experimental aspect of this work, we study the single-crystal $\text{Bi}_2\text{Sr}_2\text{CaCu}_2\text{O}_{8+\delta}$ (Bi-2212) cuprate by Brillouin light scattering spectroscopy at room-temperature. We study the acoustic phonon behaviour in the normal state and gain further information on the structural dynamics which currently remain unresolved. From spectra

collected with an excitation source of 532 nm, we identify the Rayleigh surface mode, a longitudinal resonance mode, and six bulk acoustic modes (four quasi-transverse and two quasi-longitudinal), contrary to the typically expected three. From bulk spectral peaks, the extracted frequency shift and linewidth were used to determine the optical extinction coefficient-to-refractive index ratios. These ratios were subsequently used to obtain the extinction coefficient, penetration depth, optical absorption coefficient, and complex dielectric function, and were found to be 5 – 7 times larger than those obtained from optical interference measurements.

The number of bulk modes observed in the Brillouin data suggests Bi-2212 is an incommensurate composite crystal consisting of two weakly interacting sublattices. Further analysis of the Brillouin data allows us to assign the two independent sublattices as $\text{Bi}_2\text{Sr}_2\text{O}_4$ and CaCu_2O_4 , calculate the hypersound velocity of the observed surface and bulk acoustic phonon modes, and derive an expression relating the bulk crystals longitudinal acoustic phonon velocity to the bulk longitudinal acoustic phonon velocities corresponding to the two sublattices. Finally, we determined the elastic constants C_{11} , C_{22} , C_{33} , C_{44} , C_{55} , C_{12} , and C_{23} and related sublattice elastic constants.

Overall, the utility of the experimental work presented in this thesis is multi-fold. Firstly, it has refined the acoustic phonon velocities, and subsequently the elastic constants, of Bi-2212 which have received little attention. Secondly, our derived expression relating the bulk and sublattice longitudinal velocities will aid in expanding upon the model of incommensurate composite crystals and the study incommensurate crystallography in general. Lastly, and most importantly, our experimental verification that Bi-2212 is comprised of two interacting sublattices alludes to a highly non-trivial optic phonon structure and the existence of low-lying optic phonon modes. Identification of such modes may play an important role in understanding the driving mechanisms surrounding high- T_c superconductivity.

Acknowledgements

I would first and foremost like to extend a major thank you to my supervisors Dr. Todd Andrews and Dr. James LeBlanc at Memorial University who have provided their continuous support, encouragement, and direction over the course of my PhD studies. The quality of this work and my experience as a graduate student would not have been the same without them. I also offer another sincere thank you to Dr. Maynard Clouter for providing on-going assistance on spectroscopy and experimental apparatus related matters. I also acknowledge Dr. Dillon Hanlon and Stephen Spencer in the Andrew's research group.

At McMaster University, I would like to thank Dr. Pat Clancy for providing the samples used in this work. I would also like to thank Pat, along with Dr. Bruce Gaulin and Dr. Qiang Chen, for their hospitality when I visited McMaster University during my PhD studies.

I would like to thank my parents, Mike and Debbie, and my brother Ryan for their continuous support and encouragement throughout the years.

Lastly, I want to thank my fiancée Olivia Dutton for everything you do, and our animals; Jovie, Juno, Milton, Doris, and the late Lincoln, for their constant company during the late work nights over the past four years. I love you all immensely.

Statement of contribution

This document is a sandwich-style thesis comprised of four peer-reviewed manuscripts. Two works are published in Physical Review B: (1) "One- and two-particle properties of the weakly interacting two-dimensional Hubbard model in proximity to the van Hove singularity" (2022), and (2) "Long-wavelength phonon dynamics in incommensurate $\text{Bi}_2\text{Sr}_2\text{CaCu}_2\text{O}_{8+\delta}$ crystals by Brillouin light scattering spectroscopy" (2022). The manuscript (3) "Optical constants of crystalline $\text{Bi}_2\text{Sr}_2\text{CaCu}_2\text{O}_{8+\delta}$ by Brillouin light scattering spectroscopy" (2021) is published in Superconductor Science and Technology, while (4) "Influence of incommensurate structure on the elastic constants of crystalline $\text{Bi}_2\text{Sr}_2\text{CaCu}_2\text{O}_{8+\delta}$ by Brillouin light scattering spectroscopy" (2023) resides in Materials Research Express.

Bradley D. E. McNiven was the sole author of this thesis. He was lead contributor in the above mentioned peer-reviewed manuscripts (i.e., data collection, data analysis, and manuscript writing), and chose the scientific problems addressed in these works. Sharing authorship in these works are his project supervisors Dr. James P. F. LeBlanc and Dr. G. Todd Andrews. Dr. LeBlanc provided computational resources and guidance toward fine-tuning computational project ideas related to the main experimental work. Dr. Andrews provided access to all experimental equipment necessary for the completion of this work.

Also sharing co-authorship in (1) is Dr. Hanna Terletska who contributed to the formulation of this particular project and finalizing revisions after journal referee feedback.

Contents

Title page	i
Abstract	ii
Acknowledgements	iv
Statement of contribution	v
Contents	vi
List of Tables	ix
List of Tables	ix
List of Figures	x
List of Figures	x
1 Introduction	1
1.1 A brief history on superconductivity	1
1.2 Type-I and type-II superconductors	4
1.3 An overview on cuprates	5
1.3.1 Cuprate phase diagram	7
1.3.2 Bi-2212	9

1.4	Present work	11
	Bibliography	13
2	Numerical Studies	16
2.1	Hubbard model	16
2.2	Relevant observables	18
2.2.1	Green's function	18
2.2.2	Longitudinal susceptibility functions	26
2.3	Algorithmic Matsubara Integration	28
	Bibliography	30
3	Numerical publication	32
3.1	One- and two-particle properties of the weakly interacting two-dimensional Hubbard model in proximity to the van Hove singularity	32
4	Experimental studies on Bi-2212	46
4.1	Phonons	46
4.2	Inelastic light scattering	48
4.2.1	Brillouin light scattering spectroscopy	50
4.3	Elastic theory in solids	53
4.3.1	Rayleigh surface velocity and elastic constants	57
4.4	Aperiodic crystallography	57
4.5	Acoustic phonons & elastic constants of Bi-2212	61
4.5.1	Brillouin light scattering measurements	61
4.5.2	Ultrasonic measurements	62
4.5.3	Inelastic neutron scattering measurements	64
4.6	Bi-2212 Samples	64
4.7	Brillouin scattering apparatus	65

Bibliography	68
5 Experimental publications	71
5.1 Optical constants of crystalline $\text{Bi}_2\text{Sr}_2\text{CaCu}_2\text{O}_{8+\delta}$ by Brillouin light scattering spectroscopy	71
5.2 Long-wavelength phonon dynamics in incommensurate $\text{Bi}_2\text{Sr}_2\text{CaCu}_2\text{O}_{8+\delta}$ crystals by Brillouin light scattering spectroscopy	76
5.3 Influence of incommensurate structure on the elastic constants of crystalline $\text{Bi}_2\text{Sr}_2\text{CaCu}_2\text{O}_{8+\delta}$ by Brillouin light scattering spectroscopy . . .	86
6 Conclusion	96

List of Tables

1.1	Overview on select cuprates shown in Fig. 1.3. Tabulated data includes each materials stoichiometry, critical temperature (T_c) at ambient pressure, and number of CuO_2 planes per unit cell (N_p). Data compiled from Refs. [8, 16, 20–24].	6
4.1	Bulk acoustic phonon velocities and the derived elastic constant quantity for a given phonon propagation direction for a crystal with orthorhombic symmetry.	55
4.2	Bulk acoustic phonon velocities and the derived elastic constant quantity for a given phonon propagation direction for a crystal with tetragonal symmetry.	56
4.3	Elastic constants and identifying subscripts (i, j, k) in Eq. 4.31 for particular directions and planes of phonon propagation.	57

List of Figures

1.1	Schematic depiction of the external magnetic field lines described by the Meissner effect when the temperature is (a) greater and (b) less than the critical temperature (T_c) of the superconducting material. . . .	1
1.2	Simple schematic of the BCS theory of superconductivity. (a) An electron travels through a lattice of positively charged ions. (b) Ions are displaced by their attraction to the moving electron resulting in a region of positive charge density. (c) A second electron is attracted to the region of positive charge density. These electrons are now coupled to one another as a Cooper pair.	2
1.3	Chronology of the discovery of notable superconductors and their measured T_c at atmospheric pressure. Also shown are select high-pressure superconductors along with the boiling points of liquid Nitrogen, Helium, and Hydrogen. Data compiled from Refs. [7–14].	3
1.4	Phase diagram of conventional and unconventional superconductors in the $H - T$ plane. Type-II inset depicts the magnetic flux lines (black) resulting supercurrents (red) in the bulk of the superconducting material. T_c - critical temperature, H_c - critical magnetic fields, H_i - internal magnetic field.	5
1.5	Schematic of the ABX_3 perovskite structure. A - metal cation, B,X - nonmetal anion.	6
1.6	Schematic of the hole-doped cuprate phase diagram showing the five main phases.	8

1.7	Schematic depicting the electrical resistivity as a function of temperature in the pseudogap and non-pseudogap phases. In the pseudogap phase, the resistivity until the onset of superconductivity, while in the non-pseudogap phases the decrease in resistivity is non-linear. T_c - critical temperature, T_p - pseudogap temperature.	9
1.8	Simplified schematic depicting the unit cell of Bi-2212.	10
2.1	Schematic representation of a 2D square lattice. U - onsite Hubbard interaction for doubly occupied lattice site, t (t') nearest (next-nearest) neighbor hopping amplitude of a given electron moving lattice sites. . .	17
2.2	The six resulting first order Green's function diagrams from the perturbative expansion derived in Eqn. 2.23.	23
2.3	Contributing diagrams for $m = 0 - 2$ in the Green's function expansion derived in Eqn. 2.23. R - reducible, IR - irreducible.	24
2.4	The first few diagrams in the perturbative expansions of $\chi_{\uparrow\uparrow}$ and $\chi_{\uparrow\downarrow}$, as seen in Ref. [7].	27
2.5	Workflow of the AMI routine used in the numerical portion of this work.	29
4.1	Linear diatomic chain of two distinguishable atoms, each with a respective mass of M_1 and M_2 and uniform spring constant K . Each atom is separated by distance a	46
4.2	Schematic of the phonon dispersion curve confined to region where the acoustic branch is approximately linear.	48
4.3	Schematic depicting a typical spectrum due to phonons for a typical crystalline solid for an inelastic light scattering experiment. T - bulk transverse acoustic, L - bulk longitudinal acoustic.	49
4.4	Schematic depicting the scattering process of incident photons with thermally excited acoustic phonons in a solid. k - photon wavevector, q - phonon wavevector, ω - photon frequency, Ω - phonon angular frequency, θ - external angle, θ' - internal angle, n - refractive index of the solid, R - Rayleigh surface mode, B - bulk acoustic phonon mode, i - incident, s - scattered.	51

4.5	Schematic depicting the lattice system of a (a) commensurate (periodic) crystal, (b) incommensurate modulated crystal, and (c) incommensurate composite crystal.	59
4.6	Schematic depicting the acoustic phonon dispersion along a general direction of an incommensurate composite system consisting of two sublattices. Dashed lines indicate branch crossing regions. q_c - crossover wavevector, LA - longitudinal acoustic phonon branch, TA - transverse acoustic phonon branches.	60
4.7	Parent Bi-2212 samples with (a) $T_c = 78$ K and (b) $T_c = 91$ K. Note $T_c = 90$ K is not shown as it is nearly identical in appearance and dimension to the $T_c = 91$ K parent crystal. Original images are found in Ref. [39].	65
4.8	Schematic depicting the Brillouin light scattering apparatus used in this work.	66
4.9	Schematic depicting the six-pass tandem Fabry Perot inteferometer used in this work.	67

Chapter 1

Introduction

1.1 A brief history on superconductivity

Since Heike Kamerlingh Onnes's 1911 groundbreaking work showed the electrical resistance of pure mercury dissipates to zero at a critical temperature (T_c) of just 4.2 K [1, 2], physicists around the globe have been interested in this phenomena now known as superconductivity. After the discovery this superconducting state in mercury, other pure metals were studied at cryogenic temperatures, where lead was also found to have superconducting state at a slightly higher T_c (~ 6 K [1]).

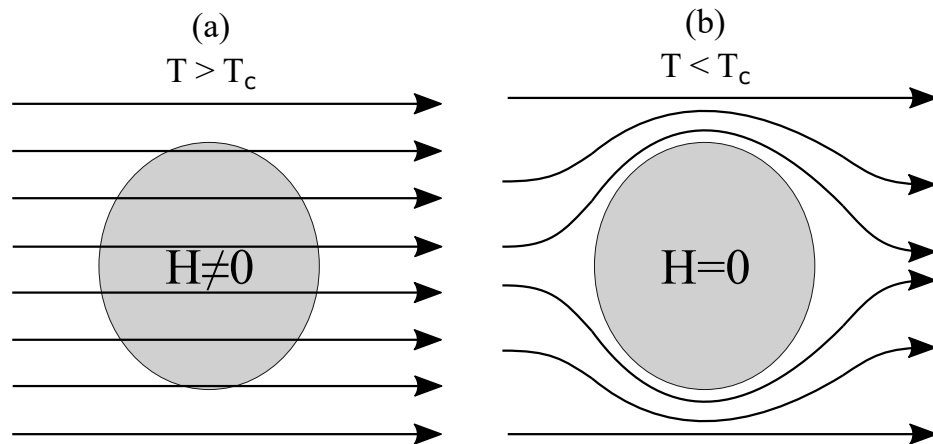


Figure 1.1: Schematic depiction of the external magnetic field lines described by the Meissner effect when the temperature is (a) greater and (b) less than the critical temperature (T_c) of the superconducting material.

The next monumental discovery of superconductivity occurred in 1933, where Walther Meissner and Robert Ochsenfeld showed superconductors exhibit superdiamagnetism [3], an outcome of the materials magnetic susceptibility equaling -1 at a critical magnetic field H_c . Now referred to as the Meissner effect, this result means that the magnetic field inside the material will be zero due to the magnetic flux lines being expelled from the material in a superconducting state. This is demonstrated in Fig. 1.1.

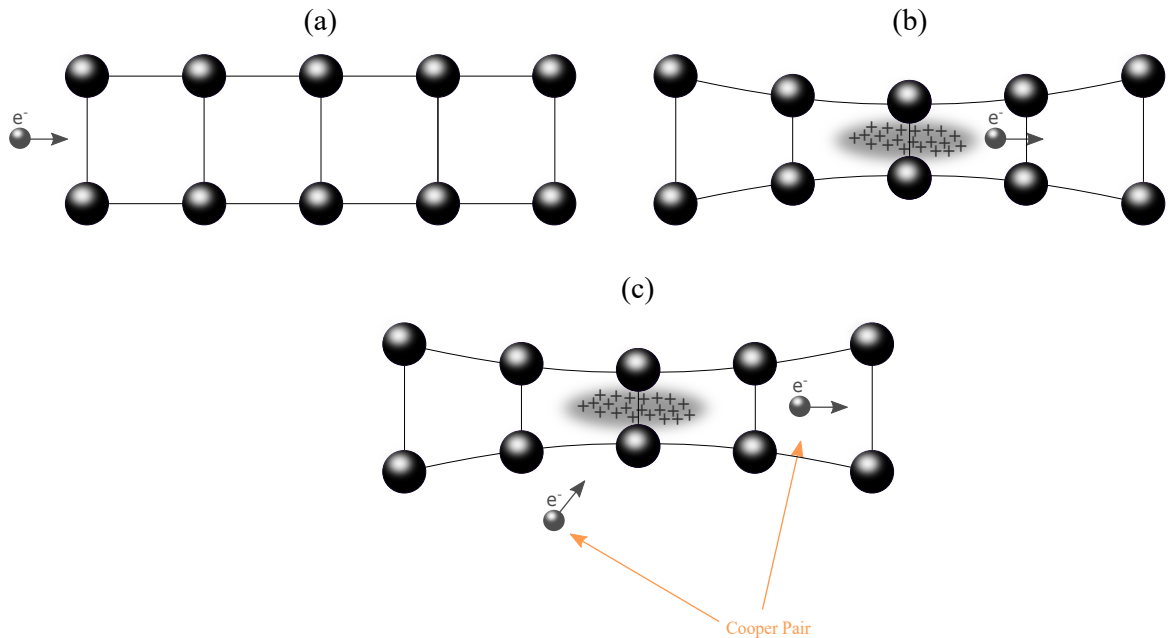


Figure 1.2: Simple schematic of the BCS theory of superconductivity. (a) An electron travels through a lattice of positively charged ions. (b) Ions are displaced by their attraction to the moving electron resulting in a region of positive charge density. (c) A second electron is attracted to the region of positive charge density. These electrons are now coupled to one another as a Cooper pair.

While superconductivity and the closely related Meissner effect were now known, the underlying mechanisms responsible for superconductivity remained unknown. This however was resolved in 1957, when the first microscopic theory of superconductivity was presented by John Bardeen, Leon Cooper, and John Robert Schrieffer and is now known as BCS theory [4, 5]. In Fig. 1.2, we describe this quantum mechanical model in a series of semi-classical pictures. As shown in panel (a), we show an electron travelling through a two-dimensional (2D) lattice system consisting of positively charged ions. As the electron passes through the lattice, as shown in panel (b), the ions are displaced from their equilibrium position due to their attraction to the electron, resulting in a

region of positive charge density. While the mass of an ion is much larger when compared to an electron, the time it takes to return to the equilibrium position is much longer than that of the electron to move through the system. This means the region of positive charge density resides in the system long enough to attract a second propagating electron, which then begins to follow the first electron as it continuously leaves a trail of positive charge density behind it (see panel (c)). When near the Fermi level, these two electrons are now coupled to one another by these lattice vibrations, and if the two electrons have opposite spin, will combine to form what is referred to as a Cooper pair. Cooper pairs will behave as an integer spin, meaning that the Cooper pairs present in a superconducting state will collectively act as a Bose-Einstein condensate. As a condensate, raising the energy above the Fermi level will simultaneously break all Cooper pairs and thus below the Fermi level the condensate will not encounter the same electrical resistance as individual electrons. In fact, the condensate experiences zero electrical resistance, a key defining feature of a superconducting state, due to the production of a gap in the energy spectrum [6].

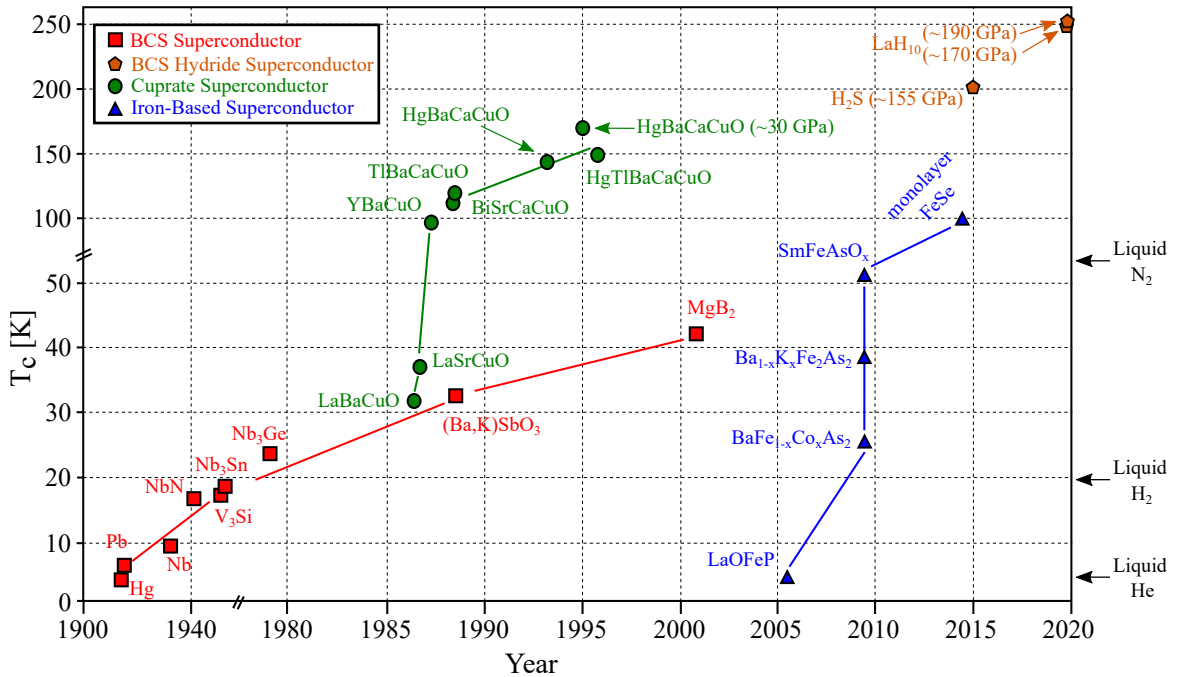


Figure 1.3: Chronology of the discovery of notable superconductors and their measured T_c at atmospheric pressure. Also shown are select high-pressure superconductors along with the boiling points of liquid Nitrogen, Helium, and Hydrogen. Data compiled from Refs. [7–14].

At this time in the 1960s, BCS theory indicated the critical temperature of conventional metals must be $T_c \lesssim 30$ K [15], with experimental data largely corroborating this (see Fig. 1.3). This notion, however, was proven false in 1986, when Johannes G. Bednorz and K. Alex Müller synthesized the inorganic ceramic $\text{La}_{1.85}\text{Ba}_{0.15}\text{CuO}_4$ (referred to as LBCO), which was found to have a critical temperature of 35 K [16]. This monumental discovery prompted a flurry of interest and questions surrounding superconductivity, as LBCO did not fit into the BCS theory. Over the next decade, several other copper-oxide based superconducting materials, known as cuprates, were successfully synthesized, each with a T_c far-surpassing both the previously predicted limit of $T_c \lesssim 30$ K and the T_c of known BCS superconductors. As shown in Fig. 1.3, numerous superconducting materials have been synthesized to date, such as the class of iron-based superconductors, which also do not abide by the BCS theory of superconductivity, and the more recently discovered high-pressure BCS hydride superconductors.

1.2 Type-I and type-II superconductors

There are two types of superconductors; type-I and type-II. The largest distinction between both types resides in the internal magnetic field and is demonstrated in Fig. 1.4. As seen in the figure, Type-I superconductors have one pure superconducting state that expels all magnetic flux from its bulk (i.e., the Meissner effect described above) and are described by BCS theory. The critical magnetic field has a temperature dependence that is parabolic and can be described via a mean-field approach by [8]:

$$H_c = H_c(0) \left(1 - \left(\frac{T}{T_c} \right)^2 \right), \quad (1.1)$$

where $H(0)$ is the magnetic field at $T = 0$ K.

Conversely, type-II superconductors have two superconducting critical phases, each with an upper critical magnetic field defined as H_{c1} and H_{c2} . For $H < H_{c1}$, these materials behave in the same manner as type-I, with the inside magnetic field (H_i) equaling zero, while for the region $H_{c1} < H < H_{c2}$, a mixed state is present where $H_i \neq 0$ and BCS theory does not apply [8]. In this mixed state, magnetic field lines penetrate the bulk as quantized vortices and ultimately create shielding currents

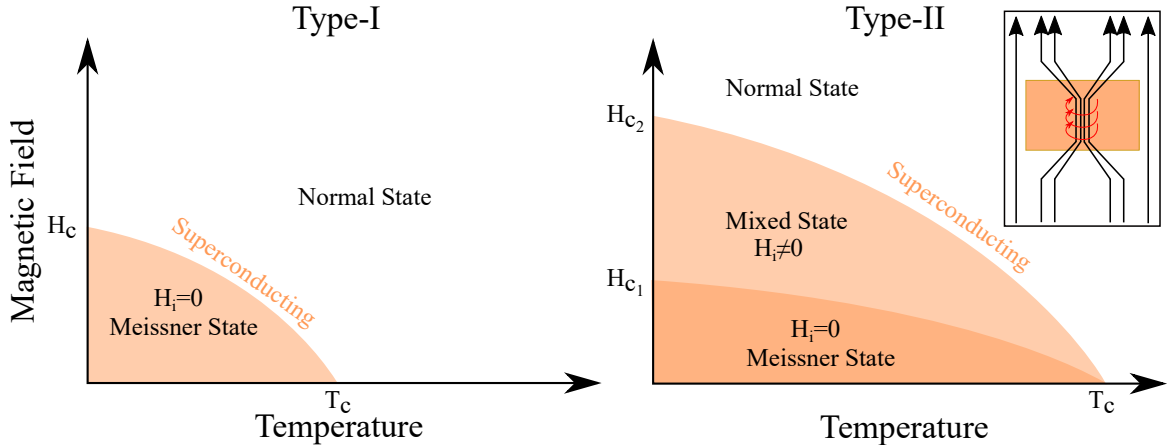


Figure 1.4: Phase diagram of conventional and unconventional superconductors in the $H - T$ plane. Type-II inset depicts the magnetic flux lines (black) resulting supercurrents (red) in the bulk of the superconducting material. T_c - critical temperature, H_c - critical magnetic fields, H_i - internal magnetic field.

which protect the bulk from the external and penetrating magnetic field lines [7] (see Type-II inset of Fig. 1.4). Cuprates have two superconducting phases and thus reside in the subclass of type-II superconductors.

1.3 An overview on cuprates

Cuprates are a group of layered high- T_c materials containing CuO_2 planes which play a substantial role in high- T_c superconductivity [17]. Cuprates have a general perovskite-like structure with the generalized formula ABX_3 , where A is a metal cation while B and X are nonmetal anions [8], with this structure shown in Fig. 1.5. Further, cuprates are highly anisotropic and have extremely complex structural effects [8], which we will discuss later in this thesis. While cuprates can have either an orthorhombic or tetragonal crystallographic structure, many of these compounds are simply referred to as pseudo-tetragonal due to their lattice constants being $a \approx b \neq c$ [18, 19].

Table 1.1 contains relevant data surrounding the high- T_c cuprates shown in Fig. 1.3. We include the general stoichiometry, structural phases commonly studied, and their respective T_c at atmospheric pressure. Also shown in the table are the the number of

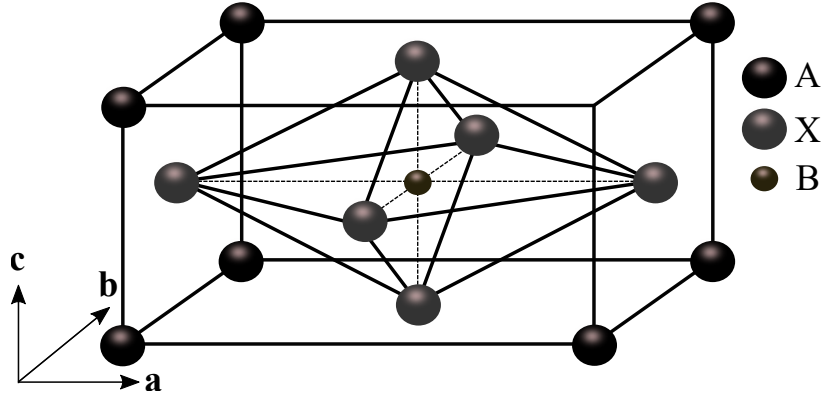


Figure 1.5: Schematic of the ABX_3 perovskite structure. A - metal cation, B,X - nonmetal anion.

Table 1.1: Overview on select cuprates shown in Fig. 1.3. Tabulated data includes each materials stoichiometry, critical temperature (T_c) at ambient pressure, and number of CuO_2 planes per unit cell (N_p). Data compiled from Refs. [8, 16, 20–24].

From Fig. 1.3	General Stoichiometry	Phase (Abbrev.)	T_c [K]	N_p
LaBaCuO	$\text{La}_{2-x}\text{Ba}_x\text{CuO}_4$	LBCO	35	1
LaSrCuO	$\text{La}_{2-x}\text{Sr}_x\text{CuO}_4$	LSCO	38	1
YBaCuO	$\text{YBa}_2\text{Cu}_3\text{O}_{7-\delta}$	YBCO	93	2
TlBaCaCuO	$\text{Tl}_2\text{Ba}_2\text{Ca}_{n-1}\text{Cu}_n\text{O}_{2n+4}$	$\text{Tl}_2\text{Ba}_2\text{CuO}_6$ (Tl-2201)	95	1
		$\text{Tl}_2\text{Ba}_2\text{CaCu}_2\text{O}_8$ (Tl-2212)	105	2
		$\text{Tl}_2\text{Ba}_2\text{Ca}_2\text{Cu}_3\text{O}_{10}$ (Tl-2223)	125	3
		$\text{TlBa}_2\text{Ca}_{n-1}\text{Cu}_n\text{O}_{2n+3}$	$\text{TlBa}_2\text{Ca}_3\text{Cu}_4\text{O}_{11}$ (Tl-1234)	122
BiSrCaCuO	$\text{Bi}_2\text{Sr}_2\text{Ca}_{n-1}\text{Cu}_n\text{O}_{2n+4+\delta}$	$\text{Bi}_2\text{Sr}_2\text{CuO}_{6+\delta}$ (Bi-2201)	12	1
		$\text{Bi}_2\text{Sr}_2\text{CaCu}_2\text{O}_{8+\delta}$ (Bi-2212)	95	2
		$\text{Bi}_2\text{Sr}_2\text{Ca}_2\text{Cu}_3\text{O}_{10+\delta}$ (Bi-2223)	110	3
HgBaCaCuO	$\text{HgBa}_2\text{Ca}_{n-1}\text{Cu}_n\text{O}_{2n+2+\delta}$	$\text{HgBa}_2\text{CuO}_{4+\delta}$ (Hg-1201)	98	1
		$\text{HgBa}_2\text{CaCu}_2\text{O}_{6+\delta}$ (Hg-1212)	128	2
		$\text{HgBa}_2\text{Ca}_2\text{Cu}_3\text{O}_{8+\delta}$ (Hg-1223)	135	3
HgTlBaCaCuO	$\text{Hg}_{0.8}\text{Tl}_{0.2}\text{Ba}_2\text{Ca}_2\text{Cu}_3\text{O}_{8+\delta}$	Hg(Tl)-1223	138	3

CuO_2 planes (N_p) contained in the unit cell of each compound. The relationship between T_c and the number of copper-oxide planes (N_p) remains an interesting question as T_c increases with increasing N_p and maximizes at when $N_p = 3$ [25].

1.3.1 Cuprate phase diagram

Cuprates are renowned for having a particularly rich phase diagram, where we show a simplified schematic in Fig. 1.6. Doping on the x-axis refers to oxygen doping per copper atom, with underdoped and overdoped referring to low and high oxygen content, respectively. It is noted that the introduction of oxygen dopants to cuprate systems results in hole-doped materials, which will be discussed in the following section.

As seen in the figure, cuprate compounds have a total of five main phases. Starting on the left-most side of the underdoped region is the antiferromagnetic phase. In this phase, all cuprates are insulating and exhibit antiferromagnetism over the approximate temperature range $0 \leq T \leq 300$ K.

In the lower half of Fig. 1.6, we show the superconducting phase which typically exists for doping levels between ~ 0.05 and ~ 0.27 . The point at which superconductivity occurs at the highest temperature is referred to as optimal doping and as shown in Table 1.1, ranges from ~ 90 K to ~ 130 K at atmospheric pressure for cuprates.

Next is the pseudogap phase, one of the defining characteristics of cuprate systems. This region exists for underdoped cuprates and is defined by an energy gap in the Fermi surface. While still not understood, the experimental observation of the deviation between the temperature dependence of several transport properties in underdoped cuprates compared to that of overdoped cuprates has been taken as support for the existence of the pseudogap phase.

An example of this is shown in Fig. 1.7, where we show a schematic of the resistivity as a function of temperature for partially underdoped and overdoped cuprates. For the overdoped case, resistivity decreases linearly until it drops to zero once the superconducting phase is reached [26–28], in which the resistivity drops to zero. In the case of underdoped cuprates, the resistivity drops linearly with decreasing temperature until the pseudogap phase is reached (T_p). For $T_c \leq T \leq T_p$, the decrease in resistivity is no longer linear, however, it drops to zero for $T \leq T_c$.

Furthermore, encompassing a significant percentage of phase space in the cuprate phase diagram are the strange metal and metallic regions. For the former case, this phase is not described by Fermi-liquid theory [29]. Conversely, the latter case is relatively understood as all strongly overdoped cuprates are weakly-correlated metals and thus are well described by Fermi-liquid theory.

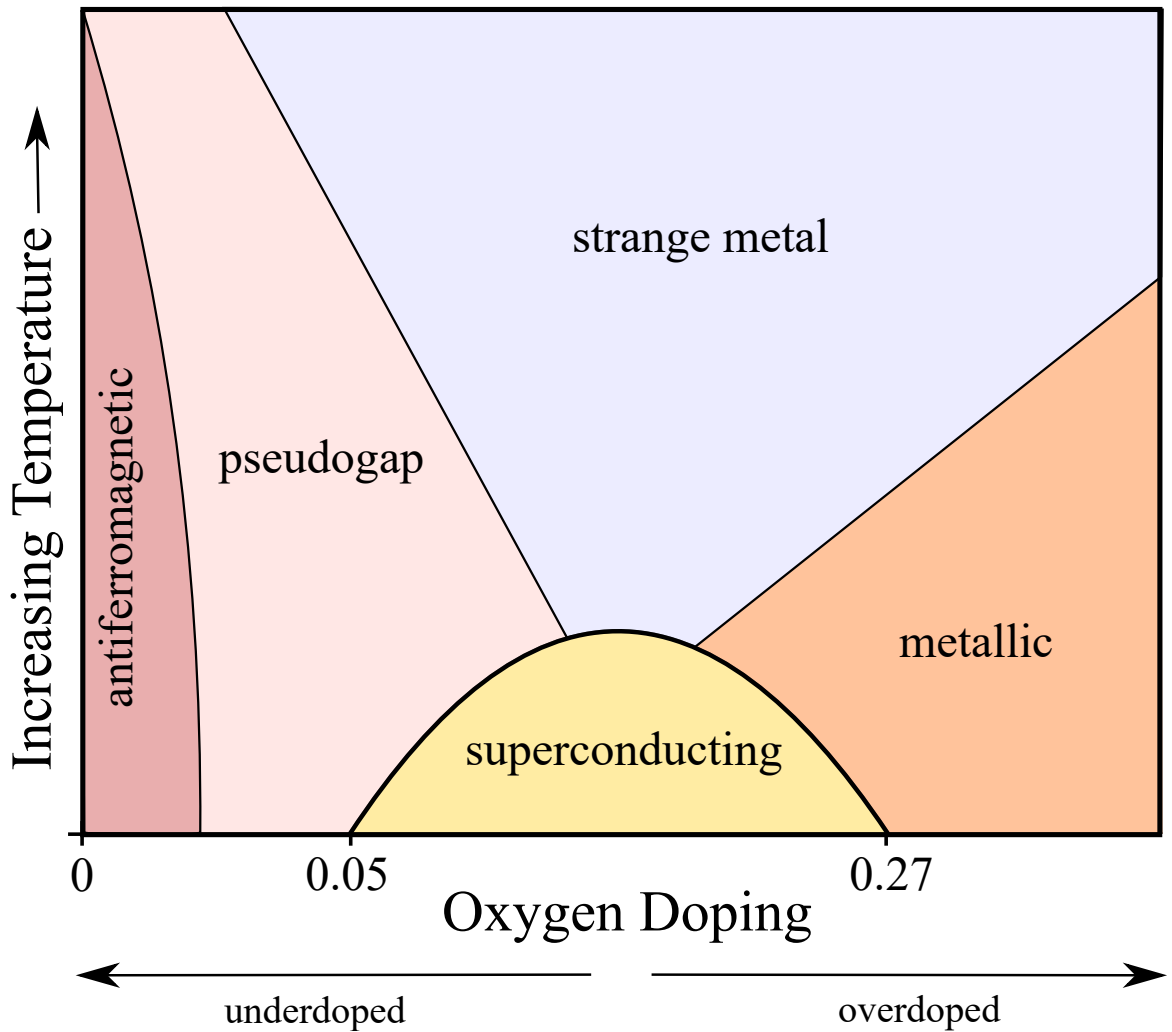


Figure 1.6: Schematic of the hole-doped cuprate phase diagram showing the five main phases.

While theoretical models such as the two-dimensional (2D) Hubbard model appear to encapsulate much of the physics contained in cuprate systems [30], the study of these materials experimentally is a significant challenge. Superconductivity in cuprates is largely dependent on the layered nature of their crystallographic structure [8], and given that these materials are influenced by their growth environment, and in some cases are unstable at atmospheric conditions, the resulting lattice defects and/or dopant atoms are able to alter their structural integrity. This can ultimately result in a drastic decrease or complete destruction of the superconducting phase. Furthermore, it is well known that cuprates are faced with significant grain boundary effects which can act as further impurities to the system [31].

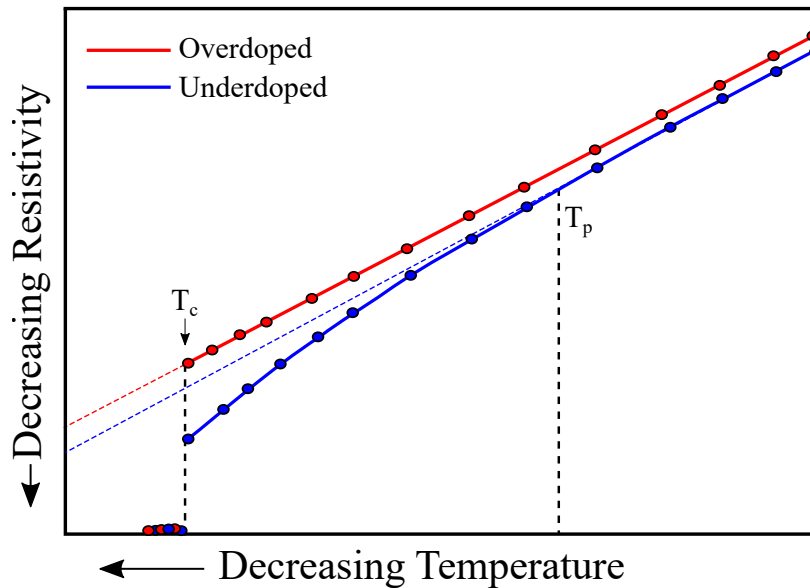


Figure 1.7: Schematic depicting the electrical resistivity as a function of temperature in the pseudogap and non-pseudogap phases. In the pseudogap phase, the resistivity until the onset of superconductivity, while in the non-pseudogap phases the decrease in resistivity is non-linear. T_c - critical temperature, T_p - pseudogap temperature.

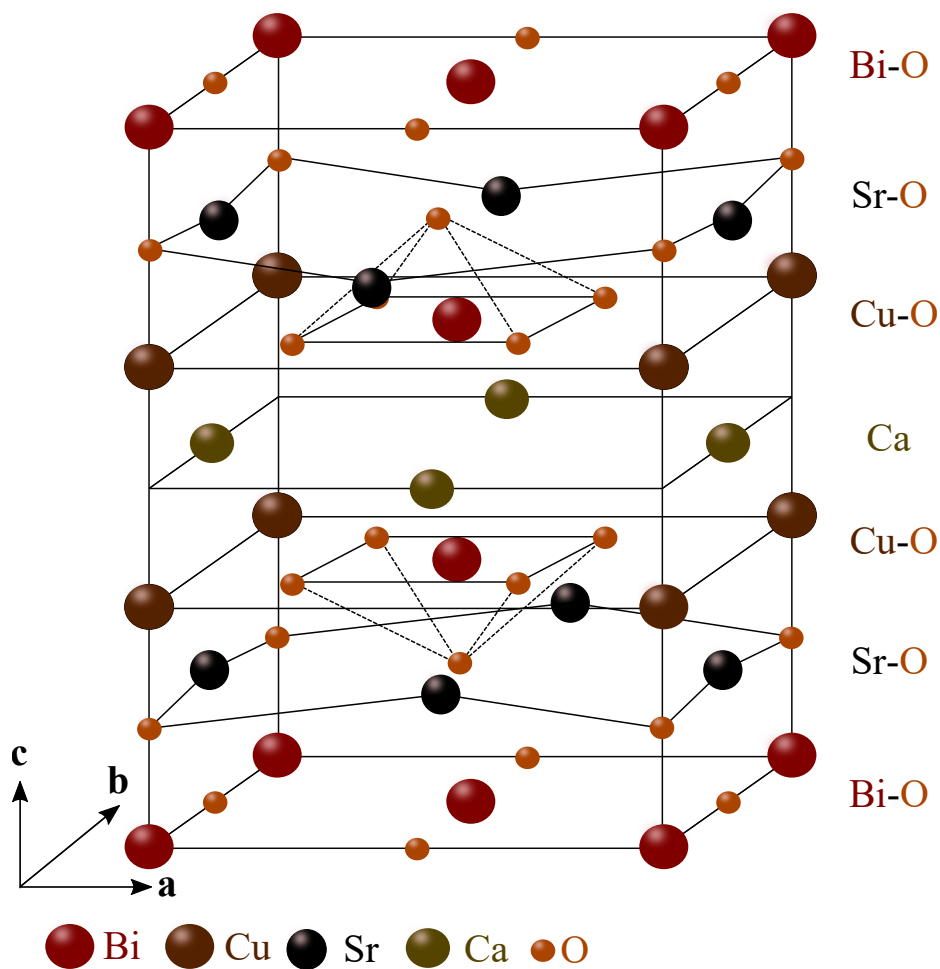
1.3.2 Bi-2212

Historically, Bi-2212 was the first synthesized high- T_c cuprate absent of rare earth elements [32]. Since its discovery, Bi-2212 has become one of the most popular cuprates to study experimentally due to its stability at atmospheric conditions and its layered nature [8]. These layers are perpendicular to the crystallographic c -axis and are held together by weak Van der Waals forces, making it a prime candidate for two-dimensional analysis via mechanical exfoliation of the crystals [31, 33].

As shown in Fig. 1.8, the unit cell of Bi-2212 is a multilayered perovskite-like structure with a plane of Calcium atoms separating the upper and lower pyramidal structure [34]. Moreover, the unit cell includes two semiconducting Bi-O planes, two insulating Sr-O planes, and two charge carrying Cu-O planes [8]. The introduction of oxygen dopants to cuprates results in a non-stoichiometric compound (see Table 1.1). The added oxygen ions reside in interstitial sites above and below the Cu-O layers, ultimately leaching electrons and producing hole-doped Cu-O planes.

While the overall crystallographic structure of Bi-2212 is presumed to be orthorhombic (or pseudo-tetragonal since $a \approx b = 0.542$ nm and $c = 3.09$ nm [18]), the sub-structure

Figure 1.8: Simplified schematic depicting the unit cell of Bi-2212.



is more complicated when compared to other cuprates. There is a well-documented incommensurate structure present along the crystallographic b -axis [35–38], however, the degree of incommensurability remains unclear. While this may seem insignificant at first glance, determining this is crucial as the incommensurate structure has a direct impact on the vibrational and electronic dynamics of Bi-2212, two key properties driving conventional superconductivity and thought to hold some degree of importance in high- T_c superconductivity [39]. This will be discussed further in Chapter 4.

1.4 Present work

In this work, we study cuprate systems through both experimental and numerical means. The experimental aspect of this work acts as an extension of Ref. [40], where we study the room temperature acoustic phonon dynamics in Bi-2212 by Brillouin light scattering spectroscopy. From our experiments, we identified eight individual acoustic phonon modes: the Rayleigh surface mode, two quasi-longitudinal bulk modes, four quasi-transverse bulk modes, and a longitudinal resonance mode. From the spectral line width and frequency shift of a bulk acoustic mode, we calculate important optical properties, including the optical extinction and absorption coefficients, optical penetration depth, and the complex dielectric constant at the commonly used wavelength of 532 nm. Moreover, with the observation of twice the number of acoustic phonon modes compared to what is typically expected in a crystalline solid, we take this as evidence that Bi-2212 is comprised of two weakly interacting sublattices, as described by the aperiodic model for incommensurate composite systems [41, 42]. From collected Brillouin spectra, the bulk sublattice acoustic phonon velocities were determined and subsequently used along with a previously derived expression relating sublattice and long-wavelength phonon velocities to obtain the bulk long-wavelength longitudinal velocity and allow for our sublattice assignment of $\text{Bi}_2\text{Sr}_2\text{O}_4$ and CaCu_2O_4 . Additionally, using this velocity relationship alongside a separate set of functions relating acoustic phonon modes along high symmetry directions [43] and our own derived result for elastic constants associated with sublattice longitudinal acoustic phonons, we calculated the room temperature elastic constants C_{11} , C_{22} , C_{33} , C_{44} , C_{55} , C_{12} , C_{13} , C_{23} , and the sublattice elastic constant counterparts associated with C_{22} , C_{44} , and C_{66} .

The numerical work presented in this thesis is the study of the single-band two-dimensional (2D) $t - t' - U$ Hubbard model in the weak coupling limit using a diagrammatic perturbation theory approach. We calculate the longitudinal density-density and spin-spin correlation functions in the $\chi_{\uparrow\uparrow}$ and $\chi_{\uparrow\downarrow}$ basis which in turn allow for the derivation of the static and dynamical spin and charge susceptibilities. We study these susceptibilities as functions of both doping and temperature. Most notably, our calculations show that for $t' \neq 0$, excitations at the wavevector $\mathbf{q} = (\pi, \pi)$ associated with the static (i.e., zero frequency) spin and charge susceptibilities have maxima at different densities, and show a dynamical change surrounding the van

Hove singularity of the non-interacting dispersion that our perturbative expansion is constructed from. Moreover, we observe the same behaviour in both the calculated compressibility and double occupancy. In the case of excitations resulting from the dynamical (i.e., non-zero frequency) spin and charge susceptibilities, we determined splitting in both cases surrounding the van Hove singularity of the non-interacting dispersion, which originates from a splitting of the bottom of the Hubbard band.

The work presented in this thesis is significant for several reasons. With respect to the experimental Brillouin data, the importance is multifold. Firstly, our acoustic phonon measurements support the idea that the Bi-2212 unit cell consists of two individual sublattices. This distinction will be of interest to those working on theoretical modelling of cuprates as this substructure may be a significant factor in discrepancies between experimental and theoretical work in these materials. Additional understanding of the substructure of Bi-2212 may also hold the key to the underlying driving mechanisms behind high- T_c superconductivity. Moreover, work on aperiodic systems is primarily theory-based and our newly published experimental data on the Bi-2212 substructure and newly derived relationship between sublattice and bulk elastic constants can help to refine the theories surrounding incommensurate crystallography. Lastly, in the case of our calculations on the 2D-Hubbard model, our results will also be helpful for those studying cuprate materials experimentally as they indicate that spin and charge excitations in overdoped samples require probing higher energies when compared to those which are underdoped.

This thesis is a sandwich-style document and its layout is as follows. Chapter 2 contains relevant information and theory surrounding the numerical investigation of the 2D Hubbard model, while Chapter 3 includes the manuscript titled “One- and two-particle properties of the weakly interacting two-dimensional Hubbard model in proximity to the van Hove singularity” published in Physical Review B. Chapter 4 outlines relevant theory and experimental details surrounding the investigation of Bi-2212 via Brillouin light scattering spectroscopy. Chapter 5 is comprised of the three resulting publications from the experimental component of this work; “*Optical constants of crystalline $Bi_2Sr_2CaCu_2O_{8+\delta}$ by Brillouin light scattering spectroscopy*” published in Superconductor Science and Technology, “*Long-wavelength phonon dynamics in incommensurate $Bi_2Sr_2CaCu_2O_{8+\delta}$ crystals by Brillouin light scattering spectroscopy*” published in Physical Review B, and “*Influence of incommensurate structure on the*

elastic constants of crystalline $\text{Bi}_2\text{Sr}_2\text{CaCu}_2\text{O}_{8+\delta}$ by Brillouin light scattering spectroscopy” published in Materials Research Express. Lastly, Chapter 6 provides some concluding remarks and directions for future work.

Bibliography

- [1] D. van Delft and P. Kes, Phys. Today **63**, 38 (2010).
- [2] D. van Delft, Phys. C: Supercond **479**, 30 (2012).
- [3] W. Meissner and R. Ochsenfeld, Sci. Nat. **21**, 787 (1933).
- [4] J. Bardeen, L. N. Cooper, and J. R. Schrieffer, Phys. Rev. **106**, 162 (1957).
- [5] J. Bardeen, L. N. Cooper, and J. R. Schrieffer, Phys. Rev. **108**, 1175 (1957).
- [6] T. Dubouchet, B. Sacépé, J. Seidemann, D. Shahar, M. Sanquer, and C. Chapelier, Nat. Phys. **15**, 233–236 (2018).
- [7] P. J. Ray, *Structural investigation of $\text{La}_{2-x}\text{Sr}_x\text{CuO}_{4+y}$* , Ph.D. thesis, Master’s thesis (University of Copenhagen, 2015) (2015).
- [8] A. Mourachkine, *High Temperature Superconductivity in Cuprates - the Nonlinear Mechanism and Tunneling Measurements*. (Kluwer Academic Publishers, 2002).
- [9] Y. Yin, M. Zech, T. L. Williams, X. F. Wang, G. Wu, X. H. Chen, and J. E. Hoffman, Phys. Rev. Lett. **102**, 097002 (2009).
- [10] M. Rotter, M. Tegel, and D. Johrendt, Phys. Rev. Lett. **101**, 107006 (2008).
- [11] Z.-A. Ren, G.-C. Che, X.-L. Dong, J. Yang, W. Lu, W. Yi, X.-L. Shen, Z.-C. Li, L.-L. Sun, F. Zhou, *et al.*, EPL **83**, 17002 (2008).
- [12] A. P. Drozdov, M. I. Eremets, I. A. Troyan, V. Ksenofontov, and S. I. Shylin, Nature **525**, 73–76 (2015).
- [13] A. P. Drozdov, P. P. Kong, V. S. Minkov, S. P. Besedin, M. A. Kuzovnikov, S. Mozaffari, L. Balicas, F. F. Balakirev, D. E. Graf, V. B. Prakapenka, E. Greenberg, D. A. Knyazev, M. Tkacz, and M. I. Eremets, Nature **569**, 528–531 (2019).

- [14] M. Somayazulu, M. Ahart, A. K. Mishra, Z. M. Geballe, M. Baldini, Y. Meng, V. V. Struzhkin, and R. J. Hemley, *Phys. Rev. Lett.* **122**, 027001 (2019).
- [15] V. L. Ginzburg, *Rev. Mod. Phys.* **76**, 981 (2004).
- [16] J. G. Bednorz and K. A. Müller, *Z. Phys. B Condens.* **64**, 189 (1986).
- [17] D. M. Ginsberg, *Physical properties of high temperature superconductors I* (World scientific, 1990).
- [18] J. Dominec, *Supercond. Sci. Technol.* **6**, 153 (1993).
- [19] N. N. Kovaleva, A. V. Boris, T. Holden, C. Ulrich, B. Liang, C. T. Lin, B. Keimer, C. Bernhard, J. L. Tallon, D. Munzar, and A. M. Stoneham, *Phys. Rev. B* **69**, 054511 (2004).
- [20] I. Robinson, T. A. Assefa, Y. Cao, G. Gu, R. Harder, E. Maxey, and M. P. Dean, *J. Supercond. Nov. Magn.* **33**, 99 (2020).
- [21] M. K. Wu, J. R. Ashburn, C. J. Torng, P. H. Hor, R. L. Meng, L. Gao, Z. J. Huang, Y. Q. Wang, and C. W. Chu, *Phys. Rev. Lett.* **58**, 908 (1987).
- [22] H. Ihara, R. Sugise, M. Hirabayashi, N. Terada, M. Jo, K. Hayashi, A. Negishi, M. Tokumoto, Y. Kimura, and T. Shimomura, *Nature* **334**, 510 (1988).
- [23] P. Dai, B. Chakoumakos, G. Sun, K. Wong, Y. Xin, and D. Lu, *Phys. C: Supercond.* **243**, 201 (1995).
- [24] G. Sun, K. Wong, B. Xu, Y. Xin, and D. Lu, *Phys. Lett. A* **192**, 122 (1994).
- [25] S. Raghu, R. Thomale, and T. H. Geballe, *Phys. Rev. B* **86**, 094506 (2012).
- [26] N. Hussey, R. Cooper, X. Xu, Y. Wang, I. Mouzopoulou, B. Vignolle, and C. Proust, *Proc. Math. Phys. Eng. Sci.* **369**, 1626 (2011).
- [27] T. M. Rice, N. J. Robinson, and A. M. Tselik, *Phys. Rev. B* **96**, 220502 (2017).
- [28] N. Barišić, M. K. Chan, Y. Li, G. Yu, X. Zhao, M. Dressel, A. Smontara, and M. Greven, *PNAS* **110**, 12235 (2013).
- [29] D. Neilson, *Aust. J. Phys.* **49**, 79 (1996).

- [30] M. Qin, T. Schäfer, S. Andergassen, P. Corboz, and E. Gull, *Annu. Rev. Condens. Matter Phys.* **13**, 275 (2022).
- [31] T. P. Sheahen, *Introduction to High Temperature Superconductivity*. (Kluwer Academic Publishers, 1994).
- [32] C. S. Lim, L. Wang, C. K. Chua, Z. Sofer, O. Jankovský, *J. Mater. Chem. A* **3**, 8346 (2015).
- [33] F. Liu, *Prog. Surf. Sci.* **96**, 100626 (2021).
- [34] P. Szuromi and B. Grocholski, *Science* **358**, 732 (2017).
- [35] X. B. Kan and S. C. Moss, *Acta Crystallogr. B.* **48**, 122 (1992).
- [36] J. Etrillard, Ph Bourges, H.F. He, B. Keimer, B. Liang and C.T. Lin, *EPL* **55**, 201 (2001).
- [37] P. Miles, S. Kennedy, G. McIntyre, G. Gu, G. Russell, and N. Koshizuka, *Phys. C: Supercond.* **294**, 275 (1998).
- [38] S. A. Sunshine, T. Siegrist, L. F. Schneemeyer, D. W. Murphy, R. J. Cava, B. Batlogg, R. B. van Dover, R. M. Fleming, S. H. Glarum, S. Nakahara, R. Farrow, J. J. Krajewski, S. M. Zahurak, J. V. Waszczak, J. H. Marshall, P. Marsh, L. W. Rupp, and W. F. Peck, *Phys. Rev. B* **38**, 893 (1988).
- [39] A. Lanzara, P. V. Bogdanov, X. J. Zhou, S. A. Kellar, D. L. Feng, E. D. Lu, T. Yoshida, H. Eisaki, A. Fujimori, K. Kishio, J.-I. Shimoyama, T. Noda, S. Uchida, Z. Hussain, and Z.-X. Shen, *Nature* **412**, 510–514 (2001).
- [40] B. D. E. McNiven, *Optical Properties and Acoustic Phonon Dynamics of $Bi_2Sr_2CaCu_2O_{8+\delta}$ Crystals*, Master's thesis, Memorial University of Newfoundland (2020).
- [41] S. Van Smaalen, *Incommensurate crystallography*, Vol. 21 (OUP Oxford, 2007).
- [42] J. D. Axe and P. Bak, *Phys. Rev. B* **26**, 4963 (1982).
- [43] R. Stoneley, *Geophys. J. Int.* **8**, 176 (1963).

Chapter 2

Numerical Studies

2.1 Hubbard model

First established in 1963 by Hubbard [1, 2], the so-called Hubbard model has in many ways become the foundation of the field of many-body physics. Originally proposed to theoretically describe narrow energy bands, it has since been used as a basis to describe electronic correlations in quantum materials (for a comprehensive review, see Refs. [3, 4]).

The Hubbard model is an effective model of coulombic interactions for a lattice system where the interactions are approximated as having only local components. The single-band Hamiltonian defined as

$$H = - \sum_{ij \in \xi} \sum_{\sigma} t_{ij} (c_{i\sigma}^{\dagger} c_{j\sigma} + c_{j\sigma}^{\dagger} c_{i\sigma}) + U \sum_{i \in \xi} c_{i\uparrow}^{\dagger} c_{i\uparrow} c_{i\downarrow}^{\dagger} c_{i\downarrow}, \quad (2.1)$$

where ξ is the set of spatially localized sites.

The first piece in Eqn. 2.1 is the kinetic term. Here, indices i and j refer to the encompassing set (ξ) of spatially localized lattice sites, while σ is the electron spin (equal to \uparrow or \downarrow). Further, t_{ij} is an energy prefactor defining the hopping amplitude between lattice site, and $c_{i\sigma}^{\dagger}$ ($c_{i\sigma}$) is the creation(annihilation) operator for a given electron of spin σ at lattice site i . The second term of Eqn. 2.1 is the local potential. Perhaps the most defining characteristic of the Hubbard model, this term includes an approximated Coulomb potential by replacing $k_e \sum_i \frac{q_i}{|\mathbf{r}-\mathbf{r}_i|}$ with a constant U to avoid

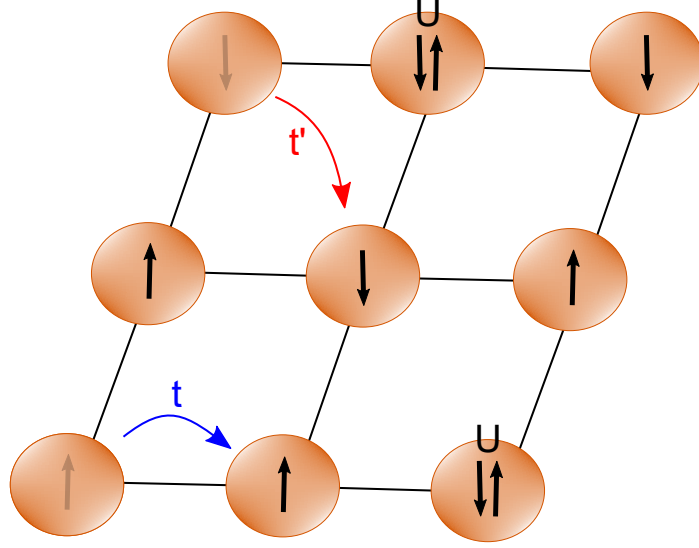


Figure 2.1: Schematic representation of a 2D square lattice. U - onsite Hubbard interaction for doubly occupied lattice site, t (t') nearest (next-nearest) neighbor hopping amplitude of a given electron moving lattice sites.

divergence issues as $|\mathbf{r} - \mathbf{r}_i| \rightarrow 0$.

Defining neighbor hopping is important and will dictate the form of the kinetic term in Eqn. 2.1. We restrict hopping to include nearest and next-nearest neighbor lattice sites, resulting in a kinetic energy of

$$\sum_{ij \in \xi} \sum_{\sigma} t_{ij} (c_{i\sigma}^{\dagger} c_{j\sigma} + c_{j\sigma}^{\dagger} c_{i\sigma}) = \sum_{\langle i,j \rangle} \sum_{\sigma} t_{\langle i,j \rangle} (c_{i\sigma}^{\dagger} c_{j\sigma} + c_{j\sigma}^{\dagger} c_{i\sigma}) + \sum_{\langle\langle i,j \rangle\rangle} \sum_{\sigma} t'_{\langle\langle i,j \rangle\rangle} (c_{i\sigma}^{\dagger} c_{j\sigma} + c_{j\sigma}^{\dagger} c_{i\sigma}), \quad (2.2)$$

where $t_{\langle i,j \rangle}$ and $t_{\langle\langle i,j \rangle\rangle}$ are the nearest and next-nearest neighbor hopping amplitudes, respectively.

In this thesis, we work on a two-dimensional (2D) square lattice (see Fig. 2.1). This means all spatial distances are all uniform and thus both hopping amplitudes are simply chosen constants. For this reason, they may be removed from the sum, and upon substituting 2.2 into Eqn. 2.1, yields

$$H = -t \sum_{\langle i,j \rangle} \sum_{\sigma} (c_{i\sigma}^{\dagger} c_{j\sigma} + c_{j\sigma}^{\dagger} c_{i\sigma}) - t' \sum_{\langle\langle i,j \rangle\rangle} \sum_{\sigma} (c_{i\sigma}^{\dagger} c_{j\sigma} + c_{j\sigma}^{\dagger} c_{i\sigma}) + U \sum_i c_{i\uparrow}^{\dagger} c_{i\uparrow} c_{i\downarrow}^{\dagger} c_{i\downarrow}. \quad (2.3)$$

2.2 Relevant observables

2.2.1 Green's function

Derivation

At zero-temperature, Green's function can be defined as [5]

$$G(\mathbf{k}, t_1 - t_2) = -i \langle | \mathcal{T} c_{\mathbf{k}}(t_1) c_{\mathbf{k}}^\dagger(t_2) | \rangle \quad (2.4)$$

where \mathcal{T} is the time ordering operator and t_i are time. From here, we insert the S-matrix $S(0, -\infty) |0\rangle$ into 2.4 to rewrite the Green's function in terms of a non interacting function:

$$G(\mathbf{k}, t_1 - t_2) = -i \langle 0 | S(-\infty, 0) \mathcal{T} c_{\mathbf{k}}(t_1) c_{\mathbf{k}}^\dagger(t_2) S(0, \infty) | 0 \rangle. \quad (2.5)$$

Rewriting 2.5 in terms of the interaction representation via the time development operator:

$$U(t_i) = e^{\frac{it_i}{\hbar}(H-H_0)},$$

Eqn. 2.5 can be simplified to

$$G(\mathbf{k}, t_1 - t_2) = -i \langle 0 | \mathcal{T} S(-\infty, 0) U(0) U^\dagger(t_1) \hat{c}_{\mathbf{k}}(t) S(t_1, t_2) \hat{c}_{\mathbf{k}}^\dagger(t_2) \times U(t_2) U^\dagger(0) S(0, \infty) | 0 \rangle, \quad (2.6)$$

where $c_{\mathbf{k}}(t_i) = U^\dagger(t_i) \hat{c}_{\mathbf{k}}(t_i) U(t_i)$, or equivalently in S-matrix representation:

$$G(\mathbf{k}, t_1 - t_2) = -i \theta(t_1 - t_2) \langle 0 | S(-\infty, 0) S(0, t_1) \hat{c}_{\mathbf{k}}(t_1) S(t_1, 0) S(0, t_2) \times \hat{c}_{\mathbf{k}}^\dagger(t_2) S(t_2, 0) S(0, -\infty) | 0 \rangle + i \theta(t_2 - t_1) \langle 0 | S(-\infty, 0) S(0, t_2) \times \hat{c}_{\mathbf{k}}^\dagger(t_2) S(t_2, 0) S(0, t_1) \hat{c}_{\mathbf{k}}(t_1) S(t_1, 0) S(0, -\infty) | 0 \rangle, \quad (2.7)$$

where $\theta(\pm(t_1 - t_2))$ is the step function. To encompass the function over all possible states, we define the S-matrix property

$$\langle 0 | = \frac{\langle 0 | S(\infty, -\infty)}{\langle 0 | S(\infty, -\infty) | 0 \rangle},$$

where its substitution into Eqn 2.7 yields

$$G(\mathbf{k}, t_1 - t_2) = \frac{1}{\langle 0 | S(\infty, -\infty) | 0 \rangle} \left(-i \theta(t_1 - t_2) \langle 0 | S(\infty, t_1) \hat{c}_{\mathbf{k}}(t_1) S(t_1, t_2) \times \right. \\ \left. \hat{c}_{\mathbf{k}}^\dagger(t_2) S(t_2, -\infty) | 0 \rangle + i \theta(t_2 - t_1) \times \right. \\ \left. \langle 0 | S(\infty, t_2) \hat{c}_{\mathbf{k}}^\dagger(t_2) S(t_2, t_1) \hat{c}_{\mathbf{k}}(t_1) S(t_1, -\infty) | 0 \rangle \right). \quad (2.8)$$

This reduces to the familiar form of the non-interacting Green's function:

$$G_0(\mathbf{k}, t_1 - t_2) = -i \langle 0 | \mathcal{T} \hat{c}_{\mathbf{k}}(t_1) \hat{c}_{\mathbf{k}}^\dagger(t_2) | 0 \rangle. \quad (2.9)$$

Performing a Fourier transform on 2.9:

$$G_0(\mathbf{k}, \omega) = \int_{-\infty}^{\infty} e^{i\omega\Delta t} G_0(\mathbf{k}, t) d\Delta t, \quad (2.10)$$

where $\Delta t = t - t'$, we obtain

$$G_0(\mathbf{k}, \omega) = \frac{1}{\omega - \epsilon(\mathbf{k}) + i\Gamma}, \quad (2.11)$$

where ω is the frequency and the $i\Gamma$ is introduced as an artificial broadening parameter to ensure convergence. $\epsilon(\mathbf{k})$ in Eqn. 2.11 (where the prefactor \hbar is set to 1 for convenience) is the free-particle energy dispersion. In this thesis, we work with the tight-binding free-particle energy containing up to next-nearest neighbor hopping,

$$\epsilon(\mathbf{k}) = -2t[\cos(k_x) + \cos(k_y)] - 4t'[\cos(k_x) \cos(k_y)] - \mu, \quad (2.12)$$

where μ is the chemical potential. The simplistic result of Eqn. 2.11 is quite handy as it can be used to obtain analytic functions for important one-particle properties such as the spectral function:

$$A(\mathbf{k}, \omega) = -Im G_0(\mathbf{k}, \omega) = \frac{1}{\pi} \frac{\Gamma}{(\omega - \epsilon(\mathbf{k}))^2 + \Gamma^2}, \quad (2.13)$$

density of states:

$$N(\omega) = \sum_{\mathbf{k}} A(\mathbf{k}, \omega) = \frac{\Gamma}{\pi} \sum_{\mathbf{k}} \frac{1}{(\omega - \epsilon(\mathbf{k}))^2 + \Gamma^2}, \quad (2.14)$$

and the density operator:

$$n = \sum_{\mathbf{k}, \omega} = G_0(\mathbf{k}, \omega). \quad (2.15)$$

For finite temperatures, analogous temperature dependent expressions can be derived for Eqns. 2.13-2.14 via the bare Matsubara Green's function:

$$\mathcal{G}_0(\mathbf{k}, i\nu_n) = \frac{1}{i\nu_n - \epsilon(\mathbf{k})}, \quad (2.16)$$

where ν_n is the Matsubara frequency. For fermions, $\nu_n = (2n + 1)\pi/\beta$ and similarly, $\nu_n = (2n)\pi/\beta$ for bosons, where $\beta = 1/k_B T$. By replacing $i\nu_n \rightarrow \nu + i0^+$ in Eqn. 2.16, one can obtain real frequency results (i.e., an analogous expression to Eqn. 2.11).

Diagrammatic expansion

In this thesis, we look to study the finite temperature Green's function. This can be expressed generally as a perturbative expansion built upon the non-interacting Green's function [6]:

$$\begin{aligned} G(\tau, \tau') &= -\frac{Z_0}{Z} \sum_{m=0}^{\infty} \frac{(-1)^m}{m!} \int_0^\beta d\tau_1 \int_0^\beta d\tau_2 \times \\ &\dots \int_0^\beta d\tau_m \langle \mathcal{T}_m \hat{c}_I(\tau) \hat{c}_I^\dagger(\tau') \hat{V}_I(\tau_1) \hat{V}_I(\tau_2) \dots \hat{V}_I(\tau_m) \rangle_0, \end{aligned} \quad (2.17)$$

where $Z = \text{Tr}[e^{-\beta \hat{H}}]$ ($Z_0 = \text{Tr}[e^{-\beta \hat{H}_0}]$) is the interacting (non-interacting) partition function in the interaction representation, with the generalized Hamiltonian defined as

$$\hat{H} = \hat{H}_0 + \hat{V}, \quad (2.18)$$

where

$$\begin{aligned}\hat{H}_0 &= \sum_{i,j,\sigma} t_{ij} \hat{c}_{i\sigma}^\dagger \hat{c}_{j\sigma}, \\ \hat{V} &= \frac{1}{2} \sum_{ijkl} \sum_{\sigma\sigma'} U_{ijkl} \hat{c}_{i\sigma}^\dagger \hat{c}_{k\sigma'}^\dagger \hat{c}_{l\sigma'} \hat{c}_{j\sigma}.\end{aligned}\tag{2.19}$$

Given its sheer complexity, our goal in this thesis is to look at Eqn. 2.17 on an order by order basis. For example, the first order ($m = 0$) term of the Green's function expansion is

$$G_1(\tau, \tau') = -\frac{Z_0}{Z} \int_0^\beta d\tau_0 \langle \mathcal{T}_0 \hat{c}_I(\tau) \hat{c}_I^\dagger(\tau') \hat{V}_I(\tau_0) \rangle_0,\tag{2.20}$$

and upon substitution of Eqn. 2.19 yields

$$\begin{aligned}G_1(\tau, \tau') &= -\frac{Z_0}{2Z} \int_0^\beta d\tau_0 \left\langle \mathcal{T}_1 \hat{c}_I(\tau) \hat{c}_I^\dagger(\tau') \sum_{ijkl} U_{ijkl} \right. \\ &\quad \left. \times \sum_{\sigma\sigma'} \hat{c}_{i\sigma}^\dagger(\tau_0) \hat{c}_{k\sigma'}^\dagger(\tau_0) \hat{c}_{l\sigma'}(\tau_0) \hat{c}_{j\sigma}(\tau_0) \right\rangle_0.\end{aligned}\tag{2.21}$$

By application of Wick's theorem [5], we obtain

$$\begin{aligned}G_1(\tau, \tau') &= -\frac{Z_0}{2Z} \sum_{ijkl} U_{ijkl} \int_0^\beta d\tau_0 \left[\left\langle \hat{c}_I(\tau) \hat{c}_I^\dagger(\tau') \right\rangle_0 \times \right. \\ &\quad \left. \sum_{\sigma\sigma'} \left\langle \hat{c}_{j\sigma}(\tau_0) \hat{c}_{i\sigma}^\dagger(\tau_0) \right\rangle_0 \left\langle \hat{c}_{l\sigma'}(\tau_0) \hat{c}_{k\sigma'}^\dagger(\tau_0) \right\rangle_0 - \right. \\ &\quad \left\langle \hat{c}_I(\tau) \hat{c}_I^\dagger(\tau') \right\rangle_0 \sum_{\sigma\sigma'} \left\langle \hat{c}_{l\sigma'}(\tau_0) \hat{c}_{i\sigma}^\dagger(\tau_0) \right\rangle_0 \left\langle \hat{c}_{j\sigma}(\tau_0) \hat{c}_{k\sigma'}^\dagger(\tau_0) \right\rangle_0 + \\ &\quad \sum_{\sigma\sigma'} \left\langle \hat{c}_I(\tau) \hat{c}_{k\sigma'}^\dagger(\tau_0) \right\rangle_0 \left\langle \hat{c}_{l\sigma'}(\tau_0) \hat{c}_{i\sigma}^\dagger(\tau_0) \right\rangle_0 \left\langle \hat{c}_{j\sigma}(\tau_0) \hat{c}_I^\dagger(\tau') \right\rangle_0 - \\ &\quad \sum_{\sigma\sigma'} \left\langle \hat{c}_I(\tau) \hat{c}_{k\sigma'}^\dagger(\tau_0) \right\rangle_0 \left\langle \hat{c}_{j\sigma}(\tau_0) \hat{c}_{i\sigma}^\dagger(\tau_0) \right\rangle_0 \left\langle \hat{c}_{l\sigma'}(\tau_0) \hat{c}_I^\dagger(\tau') \right\rangle_0 + \\ &\quad \sum_{\sigma\sigma'} \left\langle \hat{c}_{j\sigma}(\tau_0) \hat{c}_{k\sigma'}^\dagger(\tau_0) \right\rangle_0 \left\langle \hat{c}_I(\tau) \hat{c}_{i\sigma}^\dagger(\tau_0) \right\rangle_0 \left\langle \hat{c}_{l\sigma'}(\tau_0) \hat{c}_I^\dagger(\tau') \right\rangle_0 - \\ &\quad \left. \sum_{\sigma\sigma'} \left\langle \hat{c}_I(\tau) \hat{c}_{i\sigma}^\dagger(\tau_0) \right\rangle_0 \left\langle \hat{c}_{l\sigma'}(\tau_0) \hat{c}_{k\sigma'}^\dagger(\tau_0) \right\rangle_0 \left\langle \hat{c}_{j\sigma}(\tau_0) \hat{c}_I^\dagger(\tau') \right\rangle_0 \right],\end{aligned}\tag{2.22}$$

or more compactly,

$$\begin{aligned}
G_1(\tau, \tau') = -\frac{Z_0}{2Z} \sum_{ijkl} U_{ijkl} \int_0^\beta d\tau_0 \left[G_0(\tau, \tau') G_0(\tau_{0j}, \tau_{0i}) G_0(\tau_{0l}, \tau_{0k}) - \right. \\
G_0(\tau, \tau') G_0(\tau_{0l}, \tau_{0i}) G_0(\tau_{0j}, \tau_{0k}) + G_0(\tau, \tau_{0k}) G_0(\tau_{0l}, \tau_{0i}) \times \\
G_0(\tau_{0j}, \tau') - G_0(\tau, \tau_{0k}) G_0(\tau_{0j}, \tau_{0i}) G_0(\tau_{0l}, \tau') + \\
\left. G_0(\tau_{0j}, \tau_{0k}) G_0(\tau, \tau_{0i}) G_0(\tau_{0l}, \tau') - G_0(\tau, \tau_{0i}) G_0(\tau_{0l}, \tau_{0k}) G_0(\tau_{0j}, \tau') \right]. \tag{2.23}
\end{aligned}$$

The resulting six terms shown in Eqns. 2.22-2.23 correspond to the six first order diagrams of the Green's function expansion, as seen in Fig. 2.2. From the figure, there are both connected (1,2,4,5) and disconnected (3,6) diagrams, however, only connected diagrams contribute to the overall expansion as disconnected diagrams are "divided out" by the presence of the partition functions. Further, diagrams 1 – 2 and 4 – 5 are topologically identical and only need to be considered once. Thus, in the overall Green's function expansion, there are only two first order diagram contributions.

This procedure can be repeated to obtain the Green's function diagrammatic expansion, regardless of order. Fig. 2.3 shows the diagrammatic Green's function expansion including the non-interacting Green's function (first diagram), along with the topologically distinct first and second order diagrams contributing to the expansion. Many orders have both reducible and irreducible diagrams, with examples of each shown in the figure. Simply put, reducible diagrams can be cut into separate diagrams by bisecting a Green's function line (solid line). Each of the remaining diagrams after bisection correspond to diagrams of lower order, as seen by the reducible $m = 2$ diagrams in Fig. 2.3. Conversely, irreducible diagrams cannot be reduced by Green's function line bisection. These details will be important for the following section.

Dyson's equation and the self-energy

For a generalized Hamiltonian like that shown in Eqn. 2.18, the associated interacting Green's function composed of both irreducible and reducible diagrams can be rewritten as

$$G(\mathbf{k}, \omega) = \frac{1}{\omega - \hat{H}(\mathbf{k}, \omega)} = \frac{1}{\omega - \epsilon(\mathbf{k}) - \Sigma(\mathbf{k}, \omega)}, \tag{2.24}$$

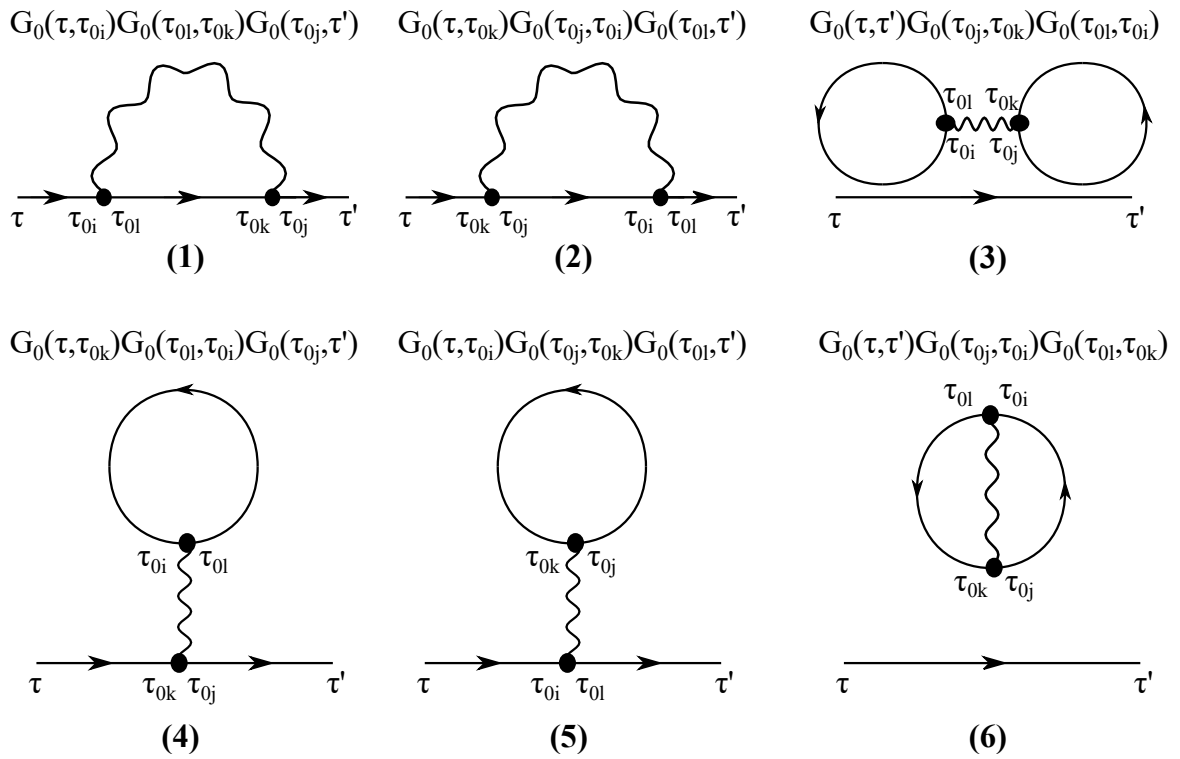


Figure 2.2: The six resulting first order Green's function diagrams from the perturbative expansion derived in Eqn. 2.23.

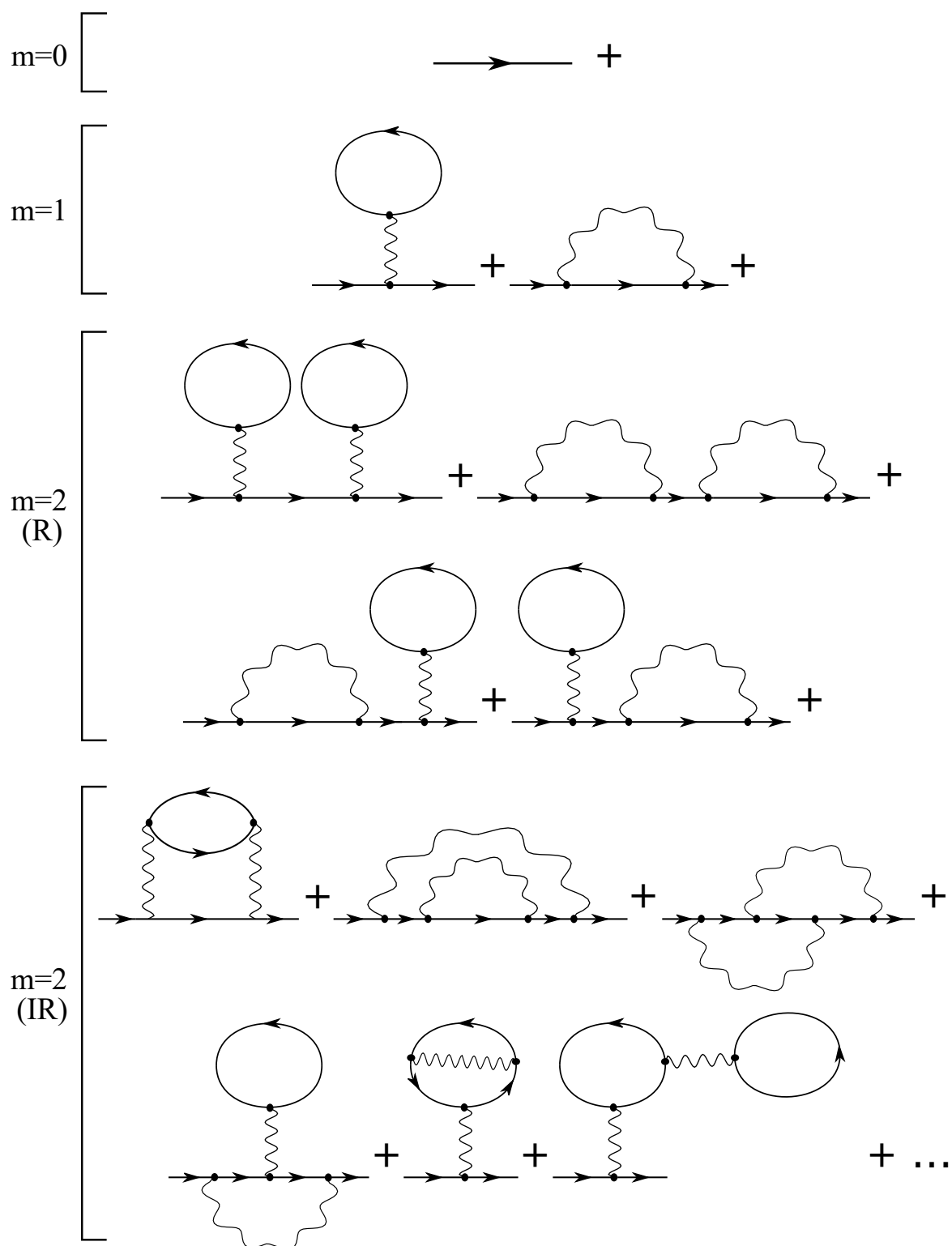


Figure 2.3: Contributing diagrams for $m = 0 - 2$ in the Green's function expansion derived in Eqn. 2.23. R - reducible, IR - irreducible.

where $\epsilon(\mathbf{k})$ is the diagonalizable free-particle energy and $\Sigma(\mathbf{k}, \omega)$ is the summation of all irreducible diagrams and is called the self-energy.

Eqn. 2.24 can be expanded as

$$G(\mathbf{k}, \omega) = G_0(\mathbf{k}, \omega) + G_0(\mathbf{k}, \omega)\Sigma(\mathbf{k}, \omega)G_0(\mathbf{k}, \omega) + G_0(\mathbf{k}, \omega)\Sigma(\mathbf{k}, \omega) \times G_0(\mathbf{k}, \omega)\Sigma(\mathbf{k}, \omega)G_0(\mathbf{k}, \omega) + \dots, \quad (2.25)$$

and by rearranging:

$$G(\mathbf{k}, \omega) = G_0(\mathbf{k}, \omega) \left(1 + \Sigma(\mathbf{k}, \omega)G_0(\mathbf{k}, \omega) + \Sigma(\mathbf{k}, \omega) \times G_0(\mathbf{k}, \omega)\Sigma(\mathbf{k}, \omega)G_0(\mathbf{k}, \omega) + \dots \right), \quad (2.26)$$

$G(\mathbf{k}, \omega)$ takes the form of a geometric series such that

$$G(\mathbf{k}, \omega) = \frac{G_0(\mathbf{k}, \omega)}{1 - G_0(\mathbf{k}, \omega)\Sigma(\mathbf{k}, \omega)}, \quad (2.27)$$

Eqn 2.27 is known as Dyson's equation and is commonly used as a way to estimate $G(\mathbf{k}, \omega)$ by approximating $\Sigma(\mathbf{k}, \omega)$ up to a truncated order. It is worth noting, however, that its reliability is controversial as it assumes the dominant diagrammatic contributions of the self-energy are contained within this truncated order. Moreover, Dyson's equation is only applicable in the weak coupling limit (i.e., small U in the confines of the Hubbard model) [5], further reducing its applicability.

Diagrammatics within the Hubbard model

In this thesis, we work within the confines of the two-dimensional Hubbard model in momentum-frequency space, and thus diagrams in the Green's function expansion which are non-zero are those which allow for spin conservation. Specific rules for generating m^{th} order diagrams in the momentum-frequency space can be found in Ref. [5].

2.2.2 Longitudinal susceptibility functions

The spin susceptibility is a spin-spin correlation function defined in terms of the spin operator $\hat{S}_z(\tau, x)$:

$$\chi_s = \langle \mathcal{T} \hat{S}_z(\tau, x) \hat{S}_z(\tau', x') \rangle, \quad (2.28)$$

where \mathcal{T} is the time ordering operator. Noting that $\hat{S}_z(\tau, x) = \frac{1}{2}(\hat{n}_\uparrow(\tau, x) - \hat{n}_\downarrow(\tau, x))$, where $\hat{n}_\sigma(\tau, x) = c_\sigma^\dagger(\tau, x)c_\sigma(\tau, x)$ is the number operator and $\sigma \in \{\uparrow, \downarrow\}$ is the spin, Eqn. 2.28 can be rewritten as

$$\chi_s = \frac{1}{4} \left(\langle \mathcal{T} \hat{n}_\uparrow(\tau, x) \hat{n}_\uparrow(\tau', x') \rangle + \langle \mathcal{T} \hat{n}_\downarrow(\tau, x) \hat{n}_\downarrow(\tau', x') \rangle - \langle \mathcal{T} \hat{n}_\uparrow(\tau, x) \hat{n}_\downarrow(\tau', x') \rangle - \langle \mathcal{T} \hat{n}_\downarrow(\tau, x) \hat{n}_\uparrow(\tau', x') \rangle \right). \quad (2.29)$$

Assuming spin symmetry, *i.e.*,

$$\begin{aligned} \hat{n}_\uparrow(\tau, x) \hat{n}_\uparrow(\tau', x') &= \hat{n}_\downarrow(\tau, x) \hat{n}_\downarrow(\tau', x'), \\ \hat{n}_\uparrow(\tau, x) \hat{n}_\downarrow(\tau', x') &= \hat{n}_\downarrow(\tau, x) \hat{n}_\uparrow(\tau', x'), \end{aligned}$$

Eqn. 2.29 can be simplified as

$$\chi_s = \frac{1}{2} \left(\langle \mathcal{T} \hat{n}_\uparrow(\tau, x) \hat{n}_\uparrow(\tau', x') \rangle - \langle \mathcal{T} \hat{n}_\uparrow(\tau, x) \hat{n}_\downarrow(\tau', x') \rangle \right). \quad (2.30)$$

Alternatively, the charge susceptibility is a density-density correlation function and can be defined in terms of the number density $\hat{n}(\tau, x)$ via:

$$\chi_d = \langle \mathcal{T} \hat{n}(\tau, x) \hat{n}(\tau, x) \rangle. \quad (2.31)$$

With $\hat{n}(\tau, x) = \hat{n}_\uparrow(\tau, x) + \hat{n}_\downarrow(\tau, x)$, χ_d can be determined by a similar approach to that used above for χ_s :

$$\chi_d = 2 \left(\langle \mathcal{T} \hat{n}_\uparrow(\tau, x) \hat{n}_\uparrow(\tau', x') \rangle + \langle \mathcal{T} \hat{n}_\uparrow(\tau, x) \hat{n}_\downarrow(\tau', x') \rangle \right). \quad (2.32)$$

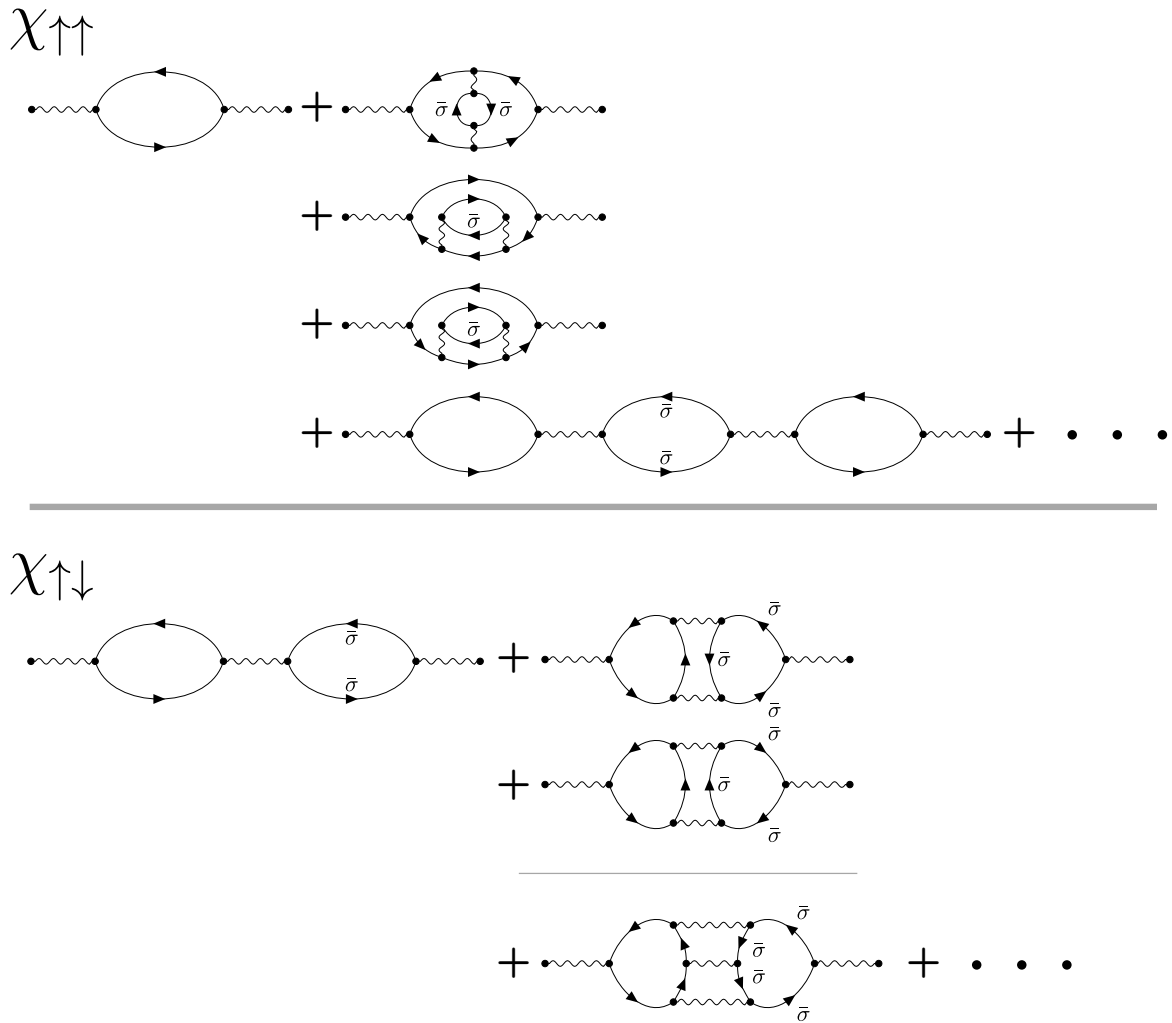


Figure 2.4: The first few diagrams in the perturbative expansions of $\chi_{\uparrow\uparrow}$ and $\chi_{\uparrow\downarrow}$, as seen in Ref. [7].

Given Eqns. 2.30 and 2.32 are of similar form, they can be rewritten in terms of two new susceptibility objects in the $\uparrow\uparrow / \uparrow\downarrow$ basis and are defined as [8]

$$\begin{aligned}\chi_{\uparrow\uparrow} &= 2\langle \mathcal{T} \hat{n}_{\uparrow}(\tau, x) \hat{n}_{\uparrow}(\tau', x') \rangle, \\ \chi_{\uparrow\downarrow} &= 2\langle \mathcal{T} \hat{n}_{\uparrow}(\tau, x) \hat{n}_{\downarrow}(\tau', x') \rangle.\end{aligned}\tag{2.33}$$

This allows for χ_s and χ_d to be rewritten in the simplistic form

$$\begin{aligned}\chi_s &= \chi_{\uparrow\uparrow} - \chi_{\uparrow\downarrow}, \\ \chi_d &= \chi_{\uparrow\uparrow} + \chi_{\uparrow\downarrow}.\end{aligned}\tag{2.34}$$

Fig 2.4 shows the first few diagrams of the $\chi_{\uparrow\uparrow}$ and $\chi_{\uparrow\downarrow}$ objects. It is noted that in the figure, $\bar{\sigma}$ associated with a given propagation line represents the opposite spin of the non-labelled propagation lines.

2.3 Algorithmic Matsubara Integration

In this thesis, we use the Algorithmic Matsubara Integration (AMI) algorithm to evaluate analytic representations of Feynman diagrams and obtain numerical results on both the Matsubara and real frequency axis. In the case of the former, the solution will be equivalent to commonly employed canonical Diagrammatic Monte Carlo (DiagMC) methods [9], however, DiagMC needs substantially more computational resources to probe the larger integration space required. Further, utilizing DiagMC methods to obtain numerical results on the real frequency axis for many problems is not feasible, making the AMI routine superior for problems in the weak coupling limit. Below we walk through the general workflow of the AMI routine, while specific particulars on the algorithm may be found in Refs. [10, 11].

Fig 2.5 shows the generalized workflow of the AMI routine. The routine is broken into three phases; initialization, construction, and evaluation. With no assumption of topology, the generalized n^{th} order Feynman diagram and its associated conservation labels (i.e., spin and momenta) are generated in the initialization stage. Once these are produced, we enter the construction phase where these diagrams are inputted into the AMI algorithm which in turn produces the analytic function expressed as sum over the internal variables (i.e., frequency, momenta).

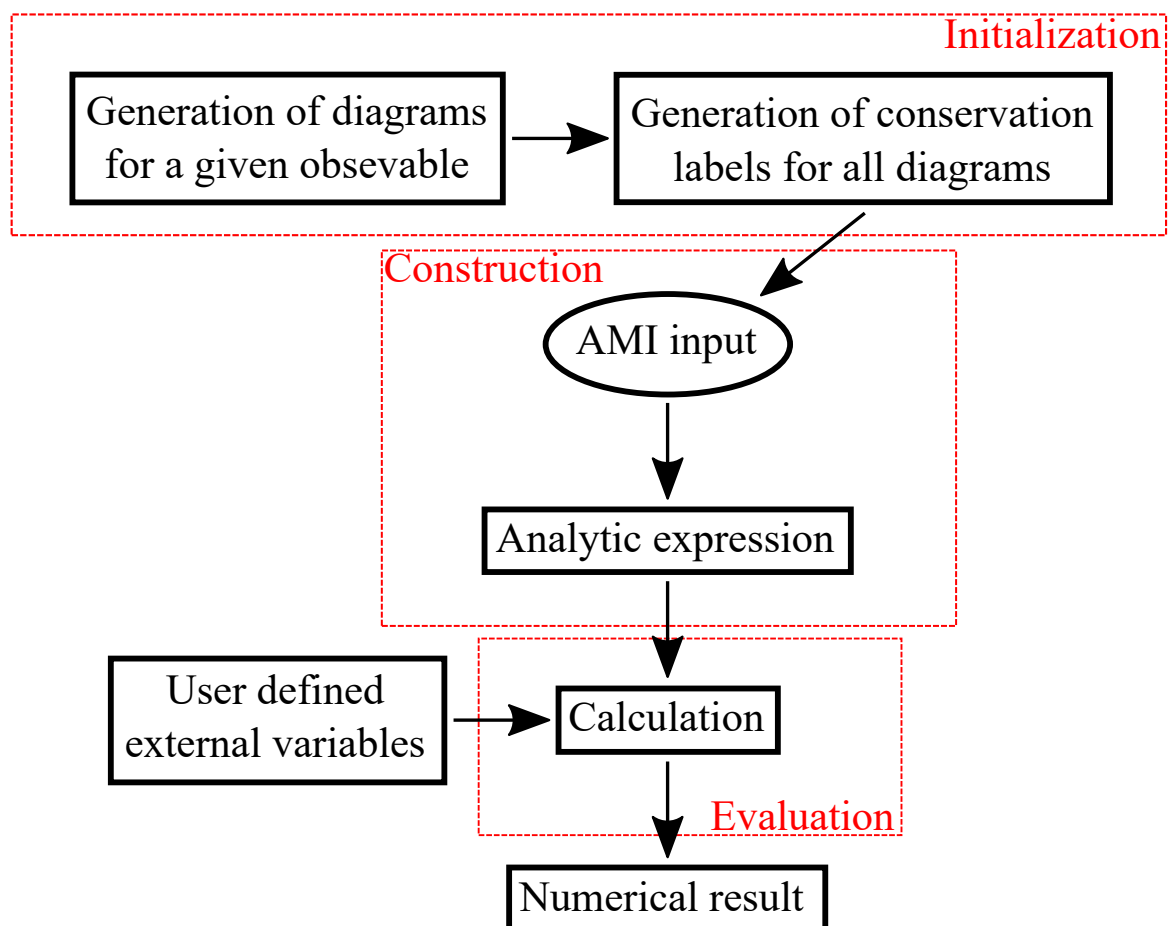


Figure 2.5: Workflow of the AMI routine used in the numerical portion of this work.

Once generated, the evaluation phase begins. Here, the algorithm takes the users external parameters as input (such as temperature, momenta, and complex frequency and chemical potential) and begins to evaluate the internal Matsubara summations up to the specified truncation order via the residue theorem, while the remaining external momenta sums are evaluated by standard Monte-Carlo sampling techniques. The resulting numerical answer for the diagrammatic expansion of the observable takes the form:

$$\mathcal{O} = \sum_{i=0}^n a_n U^n, \quad (2.35)$$

where n is the truncation order and a_n is the n^{th} order coefficient which is dependent upon the chosen external parameters.

Bibliography

- [1] J. Hubbard, Proc. Math. Phys. Eng. Sci. **276**, 238 (1963).
- [2] J. P. F. LeBlanc, A. E. Antipov, F. Becca, I. W. Bulik, G. K.-L. Chan, C.-M. Chung, Y. Deng, M. Ferrero, T. M. Henderson, C. A. Jiménez-Hoyos, E. Kozik, X.-W. Liu, A. J. Millis, N. V. Prokof'ev, M. Qin, G. E. Scuseria, H. Shi, B. V. Svistunov, L. F. Tocchio, I. S. Tupitsyn, S. R. White, S. Zhang, B.-X. Zheng, Z. Zhu, and E. Gull (Simons Collaboration on the Many-Electron Problem), Phys. Rev. X **5**, 041041 (2015).
- [3] D. P. Arovas, E. Berg, S. A. Kivelson, and S. Raghu, Annu. Rev. Condens. Matter Phys. **13**, 239 (2022).
- [4] M. Qin, T. Schäfer, S. Andergassen, P. Corboz, and E. Gull, Annu. Rev. Condens. Matter Phys. **13**, 275 (2022).
- [5] G. D. Mahan, *Many-particle physics* (Springer Science & Business Media, 2000).
- [6] J. Li, Y. Yu, E. Gull, and G. Cohen, Phys. Rev. B **105**, 165133 (2022).
- [7] B. D. E. McNiven, H. Terletska, G. T. Andrews, and J. P. F. LeBlanc, Phys. Rev. B **106**, 035145 (2022).
- [8] G. Rohringer, A. Valli, and A. Toschi, Phys. Rev. B **86**, 125114 (2012).

- [9] K. Van Houcke, E. Kozik, N. Prokof'ev, and B. Svistunov, *Phys. Procedia* **6**, 95 (2010).
- [10] H. Elazab, B. McNiven, and J. LeBlanc, *Computer Physics Communications* **280**, 108469 (2022).
- [11] A. Taheridehkordi, S. H. Curnoe, and J. P. F. LeBlanc, *Phys. Rev. B* **99**, 035120 (2019).

Chapter 3

Numerical publication

3.1 One- and two-particle properties of the weakly interacting two-dimensional Hubbard model in proximity to the van Hove singularity

In this section, we include the manuscript (and associated supplementary materials) titled “One- and two-particle properties of the weakly interacting two-dimensional Hubbard model in proximity to the van Hove singularity” presented in the journal Physical Review B (reference: PRB 106, 035145 (2022)). Reprinted with permission from authors B. D. E. McNiven, G. T. Andrews, Hanna Terletska, and J. P. F. LeBlanc, and Physical Review B. Copyright (2022) by the American Physical Society.

One- and two-particle properties of the weakly interacting two-dimensional Hubbard model in proximity to the van Hove singularity

B. D. E. McNiven¹, Hanna Terletska,² G. T. Andrews¹ and J. P. F. LeBlanc^{1,*}

¹*Department of Physics and Physical Oceanography, Memorial University of Newfoundland, St. John's, Newfoundland & Labrador, Canada A1B 3X7*

²*Department of Physics and Astronomy, Computational Sciences Program, Middle Tennessee State University, Murfreesboro, Tennessee 37132, USA*

 (Received 25 March 2022; revised 31 May 2022; accepted 6 July 2022; published 25 July 2022)

We study the weak-coupling limit of the $t - t' - U$ Hubbard model on a two-dimensional square lattice using a direct perturbative approach. Aided by symbolic computational tools, we compute the longitudinal density-density correlation functions in the $\chi_{\uparrow\uparrow}$ and $\chi_{\uparrow\downarrow}$ basis from which we can obtain the dynamical spin and charge susceptibilities at arbitrary doping and temperature. We find that for nonzero t' , the zero-frequency commensurate $\mathbf{q} = (\pi, \pi)$ spin and charge excitations are each strongest at different densities and we observe a clear behavioral change that appears tied to the van Hove singularity of the noninteracting dispersion upon which the perturbative expansion is built. We find a strongly reduced compressibility in the vicinity of the van Hove singularity as well as a behavioral change in the double occupancy. For finite t' , the observed van Hove singularity occurs away from half filling, leading us to conclude that this reduction in compressibility is distinct from the Mott insulating physics that one expects in the strong-coupling regime. We compute the full dynamical spin and charge excitations and observe distinct structure for electron- and hole-doped scenarios, in agreement with experiments on cuprate materials. Finally, we observe a peculiar splitting in spin and charge excitations in the vicinity of the van Hove singularity, the origin of which is traced to a splitting near the bottom of the band.

DOI: [10.1103/PhysRevB.106.035145](https://doi.org/10.1103/PhysRevB.106.035145)

I. INTRODUCTION

It is generally assumed that the dominant physics of the cuprate phase diagram emerges from strong electronic correlations, and, for this reason, the square lattice Hubbard model in the strong-coupling regime has been the focus of theoretical and computational studies [1–3] as well as experimental work on ultracold atom systems [4,5]. Such work on the Hubbard model has found a plethora of phases with striking similarity to the doping-dependent phase diagram of the high-temperature cuprate class of materials [6–8]. In contrast, much of the experimental work on cuprates connects single- and two-particle properties based on the arguments of nesting of scattering vectors for various Fermi-surface topologies [9]. If such nested momentum- or energy-transfer processes can be identified then the idea of vector nesting provides an incredibly powerful lens through which one can understand the effects of weak renormalization due to interactions [10] and has often been a central consideration for the development of phenomenological theories of pseudogap physics [11–15].

Dynamical mean-field theory (DMFT) [16] is perhaps the most well-known method for studying correlated electron systems which, when applied to the two-dimensional (2D) Hubbard model at strong-coupling strengths, finds a gapped system known as a Mott insulator that originates from both strong local electron-electron interactions *and*, in the case of

the Hubbard model, proximity to the half-filling point of the band (see Supplemental Materials [17]). Although alternate explanations remain possible [18], a number of numerical studies have suggested that strong commensurate spin excitations lead to pseudogapped and insulating states in the symmetric ($t' = 0$) half-filled two-dimensional (2D) Hubbard model in the weak-coupling limit, where direct perturbative schemes are convergent [19–22]. As temperature is decreased, the onset of insulating behavior occurs at smaller values of the Hubbard interaction strength U/t and also coincides with long-range antiferromagnetic spin-correlation lengths, and this behavior is observed from a variety of numerical methods [19,23–25]. This begs the question as to how one should interpret a wealth of literature that clearly demonstrates the formation of a Mott gap beyond the range of perturbative methods and above a finite critical interaction value U_c in the $T = 0$ limit [26–28].

For the single-band Hubbard model with only nearest-neighbor hopping, the strongest vector nesting is expected to occur at half filling. There is then the potential for a mixture of two physical phenomena occurring at the same point: insulating behavior due to vector nesting that is rooted in weak-coupling ideas, and Mott-insulating physics rooted in the strong-coupling limit. Separating these two effects is essential to developing a true understanding of the single-band model on the square lattice.

To delineate these two effects, we study the single-band model with finite next-neighbor hopping t' , which plays a key role since it moves the van Hove point for the noninteracting

*jleblanc@mun.ca

problem away from the half filled point and breaks the perfect $\mathbf{q} = (\pi, \pi)$ nesting. We then study the charge and spin excitation spectra in the weak-coupling limit. Our methodology is based on the direct perturbative expansion of density-density correlation functions in the form of Feynman diagrammatics in conjunction with a scheme to automate the analytic evaluation of Matsubara sums [29,30]. This scheme, known as algorithmic Matsubara integration (AMI), provides analytic expressions in which Matsubara frequencies can be analytically continued by replacing $i\omega \rightarrow \omega + i\Gamma$ which is exact in the $\Gamma \rightarrow 0^+$ limit. Furthermore, the calculations do not suffer from finite-size effects, and the generated expressions have explicit dependence on temperature and chemical potential, ultimately giving access to arbitrary temperatures and doping, which, when combined, allow us to develop a full picture of the weak-coupling physics within the model.

II. METHODS

A. Hubbard Hamiltonian

We study the single-band Hubbard Hamiltonian on a 2D square lattice [1],

$$H = \sum_{ij\sigma} t_{ij} c_{i\sigma}^\dagger c_{j\sigma} + U \sum_i n_{i\uparrow} n_{i\downarrow}, \quad (1)$$

where t_{ij} is the hopping amplitude, $c_{i\sigma}^\dagger$ ($c_{i\sigma}$) is the creation (annihilation) operator at site i , $\sigma \in \{\uparrow, \downarrow\}$ is the spin, U is the onsite Hubbard interaction, and $n_{i\sigma} = c_{i\sigma}^\dagger c_{i\sigma}$ is the number operator. We restrict the sum over sites to nearest and next-nearest neighbors for a 2D square lattice, resulting in the free-particle energy

$$\epsilon(\mathbf{k}) = -2t[\cos(k_x) + \cos(k_y)] - 4t'[\cos(k_x)\cos(k_y)] - \mu,$$

where μ is the chemical potential, and t (t') is the nearest (next-nearest) neighbor hopping amplitude. Throughout, we work with energies in units of the hopping, $t = 1$.

1. van Hove singularity

The primary effect of a nonzero t' is that the van Hove singularity will occur at a density away from half filling. For the noninteracting case this can be found analytically from $\epsilon(\mathbf{k})$. For values of $|t'| < 0.5$, the van Hove singularity occurs at a chemical potential of $\mu = 4t'$. For larger amplitudes of t' , the topology of the Fermi surface is changed substantially from the $t' = 0$ case, because the next-nearest-neighbor hopping becomes dominant [31]. We therefore restrict our study to nominal values of $|t'| < 0.5$.

In the case of noninteracting problems there is a one-to-one correspondence between the van Hove singularity and the location of a topological change in the Fermi surface known as a Lifshitz transition. Past studies of the Lifshitz transition in the 2D Hubbard model have focused on the large U/t insulating regime, where even for $t' = 0$, the Lifshitz transition occurs for densities $\langle n \rangle \equiv n < 0.5$ [32,33]. Our calculations represent a perturbative expansion built upon the Hartree-shifted but otherwise noninteracting problem. The inclusion of a Hartree-shift creates a U/t dependence in the relationship between chemical potential μ and density n . Since we are at the weakly interacting limit of the model, the system has

a metallic Fermi surface, and therefore the location of the van Hove point is not changed substantially from the non-interacting case and should always occur in the vicinity of $\mu = 4t'$. We therefore use this information to guide our choice of parameters throughout.

B. Perturbation expansion

We obtain the diagrams for the spin susceptibility $\chi_s = \langle \mathcal{T} \hat{S}_z(\tau, x) \hat{S}_z(\tau', x') \rangle$ and for the charge susceptibility $\chi_d = \langle \mathcal{T} \hat{n}(\tau, x) \hat{n}(\tau', x') \rangle$ via perturbative expansions of each set of operators. The two expansions are related due to the definitions of $\hat{S}_z = \hat{n}_\uparrow - \hat{n}_\downarrow$ and $\hat{n} = n_\uparrow + n_\downarrow$. We can therefore define the susceptibility in a basis of correlations between \hat{n}_\uparrow and \hat{n}_\downarrow operators. Assuming spin symmetry, we denote relevant correlation functions as $\chi_{\uparrow\uparrow} = 2\langle \mathcal{T} \hat{n}_\uparrow(\tau, x) \hat{n}_\uparrow(\tau', x') \rangle$ and $\chi_{\uparrow\downarrow} = 2\langle \mathcal{T} \hat{n}_\uparrow(\tau, x) \hat{n}_\downarrow(\tau', x') \rangle$ [34]. This leads to the simple relations $\chi_s = \chi_{\uparrow\uparrow} - \chi_{\uparrow\downarrow}$ and $\chi_d = \chi_{\uparrow\uparrow} + \chi_{\uparrow\downarrow}$.

We present as well the double occupancy $D = \langle n \rangle^2 + 2\langle \hat{n}_\uparrow(\tau, x) \hat{n}_\downarrow(\tau, x) \rangle$ [35]. The first term represents the uncorrelated disconnected diagrams while the second term is the local, same-time contribution from interactions. The second term can be obtained from the Fourier transform of the local, same-time expectation value above and is given by $\sum_{\mathbf{q}} \sum_n \chi_{\uparrow\downarrow}(\mathbf{q}, i\Omega_n)$. We provide a summary of each diagrammatic expansion in the Supplemental Materials [17]. The convergence rate for each observable can differ drastically. For example, results for double occupancy and density as well as quantities on the Matsubara axis are much easier to compute while results on the real frequency axis take substantially more computational effort. Results are obtained to fourth order in the interaction for static and Matsubara axis properties and for self-energies on the real-frequency axis, and to third order for real-frequency evaluation of susceptibilities. With these truncations in mind, we expect our results to be robust for values of $U/t < 4$ and $\beta t < 5$ at the half-filled point and for larger U/t and βt values away from half filling and for finite t' . We note that there is no conceptual barrier associated with extending to higher orders, but there is a computational hurdle that is beyond exponential in the expansion order. Further advancements will be required to overcome those hurdles, such as those suggested in Refs. [36,37].

C. Algorithmic Matsubara integration

First presented in Ref. [29], AMI automates the evaluation of internal Matsubara sums for arbitrary Feynman diagrams via a repeated application of the well-understood residue theorem. This works so long as the perturbative expansion can be built within a diagonal basis of known eigenvalues that are frequency independent. The interaction must also be frequency independent, or its frequency dependence must be explicitly known. In the case of the Hubbard interaction, the result of AMI applied to an n th-order diagram is an analytic expression comprised of a prefactor times U^n , a product of Fermi or Bose distribution functions and derivatives of such, and a product of noninteracting Green's functions. Each diagram typically results in many such terms, the number of which grow exponentially with expansion order (see Supplemental Materials [17]). We use AMI to analytically

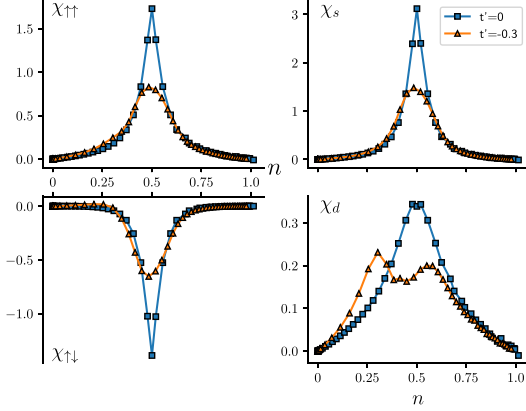


FIG. 1. The static two-particle susceptibility at scattering vector $\mathbf{q} = (\pi, \pi)$ in the $\chi_{\uparrow\uparrow}$, and $\chi_{\downarrow\downarrow}$ basis (left) and in the spin-charge basis (right) for $t' = 0.0, -0.3t$, $U/t = 3$, $\beta t = 5$ as a function of particle density n .

perform the Matsubara sums over the internal Matsubara frequencies for $\chi_{\uparrow\uparrow}$ and $\chi_{\downarrow\downarrow}$, and also the external frequency $i\Omega_n$ for the double occupancy. The resulting analytic expressions must then be integrated numerically over the remaining internal spatial degrees of freedom, which we resolve using standard Monte Carlo techniques for which we make use of the open source ALPSCORE framework [38,39] combined with the open source AMI library LIBAMI [40].

1. Analytic Wick rotation to the real frequency axis

The results of AMI are analytic expressions containing the external frequency that can be analytically continued to the real frequency axis without numerical methods such as maximum entropy inversion [41,42]. In the case of frequency-dependent observables, we perform analytic continuation by replacing the external frequency $i\Omega_n \rightarrow \omega + i\Gamma$, which is exact in the $\Gamma \rightarrow 0^+$ limit. Throughout, we employ a finite value of $\Gamma = 0.125$ which serves as a numerical regulator. The impact of the regulator can be controlled, with larger values of Γ acting to soften sharp features. The regulator should typically appear as the smallest energy scale to ensure it does not impact results.

2. Numerical analytic continuation to the real frequency axis

While numerical analytic continuation is not required in our approach, we can equally well produce results on the Matsubara axis and perform numerical analytic continuation. For this we employ the method of maximum entropy inversion using a flat default model [42] utilizing the code presented in Ref. [41] and its dependencies [38,39].

III. RESULTS

A. Doping and temperature dependence of static $\mathbf{q} = (\pi, \pi)$ susceptibilities

We present in Fig. 1 the density dependence of the static $\mathbf{q} = (\pi, \pi)$ susceptibility in the $\uparrow\uparrow / \uparrow\downarrow$, as well as the spin-

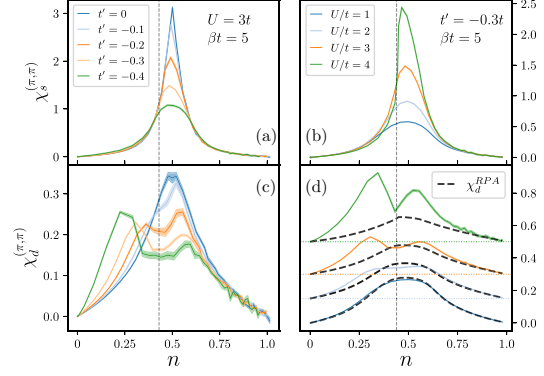


FIG. 2. The static spin (top row) and charge (bottom row) susceptibilities at $\mathbf{q} = (\pi, \pi)$, $t' = -0.3t$ as functions of doping for: (a), (c) fixed $U/t = 3$ for variation in t' , and (b), (d) for fixed t' for variation in U/t . Vertical lines represent the location of the van Hove singularity for $t' = -0.3t$ at $U/t = 3$ in the case of frames (a), (c) and for $U/t = 4$ in the case of frame (d). Black dashed curves in (d) are RPA results for the corresponding interaction strengths. χ_d and χ_d^{RPA} curves in frame (d) are offset for clarity.

charge bases (annotated by s and d following Ref. [34]) for the particle-hole symmetric case of $t' = 0$, and for a particle-hole asymmetric case of $t' = -0.3t$, both at $\beta t = 5$ for a nominal interaction strength of $U/t = 3$. Considering first $\chi_{\uparrow\uparrow}$ and $\chi_{\downarrow\downarrow}$, we see that the former is positive for all densities and peaked at the half filling point $n = 0.5$ while the latter is negative for all densities. The simple subtraction or addition of these two curves leads directly to the spin and charge susceptibilities [34], respectively, shown in the right-hand frame of Fig. 1. For $t' = 0$, the perfect particle-hole symmetry results in both the spin and charge susceptibility being strongest at half filling. This is not the case for finite t' where we see that moderate asymmetry leads to a mismatch between $\chi_{\uparrow\uparrow}$ and $\chi_{\downarrow\downarrow}$ peaks. When obtaining χ_s this slight asymmetry is washed out, and while it does decrease with t' , the spin susceptibility remains peaked near the half filled point. This is not the case for the charge susceptibility χ_d , where we see that the simple addition of $\chi_{\uparrow\uparrow}$ and $\chi_{\downarrow\downarrow}$ leads to a dip in susceptibility near half filling and creates a structure with one peak on the electron-doped side and a second peak on the hole-doped side. We have performed additional calculations from nonperturbative methods to verify the existence of the two-peak structure of χ_d (see Supplemental Materials [17]).

Precisely how the two-peak structure in χ_d is shaped is dependent upon the degree of asymmetry (value of t') but also on the temperature and interaction strength. We present results for $\chi_s^{(\pi, \pi)}$ and $\chi_d^{(\pi, \pi)}$ in Fig. 2 for variation in t' at fixed interaction strength of $U = 3t$ (left) and at fixed temperature ($\beta t = 5$) for variation in interaction strength (right). Beginning with commensurate spin excitations in Fig. 2(a), we see the dominant spin peak at $n = 0.5$ for the most widely studied case of $t' = 0$. Increasing the magnitude value of t' incrementally causes a reduction in $\chi_s^{(\pi, \pi)}$ in the vicinity of $n = 0.5$ and has virtually no effect below $n = 0.4$ or above $n = 0.6$.

In contrast, we see an entirely different behavior from $\chi_d^{(\pi,\pi)}$ shown in Fig. 2(c). While the peak in commensurate charge excitations for the $t' = 0$ case occurs at $n = 0.5$, even a modest change in t' causes a depletion of charge excitations which results in a two-peak structure as a function of doping [43]. Interestingly, the depletion is not centered at the half filled point, but instead in the vicinity of the van Hove singularity marked with a vertical dashed line. Shown in Fig. 2(d), this splitting appears to be a robust feature that exists above $U = 2t$ for increasing interaction strengths. Similarly, there is no structure in the spin susceptibility. For reference, we also include results for the charge susceptibility from the simplistic random-phase approximation, χ_d^{RPA} , marked as black dashed curves in Fig. 2(d). At weak $U/t = 1$ the AMI and RPA results are nearly identical, but for larger U/t the RPA result does not demonstrate a two-peak structure. While the RPA expansion does include some diagrams from $\chi_{\uparrow\downarrow}$ it does so only through even powers of the bare bubble diagram. This results in no mismatch in peaks of $\chi_{\uparrow\uparrow}$ and $\chi_{\uparrow\downarrow}$ as described in Fig. 1 and this results in only a single peak in the density dependence.

It is perhaps not surprising that we observe the maximal $\mathbf{q} = (\pi, \pi)$ charge excitations, at low temperatures, near the van Hove singularity since there the Fermi surface will most closely resemble that of the antiferromagnetic Brillouin zone and allow for vector nesting in the susceptibility. There is evidence to suggest that insulating behavior in the 2D Hubbard model at weak coupling is caused by strong $\mathbf{q} = (\pi, \pi)$ antiferromagnetic fluctuations [19,21,22,44], which in Fig. 2 remain centered at half filling. If pseudogap and insulating behavior are indeed due to antiferromagnetic fluctuations then we expect to find insulating behavior near half filling. We will see in the next section that this assertion appears to be false, and that the suppression of the charge susceptibility, which is an indicator of insulating character, is centered at the van Hove point and coincides with a reduced compressibility of the electron density.

B. Double occupancy and compressibility

Representing susceptibilities in the $\uparrow\uparrow / \uparrow\downarrow$ basis is particularly useful since it separates out the key element that distinguishes the charge and spin susceptibilities, namely, contributions from the correlated $2\chi_{\uparrow\downarrow}$. One can get an imprint of the impact of $\chi_{\uparrow\downarrow}(\mathbf{q}, \Omega)$ by examining also its same-time, local counterpart the double occupancy D . For a noninteracting system, one would find $\chi_{\uparrow\downarrow} = 0$ and the double occupancy is given by $D = \langle n \rangle^2$. For the interacting system, it is convenient to consider the deviation from the noninteracting case $\langle n \rangle^2 - D$ [35]. We present this deviation in Fig. 3 (top) for the particle-hole asymmetric case for $t' = -0.3t$ at nominal temperature of $\beta t = 5$ for increasing interaction strength. Here, a positive value of the deviation corresponds to a reduced value of the double occupancy which we see occurs for all densities, similar to the observed negative value of $\chi_{\uparrow\downarrow}$ in Fig. 1. One expects to find a maximal reduction in double occupancy occurring when interaction effects are maximal. Above $U = 2t$, the data exhibits a peak near $n = 0.3$ and demonstrates a kink feature at slightly higher density. This kink feature coincides with the van Hove singularity which for

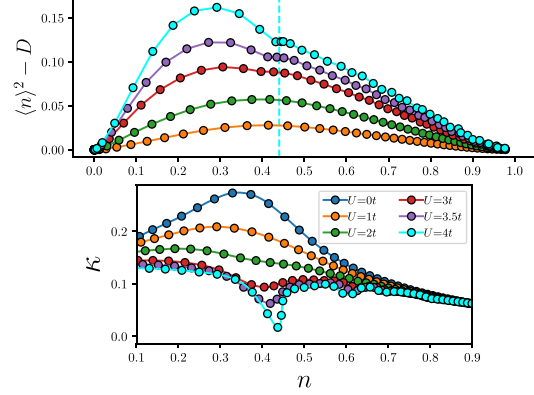


FIG. 3. Deviation of double occupancy from the uncorrelated case (top) and compressibility (bottom) as a function of density for fixed $t' = -0.3t$, $\beta t = 5$. Vertical dashed line marks location of van Hove singularity at $U/t = 4$.

$U = 4t$ occurs at a density of $n \approx 0.44$ (marked with vertical dashed line in Fig. 3).

We present also the compressibility, $\kappa = \frac{\partial n}{\partial \mu}$, as a function of density in the lower frame of Fig. 3. Upon increasing the interaction strength, we observe a reduction in compressibility that produces a minimum near the van Hove point. This reduction in compressibility grows stronger for increasing U/t and leads ultimately to an incompressible phase centered precisely at the van Hove point. We mark the van Hove point for $U/t = 4$ in the top frame of Fig. 3 and see that it coincides with a minima in the charge excitations displayed in the right-hand frames of Fig. 2 and not with the maxima of spin excitations. In the limit of strong coupling we expect that the role of spin excitations will dominate and this feature would migrate to the half filled point as seen from nonperturbative methods (see Supplemental Materials [17]), and similarly as one removes the particle-hole asymmetry due to t' .

Reiterating our earlier remark, the observation of incompressibility at the van Hove point and not at half filling, where spin excitations are strongest, conflicts with the assertion that it is $\mathbf{q} = (\pi, \pi)$ spin fluctuations that are responsible for pseudogap and insulating behavior seen in Refs. [19,20]. Past works studied primarily the $t' = 0$ case where the van Hove and half-filled points coincide. Here with finite t' we see that there are two distinct mechanisms causing insulating behavior: that of strong spin excitations and the role they are expected to play in pseudogap physics, and that of a peaked density of states that occurs near the van Hove singularity of the noninteracting system.

C. Momentum dependence of static spin and charge excitations

We present in Fig. 4 results of the static spin (top row) and charge (bottom row) susceptibility for the $U/t = 2.5$ case, plotted as a function of the scattering vector \mathbf{q} . This choice of interaction strength is large enough to show distinct spin and charge behavior while keeping numerical uncertainty under control. For densities above half filling the spin and charge

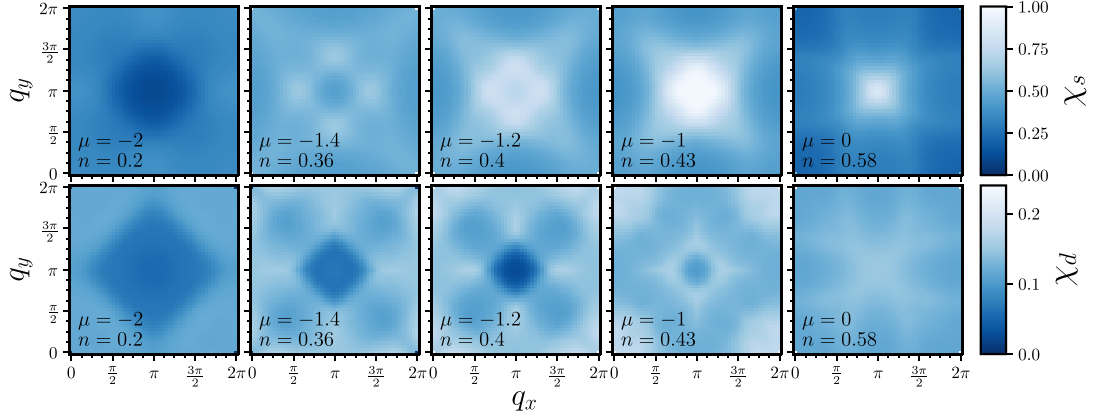


FIG. 4. $\chi_s(\Omega = 0, \mathbf{q})$ (top) and $\chi_d(\Omega = 0, \mathbf{q})$ (bottom) as a function of q_x and q_y for $U/t = 2.5$, $t' = -0.3t$, and $\beta t = 5$ for a range of densities $n = 0.2 \rightarrow 0.58$.

susceptibilities appear similar, with both having maximal values at $\mathbf{q} = (\pi, \pi)$. The spin susceptibility at (π, π) , however, is substantially larger than at other q vectors while the charge susceptibility is much more diffuse. As one reduces chemical potential towards the van Hove point at $\mu = -1.2$, we primarily note the separation of the single $\mathbf{q} = (\pi, \pi)$ spin excitation into two distinct peaks at $\mathbf{q} = (\pi \pm \delta, \pi)$ and $\mathbf{q} = (\pi, \pi \pm \delta)$, as noted in previous works [21,23]. Reducing μ further causes δ to increase and this moves the peaks further from the commensurate (π, π) point. One also observes secondary structure in the spin susceptibility that is strongest along the diagonals—qualitatively similar to observations in past RPA studies [31]. A similar albeit weaker splitting near $\mathbf{q} = (\pi, \pi)$ is observed in χ_d . Rather than distinct peaks, we observe a nearly continuous diamond shape and primarily demonstrates an increase in signal along the boundaries, particularly near $\mathbf{q} = (0, 0)$.

A sharp (in momentum) peak should be observed in the case of long-ranged but static correlations. In our data, the absence of strong features in neither the charge nor the spin susceptibility below the van Hove point suggest that the origin of incompressibility seen in Fig. 3 is not a property of static nesting. This leaves only then the possibility of dynamical scattering which we explore in Sec. III D.

We note as well that the values of χ_s and χ_d at the Γ point of the Brillouin zone are not zero. This is due to the order of the limits $\lim_{q \rightarrow 0} \lim_{\Omega \rightarrow 0}$, where for static susceptibilities the zero-frequency limit is applied before the zero scattering-vector limit. Our results for dynamic susceptibilities ($\Omega \neq 0$) correctly represent the reverse order of the limit where for all nonzero frequencies the susceptibilities are zero when $\mathbf{q} = (0, 0)$.

D. Dynamical spin and charge collective excitations

Within our approach, the same calculations that provide the static $\mathbf{q} = (\pi, \pi)$ susceptibilities for arbitrary densities can be used to produce both finite real-frequency and Matsubara frequency results, in the thermodynamic limit, at arbitrary q vectors. Access to real frequency susceptibilities allows us

to examine the dispersive behavior of plasmon and magnon collective excitations. Much is known of charge excitations from studies of the two-dimensional electron gas [36] where the RPA chain of diagrams has a formal divergence resulting in a sharp quasiparticle peak. In this work we operate with a truncated expansion and therefore interpret peaks in the imaginary part of the charge susceptibility as plasmon excitations and similarly peaks in the spin susceptibility as magnon excitations. This interpretation is commonplace in the case of spin excitations where the cross section for magnetic neutron scattering is related to the imaginary part of the spin susceptibility [45].

We plot the dispersions of the spin and charge excitations in Fig. 5 for a range of doping at $U/t = 2.5$ and $\beta t = 5$ for momenta along the $\mathbf{q} = (0, q_y)$ direction. Beginning with the strongly electron doped case at $n = 0.8$, when accounting for the change in scale the dispersion of χ_s and χ_d are very similar, with both showing a linear form up to rather high energies. Since the difference between χ_s and χ_d is just $2\chi_{\uparrow\downarrow}$, this similarity suggests that $\chi_{\uparrow\uparrow}$ is the dominant contribution far from half filling. Reducing the density towards half filling ($n = 0.5$), the charge susceptibility remains linear but shows more incoherent signal at lower energies. This incoherence coincides with peaks in χ_s that show a more recognizable sine-function shape that is representative of linear spin-wave models [46–48]. Moving to the hole-doped cases, we observe a massive behavioral change at $n = 0.38$ (coinciding with the van Hove point at $\mu = -1.2$), where both the spin and charge excitations have split into two bands at finite q vectors and merge at small q vectors and low energy. The observation of splitting in χ_s and χ_d near the van Hove point suggests that this effect is likely due to the incompressibility observed in Fig. 3 where $\kappa \rightarrow 0$. This impacts the susceptibility due to renormalization of the single-particle propagator which occurs in diagrams that are part of the $\chi_{\uparrow\uparrow}$ expansion, the amplitude of which is shared by χ_s and χ_d . The splitting is therefore not due to vertex effects that are primarily a part of the $\chi_{\uparrow\downarrow}$ expansion (see Supplemental Materials [17]). Reducing the density further to the dilute limit, $n = 0.19$, we see that

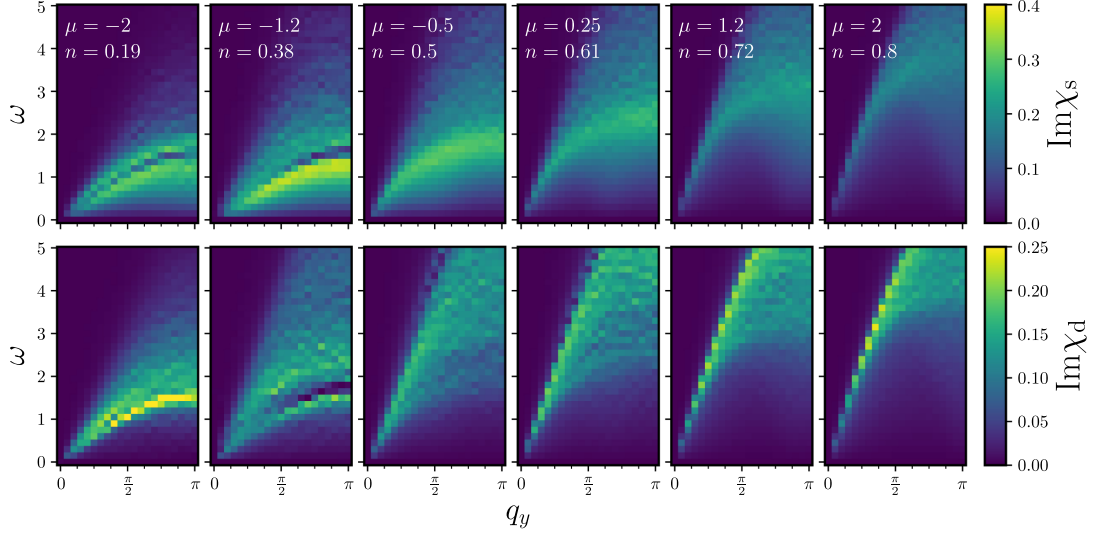


FIG. 5. Imaginary parts of $\chi_s(\omega, q)$ (top) and $\chi_d(\omega, q)$ (bottom) as a function of ω and $\mathbf{q} = (0, q_y)$ for $U/t = 2.5$, $t' = -0.3t$, and $\beta t = 5$ for a range of densities $n = 0.19 \rightarrow 0.8$.

the two-peak structure has closed in χ_d but remains in χ_s . We note a similarity in the overall shape of the dispersions of χ_s and χ_d as seen in the heavily electron doped case, suggesting again that $\chi_{\uparrow\uparrow}$ is the dominant contribution and that vertex effects are minimal.

We have tracked this splitting with density and find that it is strongest in proximity to the van Hove singularity that coincides with the associated incompressible phase shown in Fig. 3. We present a representative case in Fig. 6 (for additional data see Supplemental Materials [17] and references

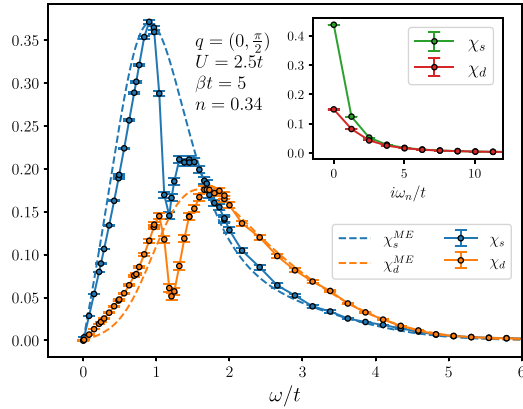


FIG. 6. The imaginary parts of $\chi_s(\omega, q)$ and $\chi_d(\omega, q)$ at $\mathbf{q} = (0, \pi/2)$ for a density of $n = 0.34$ produced via analytic continuation of $i\omega_n \rightarrow \omega + i\Gamma$ for the case of $\Gamma = 0.125$. The result of numerical analytic continuation via maximum entropy inversion (ME) is shown for reference with input from $\chi_s(i\omega_n)$ and $\chi_d(i\omega_n)$ shown in the inset.

within [49,50]), where a frequency cut of the dispersion at fixed $\mathbf{q} = (0, \pi/2)$ for a hole-doped case with $(n) = 0.4$ is shown for an interaction strength of $U/t = 2.5$ at $\beta t = 5$. We plot $\text{Im}\chi_s(\omega + i\Gamma)$ and $\text{Im}\chi_d(\omega + i\Gamma)$ in the main frame but also the result on the Matsubara axis, $\text{Re}\chi_s(i\omega_n)$ and $\text{Re}\chi_d(i\omega_n)$, in the inset. We stress that real-frequency and Matsubara axis results are the evaluation of the same analytic expressions. For connection to earlier works we present also the numerical analytic continuation of $\chi_s(i\omega_n) \rightarrow \chi_s^{ME}(\omega)$ and $\chi_d(i\omega_n) \rightarrow \chi_d^{ME}(\omega)$ via maximum entropy (ME) inversion. Results from ME are reminiscent of previous studies of the model [35,51,52], and while we see that the numerical analytic continuation has the same general shape and dominant peak location as the direct real-frequency evaluation, the result for $\chi_{s/d}^{ME}$ does not resolve the two-peak structure. This is not surprising and exemplifies the ill-posed nature of numerical analytic continuation. It remains an open question if improved numerical analytic continuation methods might resolve these distinctions [53,54]. Our results throughout this paper do not suffer from this issue, since they represent true analytic continuation, the symbolic replacement of $i\omega_n \rightarrow \omega + i\Gamma$ where the choice of Γ can in principle be made arbitrarily small.

At lowest order the charge susceptibility represents a direct transition from an occupied state at some energy ω and momentum k to an unoccupied state at $\omega + \Omega$ and momentum $k + q$. At zero temperature the lowest energy where one will find an unoccupied state is the Fermi level. At finite temperature there is of course a range of energies (on the scale of T) where unoccupied states will be available. Since the multipeak structures in Figs. 5 and 6 occur at finite frequency they cannot be related to static Fermi-surface nesting. To elucidate their origin, we plot in Fig. 7 the spectral function for the case of $U/t = 2.5$ at a density of $n = 0.34$ where the observed splitting is strong. Surprisingly, we observe that, at the bottom

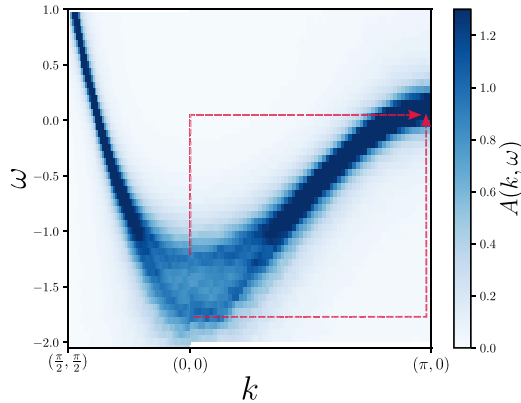


FIG. 7. The spectral density $A(k, \omega)$ along the path $\mathbf{k} = (\pi/2, \pi/2) \rightarrow (0, 0) \rightarrow X$ for the case shown in Fig. 6 evaluated up to fourth order. Dominant nonzero-frequency transitions from the bottom of the band to the $\mathbf{k} = (\pi, 0)$ antinodal point are marked in red.

of the band near $\mathbf{q} = (0, 0)$, the dispersion becomes split, albeit weakly. This behavior has been previously observed in perturbative calculations of spectral functions as well as dual-fermion calculations for comparable parameters [55,56]. In this particular case, instead of a single quasiparticle peak at energy $\omega = \mu = -1.4t$ we observe two peaks, one at $\omega = -1.2t$ and another near $\omega \sim -1.8t$. We can see that, in the case of the charge susceptibility, these peak locations correlate strongly with the peaks in Figs. 5 and 6. We surmise that finite-energy nesting comes into play because the dispersion is flat in the vicinity of both $k = (0, 0)$ and $(\pi, 0)$. There is then a roughly fixed energy transition from each peak at the bottom of the band to the $(\pi, 0)$ point—we illustrate this with dashed-red lines in Fig. 7. Furthermore, the van Hove singularity occurs precisely when the dispersion at $\mathbf{q} = (\pi, 0)$ meets the Fermi level and so this effect is expected to be strongest in the vicinity of the van Hove singularity of the Hartree-shifted starting point of the expansion.

IV. CONCLUSIONS

We have presented a complete and consistent picture of the formation of an incompressible phase in single-particle

properties of the $t - t' - U$ Hubbard model on a 2D square lattice when in proximity to the van Hove singularity. We have demonstrated the impact of the van Hove singularity on spin and charge excitations in the weak-coupling limit of the 2D Hubbard model from a perturbative perspective. By considering static and dynamic properties of the model, we observe a disconnect between spin excitations that are strongest in proximity to half filling from charge excitations that demonstrate a minima near the van Hove point. Through a simple argument based on susceptibilities in the $\chi_{\uparrow\uparrow} - \chi_{\uparrow\downarrow}$ basis, it becomes clear that commensurate charge excitations should be expected on both the electron and hole doped sides of the phase diagram while spin excitations, at the temperatures explored, remain fixed at half filling—although slightly on the hole-doped side for negative values of t' . We further examine the dynamical susceptibilities without the need for ill-posed numerical analytic continuation, providing access to plasmon and magnon dispersions. We observe a splitting both of the plasmon and magnon dispersions into two distinct modes that merge in the $q \rightarrow 0$ limit. Such splitting is similar to what has been observed at stronger coupling strengths for charge excitations in one-dimensional (1D) Hubbard chains due to the formation of a gap [57]. We note that multiple peaks only occur for densities near or below the van Hove point. Recent Raman experiments have suggested that the pseudogap phenomenon might terminate at the density associated with the Lifshitz point [58] which for a weakly coupled system coincides with the van Hove singularity. Although we are not directly computing the Raman spectra, our results would corroborate this observation. Our work has further implications to experimental probes of cuprates that have observed the existence of a high-energy plasmon and low-energy magnon for systems with particle-hole asymmetry [59–61]. Our results suggest that observing spin and charge excitations on the electron-doped side of the phase diagrams would require probing systems at higher energies than the hole-doped side.

ACKNOWLEDGMENTS

J.P.F.L. and G.T.A. acknowledge the support of the Natural Sciences and Engineering Research Council of Canada (NSERC) (RGPIN-2022-03882 and RGPIN-2015-04306). Computational resources were provided by ACENET and Compute Canada. Our Monte Carlo codes make use of the open source ALPSCORE framework [38,39].

-
- [1] J. P. F. LeBlanc, A. E. Antipov, F. Becca, I. W. Bulik, G. K.-L. Chan, C.-M. Chung, Y. Deng, M. Ferrero, T. M. Henderson, C. A. Jiménez-Hoyos, E. Kozik, X.-W. Liu, A. J. Millis, N. V. Prokof'ev, M. Qin, G. E. Scuseria, H. Shi, B. V. Svistunov, L. F. Tocchio, I. S. Tupitsyn *et al.* (Simons Collaboration on the Many-Electron Problem), *Phys. Rev. X* **5**, 041041 (2015).
- [2] E. W. Huang, C. B. Mendl, H.-C. Jiang, B. Moritz, and T. P. Devreux, *npj Quantum Mater.* **3**, 22 (2018).
- [3] B.-X. Zheng, C.-M. CHung, P. Corboz, G. Ehlers, M.-P. Qin, R. M. Noack, H. Shi, S. R. White, S. Zhang, and G. K.-L. Chan, *Science* **358**, 1155 (2017).
- [4] T. Esslinger, *Annu. Rev. Condens. Matter Phys.* **1**, 129 (2010).
- [5] E. Ibarra-García-Padilla, R. Mukherjee, R. G. Hulet, K. R. A. Hazzard, T. Paiva, and R. T. Scalettar, *Phys. Rev. A* **102**, 033340 (2020).
- [6] E. Gull, O. Parcollet, and A. J. Millis, *Phys. Rev. Lett.* **110**, 216405 (2013).

- [7] B.-X. Zheng and Garnet Kin-Lic Chan, *Phys. Rev. B* **93**, 035126 (2016).
- [8] H. Park, K. Haule, and G. Kotliar, *Phys. Rev. Lett.* **101**, 186403 (2008).
- [9] I. M. Vishik, W. S. Lee, R.-H. He, M. Hashimoto, Z. Hussain, T. P. Devereaux, and Z.-X. Shen, *New J. Phys.* **12**, 105008 (2010).
- [10] A. Virosztek and J. Ruvalds, *Phys. Rev. B* **42**, 4064 (1990).
- [11] T. M. Rice, K.-Y. Yang, and F. C. Zhang, *Rep. Prog. Phys.* **75**, 016502 (2012).
- [12] I. M. Vishik, *Rep. Prog. Phys.* **81**, 062501 (2018).
- [13] D. Chakraborty, M. Grandadam, M. H. Hamidian, J. C. S. Davis, Y. Sidis, and C. Pépin, *Phys. Rev. B* **100**, 224511 (2019).
- [14] J. P. F. LeBlanc, J. P. Carbotte, and E. J. Nicol, *Phys. Rev. B* **83**, 184506 (2011).
- [15] J. P. F. LeBlanc, *New J. Phys.* **16**, 113034 (2014).
- [16] A. Georges and G. Kotliar, *Phys. Rev. B* **45**, 6479 (1992).
- [17] See Supplemental Material at <http://link.aps.org/supplemental/10.1103/PhysRevB.106.035145> for additional results.
- [18] P. Werner, S. Hoshino, and H. Shinaoka, *Phys. Rev. B* **94**, 245134 (2016).
- [19] T. Schäfer, N. Wentzell, F. Šimkovic, Y.-Y. He, C. Hille, M. Klett, C. J. Eckhardt, B. Arzhang, V. Harkov, F. M. Le Régent, A. Kirsch, Y. Wang, A. J. Kim, E. Kozik, E. A. Stepanov, A. Kauch, S. Andergassen, P. Hansmann, D. Rohe, Y. M. Vilk *et al.*, *Phys. Rev. X* **11**, 011058 (2021).
- [20] Fedor Šimkovic, J. P. F. LeBlanc, A. J. Kim, Y. Deng, N. V. Prokof'ev, B. V. Svistunov, and E. Kozik, *Phys. Rev. Lett.* **124**, 017003 (2020).
- [21] B. Arzhang, A. E. Antipov, and J. P. F. LeBlanc, *Phys. Rev. B* **101**, 014430 (2020).
- [22] W. Wu, M. Ferrero, A. Georges, and E. Kozik, *Phys. Rev. B* **96**, 041105(R) (2017).
- [23] F. Šimkovic, R. Rossi, and M. Ferrero, [arXiv:2110.05863](https://arxiv.org/abs/2110.05863).
- [24] C. Hille, F. B. Kugler, C. J. Eckhardt, Y.-Y. He, A. Kauch, C. Honerkamp, A. Toschi, and S. Andergassen, *Phys. Rev. Research* **2**, 033372 (2020).
- [25] C. Hille, D. Rohe, C. Honerkamp, and S. Andergassen, *Phys. Rev. Research* **2**, 033068 (2020).
- [26] D. P. Arovas, E. Berg, S. A. Kivelson, and S. Raghu, *Annu. Rev. Condens. Matter Phys.* **13**, 239 (2022).
- [27] N. Furukawa, C. Honerkamp, M. Salmhofer, and T. Rice, *Phys. B (Amsterdam, Neth.)* **284–288**, 1571 (2000).
- [28] J. González, *Phys. Rev. B* **63**, 045114 (2001).
- [29] A. Taheridehkordi, S. H. Curnoe, and J. P. F. LeBlanc, *Phys. Rev. B* **99**, 035120 (2019).
- [30] A. Taheridehkordi, S. H. Curnoe, and J. P. F. LeBlanc, *Phys. Rev. B* **102**, 045115 (2020).
- [31] A. T. Rømer, A. Kreisel, I. Eremin, M. A. Malakhov, T. A. Maier, P. J. Hirschfeld, and B. M. Anderson, *Phys. Rev. B* **92**, 104505 (2015).
- [32] K.-S. Chen, Z. Y. Meng, T. Pruschke, J. Moreno, and M. Jarrell, *Phys. Rev. B* **86**, 165136 (2012).
- [33] M. R. Norman, J. Lin, and A. J. Millis, *Phys. Rev. B* **81**, 180513(R) (2010).
- [34] G. Rohringer, A. Valli, and A. Toschi, *Phys. Rev. B* **86**, 125114 (2012).
- [35] Y. F. Kung, E. A. Nowadnick, C. J. Jia, S. Johnston, B. Moritz, R. T. Scalettar, and T. P. Devereaux, *Phys. Rev. B* **92**, 195108 (2015).
- [36] I. S. Tupitsyn, A. M. Tselvik, R. M. Konik, and N. V. Prokof'ev, *Phys. Rev. Lett.* **127**, 026403 (2021).
- [37] J. Vučičević, P. Stipsić, and M. Ferrero, *Phys. Rev. Research* **3**, 023082 (2021).
- [38] A. Gaenko, A. Antipov, G. Carcassi, T. Chen, X. Chen, Q. Dong, L. Gamper, J. Gukelberger, R. Igarashi, S. Isakov, M. Könz, J. LeBlanc, R. Levy, P. Ma, J. Paki, H. Shinaoka, S. Todo, M. Troyer, and E. Gull, *Comput. Phys. Commun.* **213**, 235 (2017).
- [39] M. Wallerberger, S. Isakov, A. Gaenko, J. Kleinhenz, I. Krivenko, R. Levy, J. Li, H. Shinaoka, S. Todo, T. Chen, X. Chen, J. P. F. LeBlanc, J. E. Paki, H. Terletska, M. Troyer, and E. Gull, [arXiv:1811.08331](https://arxiv.org/abs/1811.08331).
- [40] H. Elazab, B. D. E. McNiven, and J. P. F. LeBlanc, [arXiv:2201.09868](https://arxiv.org/abs/2201.09868).
- [41] R. Levy, J. P. F. LeBlanc, and E. Gull, *Comput. Phys. Commun.* **215**, 149 (2017).
- [42] M. Jarrell and J. Gubernatis, *Phys. Rep.* **269**, 133 (1996).
- [43] X. Dong and E. Gull, *Phys. Rev. B* **101**, 195115 (2020).
- [44] O. Gunnarsson, T. Schäfer, J. P. F. LeBlanc, E. Gull, J. Merino, G. Sangiovanni, G. Rohringer, and A. Toschi, *Phys. Rev. Lett.* **114**, 236402 (2015).
- [45] H. F. Fong, B. Keimer, D. Reznik, D. L. Milius, and I. A. Aksay, *Phys. Rev. B* **54**, 6708 (1996).
- [46] R. Coldea, S. M. Hayden, G. Aeppli, T. G. Perring, C. D. Frost, T. E. Mason, S.-W. Cheong, and Z. Fisk, *Phys. Rev. Lett.* **86**, 5377 (2001).
- [47] J. P. F. LeBlanc, S. Li, X. Chen, R. Levy, A. E. Antipov, A. J. Millis, and E. Gull, *Phys. Rev. B* **100**, 075123 (2019).
- [48] A. H. MacDonald, S. M. Girvin, and D. Yoshioka, *Phys. Rev. B* **37**, 9753 (1988).
- [49] E. Gull, A. J. Millis, A. I. Lichtenstein, A. N. Rubtsov, M. Troyer, and P. Werner, *Rev. Mod. Phys.* **83**, 349 (2011).
- [50] A. E. Antipov, J. P. F. LeBlanc, and E. Gull, *Phys. Procedia* **68**, 43 (2015).
- [51] C. J. Jia, E. A. Nowadnick, K. Wohlfeld, Y. F. Kung, C.-C. Chen, S. Johnston, T. Tohyama, B. Moritz, and T. P. Devereaux, *Nat. Commun.* **5**, 3314 (2014).
- [52] E. W. Huang, D. J. Scalapino, T. A. Maier, B. Moritz, and T. P. Devereaux, *Phys. Rev. B* **96**, 020503(R) (2017).
- [53] J. Fei, C.-N. Yeh, and E. Gull, *Phys. Rev. Lett.* **126**, 056402 (2021).
- [54] J. Fei, C.-N. Yeh, D. Zgid, and E. Gull, *Phys. Rev. B* **104**, 165111 (2021).
- [55] J. Paki, Ph.D. thesis, University of Michigan, 2019, relevant data presented in Figs. 5.5 and 5.6.
- [56] B. D. E. McNiven, G. T. Andrews, and J. P. F. LeBlanc, *Phys. Rev. B* **104**, 125114 (2021).
- [57] S. Li, A. Nocera, U. Kumar, and S. Johnston, *Commun. Phys.* **4**, 217 (2021).
- [58] S. Benhabib, A. Sacuto, M. Civelli, I. Paul, M. Cazayous, Y. Gallais, M.-A. Méasson, R. D. Zhong, J. Schneeloch, G. D. Gu, D. Colson, and A. Forget, *Phys. Rev. Lett.* **114**, 147001 (2015).
- [59] J. Lin, J. Yuan, K. Jin, Z. Yin, G. Li, K.-J. Zhou, X. Lu, M. Dantz, T. Schmitt, H. Ding, H. Guo, M. P. M. Dean, and X. Liu, *npj Quantum Mater.* **5**, 4 (2020).

- [60] W. S. Lee, J. J. Lee, E. A. Nowadnick, S. Gerber, W. Tabis, S. W. Huang, V. N. Strocov, E. M. Motoyama, G. Yu, B. Moritz, H. Y. Huang, R. P. Wang, Y. B. Huang, W. B. Wu, C. T. Chen, D. J. Huang, M. Greven, T. Schmitt, Z. X. Shen, and T. P. Devereaux, *Nat. Phys.* **10**, 883 (2014).
- [61] M. Hepting, L. Chaix, E. W. Huang, R. Fumagalli, Y. Y. Peng, B. Moritz, K. Kummer, N. B. Brookes, W. C. Lee, M. Hashimoto, T. Sarkar, J.-F. He, C. R. Rotundu, Y. S. Lee, R. L. Greene, L. Braicovich, G. Ghiringhelli, Z. X. Shen, T. P. Devereaux, and W. S. Lee, *Nature (London)* **563**, 374 (2018).

Supplementary material for: One- and two-particle properties of the weakly interacting two-dimensional Hubbard model in proximity to the van Hove singularity

B. D. E. McNiven,¹ Hanna Terletska,² G. T. Andrews,¹ and J. P. F. LeBlanc^{1,*}

¹*Department of Physics and Physical Oceanography, Memorial University of Newfoundland, St. John's, Newfoundland & Labrador, Canada A1B 3X7*

²*Department of Physics and Astronomy, Computational Sciences Program, Middle Tennessee State University, Murfreesboro, TN 37132, USA*

Expansion	$N^{(0)}$	$N^{(1)}$	$N^{(2)}$	$N^{(3)}$	$N^{(4)}$	N^{terms}
$\chi_{\uparrow\uparrow}$	1	0	4	14	93	23,327
$\chi_{\uparrow\downarrow}$	0	1	2	13	78	17,954
D	0	1	2	13	78	52,644

TABLE I. Number of diagrams for the Hubbard interaction at order m , $N^{(m)}$ for each expansion, and total number of analytic terms after processing with AMI, N^{terms} .

I. SUPPLEMENTARY NOTE 1: DIAGRAMMATIC EXPANSIONS

We enumerate the number of diagrams at each order in the expansions of the susceptibilities $\chi_{\uparrow\uparrow}$ and $\chi_{\uparrow\downarrow}$ as well as the double occupancy D in Table I. The diagrammatic expansions include those diagrams that are one-particle reducible in the bosonic channel. We sketch the first few diagrams in Figure S1.

The final column of Table I shows the total number of analytic terms generated by AMI up to 4th order. While the RPA approximation includes only a single diagram comprised of two analytic terms, the data we present for χ_s and χ_d includes 41,281 analytic terms. In the case of the double occupancy the diagrammatic expansion is identical to that of $\chi_{\uparrow\downarrow}$ but includes an additional summation over the external bosonic Matsubara frequency. This results in substantially more terms and somewhat higher computational expense per term.

In the case of results presented on the real frequency axis, we restrict calculations to third order. While this is substantially fewer diagrams it still represents 1604 analytic terms, far beyond anything previously accessible.

II. SUPPLEMENTARY NOTE 2: COMPARISONS TO NON-PERTURBATIVE METHODS

A. Multi-peak Structure in Charge Susceptibility: DMFT+Dual Fermions

We compare the results of the static $\vec{q} = (\pi, \pi)$ spin and charge susceptibilities resulting from our many-body perturbation theory with algorithmic Matsubara integration

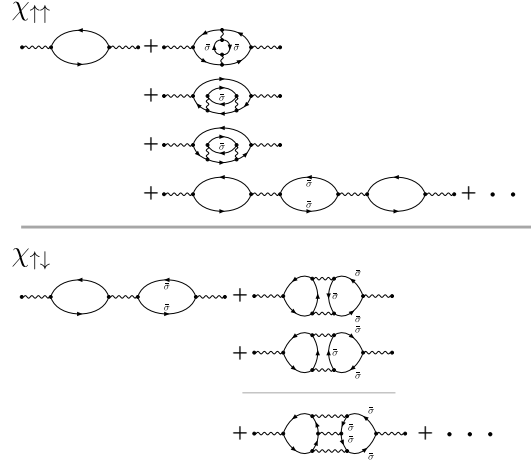


FIG. S1. First few diagrams in the expansions of $\chi_{\uparrow\uparrow}$ and $\chi_{\uparrow\downarrow}$. Due to the form of the Hubbard interaction, only interaction lines between propagators with opposite spins are non-zero. To track this, unmarked lines represent a spin choice σ and marked lines have spin $\bar{\sigma}$ that is defined to be the opposite to σ .

(MBPT+AMI) technique to that of a non-perturbative method, DMFT+DF, displayed in Fig. S2.[1, 2] We perform the DF calculation for a finite momentum resolution of 64×64 points. The calculation involves the measurement of the 4-point vertex function within DMFT, $F^{\nu\nu'\omega}$, which we obtain on a truncated grid $\nu = \nu' = \{-64, \dots, 64\}$ and $\omega = \{-24, \dots, 24\}$. While the DF method is approximate, reference data at half-filling supports that the spin susceptibility from the dual fermion method is virtually exact at this temperature.[3] In comparison to our AMI result, the spin susceptibility for our perturbative calculation, truncated at fourth order, agrees perfectly with the non-perturbative DF result. Since we compute $\chi_{\uparrow\uparrow}$ and $\chi_{\uparrow\downarrow}$ this implies that the AMI result for χ_d is equally correct. We see that the DF method underestimates the value of χ_d in comparison to our main result. This is due to a known bias in the self-consistency applied in the ladder dual-fermion method. Despite these small deviations we observe a two peak structure in DF data with the same peak locations from the non-perturbative calculation as those presented in the

* jleblanc@mun.ca

main paper. This shows that the multi-peak structure in the charge susceptibility is robust and not an artifact of our truncated perturbative expansion.

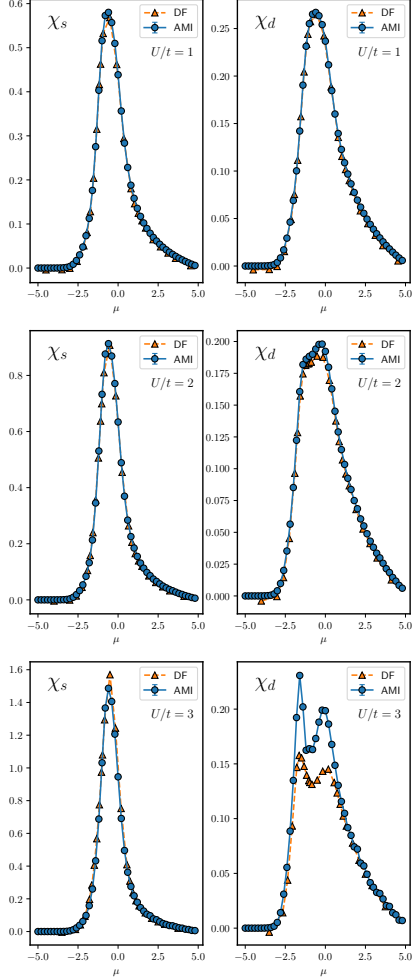


FIG. S2. Spin (left) and charge (right) susceptibilities for $\beta t = 5$, $t'/t = -0.3$ at $U/t = 1$ (top), 2 (middle), 3 (bottom). In addition to AMI data from this work we provide dual Fermion (DF) calculations for comparison.

B. Compressibility: DMFT

In the main paper we found that for weak-coupling the compressibility, $\kappa = \frac{\partial n}{\partial \mu}$, shows a suppression at a density that does not coincide with half-filling. We perform a similar study using the non-perturbative method

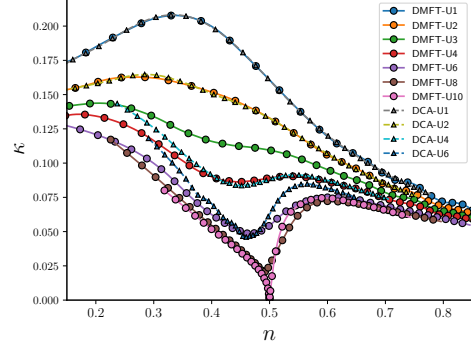


FIG. S3. Results for $\kappa = \frac{\partial n}{\partial \mu}$ at fixed $\beta t = 5$, $t' = -0.3$ from DMFT and 8-site DCA for variation in U/t .

of DMFT. Deviations between MBPT and DMFT are expected, since DMFT solves a single site impurity problem self-consistently while MBPT+AMI is in the thermodynamic limit of infinite system size. We present DMFT data in Fig. S3 where we observe a suppression in κ similar to that of MBPT+AMI that for $t' \neq 0$ occurs away from half-filling close to the van Hove point of the non-interacting system. Increasing the interaction strength causes the minimum in κ to move towards half-filling. We also performed calculations using the non-perturbative dynamical cluster approximation (DCA), an extension of DMFT, for a small 8-site cluster. We see that the compressibility obtained from DCA remains consistent with that of DMFT. Together, these results suggest that the reduction in κ away from $n = 0.5$ is a robust feature of the model, captured by both perturbative and non-perturbative methods.

C. Self-Energy

In the main paper we presented single-particle spectral data based on the truncation of our AMI perturbative expansion at fourth order. To assess the level of accuracy of such a truncation, in Fig. S4 we compare to the dynamical-cluster approximation (DCA). [1] We restrict this comparison to Matsubara axis data, from which we select a relevant temperature of $\beta t = 5$ at $U/t = 4$ for the half-filled case at the anti-nodal momentum point. We expect this comparison to be a worst-case scenario. We see that, due to finite size effects, the results of the fourth order perturbative calculation land between DCA calculations on 32- and 64-site clusters. We see that our fourth order results are quantitatively as accurate as a 64-site DCA calculation that suffers from finite-size effects. We note that the DCA data represents 'single-shot' calculations built on the non-interacting ex-

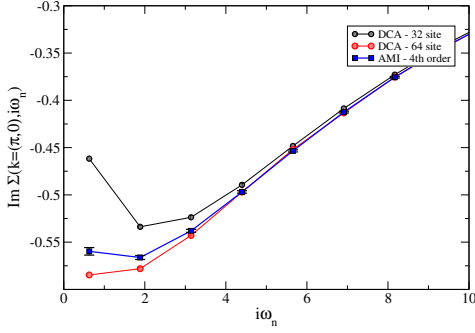


FIG. S4. Comparison of AMI self-energy data on the Matsubara axis, truncated at fourth order, to non-perturbative DCA method on a finite bipartite lattices of 32 and 64 sites. Data shown for $\beta t = 5$ at $U/t = 4$ for the half-filled case with $t' = 0$.

pansion rather than a typically iterated DCA loop. This data is therefore equivalent to finite sized determinantal quantum Monte-Carlo (DQMC) calculations.

III. SUPPLEMENTARY NOTE 3: ADDITIONAL DATA

A. Full μ Dependence at Low Order

The data presented in the main text Fig. (4) is sparse in choice of densities due to the computational effort required. We present in Fig. S5 lower order calculations, truncated at second order, but for a high resolution grid in chemical potential μ . The splitting in charge and spin excitations noted in the main text at third order exists also at second order. This demonstrates the robust nature of the additional structures in the charge and spin susceptibilities. We see a continual hardening of both spin and charge excitations for increase in chemical potential. We observe nothing particularly special at the half-filled density relative to densities nearby, but do note a maximal splitting in the charge excitations at chemical potentials near the van Hove point, near $\mu = -1.5 \rightarrow -1.2$.

B. Interaction Strength Dependence

We plot the spin and charge dispersions in Fig. S6 at fixed doping $n = 0.5$ and temperature for momenta along the $\vec{q} = (0, q_y)$ direction for increasing interaction strength. Both spin and charge susceptibilities exhibit clear dispersive behavior with peaks located within

a broad incoherent background with the charge excitations showing a linear behavior and occurring at energies above the peak in spin excitations. From the progression

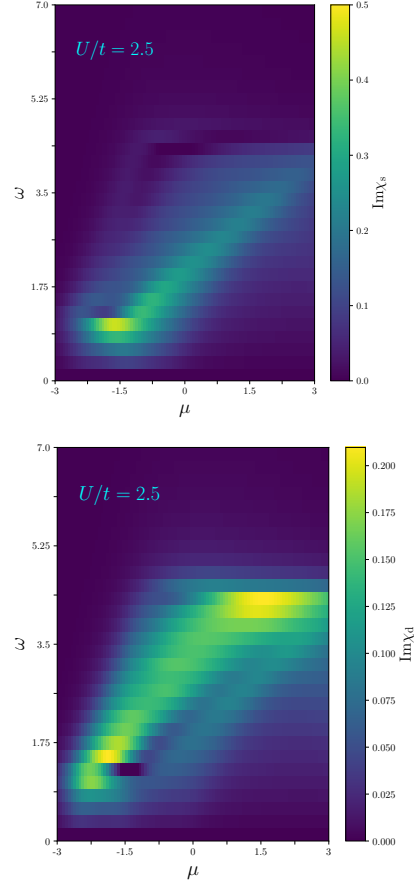


FIG. S5. Imaginary parts of the spin (Top) and charge (Bottom) susceptibilities truncated at second order with $U/t = 2.5$ over a range of μ and ω for $\vec{q} = (0, \pi/2)$. A broadening factor of $\Gamma = 0.125$ was used.

with interaction strength, we observe a straightforward increase in the spin susceptibility and broadening as U/t increases. In the case of the charge susceptibility, we see at $U/t = 3$ a weak splitting of the charge excitations into a lower and upper peak consistent with Fig. S5 and data presented in the main text.

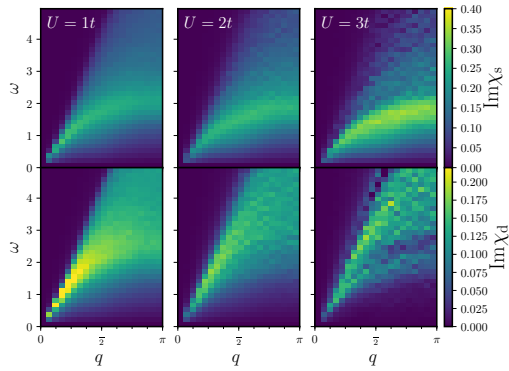


FIG. S6. Imaginary parts of $\chi_s(\omega, q)$ (top) and $\chi_d(\omega, q)$ (bottom) as a function of ω and $\vec{q} = (0, q_y)$ for $U/t = 1 \rightarrow 3$, $t' = -0.3$, and $\beta t = 5$ at a fixed density of $n = 0.5$. Calculations are truncated at third order, as in the main text for real frequency observables. A broadening factor of $\Gamma = 0.125t$ was used.

-
- [1] E. Gull, A. J. Millis, A. I. Lichtenstein, A. N. Rubtsov, M. Troyer, and P. Werner, *Rev. Mod. Phys.* **83**, 349 (2011).
- [2] A. E. Antipov, J. P. F. LeBlanc, and E. Gull, *Physics Procedia* **68**, 43 (2015), proceedings of the 28th Workshop on Computer Simulation Studies in Condensed Matter Physics (CSP2015).
- [3] T. Schäfer, N. Wentzell, F. Šimkovic, Y.-Y. He, C. Hille, M. Klett, C. J. Eckhardt, B. Arzhang, V. Harkov, F. m. c.-M. Le Régent, A. Kirsch, Y. Wang, A. J. Kim, E. Kozik, E. A. Stepanov, A. Kauch, S. Andergassen, P. Hansmann, D. Rohe, Y. M. Vilks, J. P. F. LeBlanc, S. Zhang, A.-M. S. Tremblay, M. Ferrero, O. Parcollet, and A. Georges, *Phys. Rev. X* **11**, 011058 (2021).

Chapter 4

Experimental studies on Bi-2212

4.1 Phonons

Phonons are defined as vibrational states and describe the elastic behavior of atoms in the crystal lattice. For the purposes of this thesis, the classical approach of assuming an infinite diatomic chain of two distinguishable atoms periodically aligned is sufficient to fully describe phonons. A schematic of such a system is shown Fig 4.1, where each atom has mass M_i ($i = 1, 2$) and an overall spring constant K . Restricting to just nearest neighbor interactions allows one to write Newton's second law as

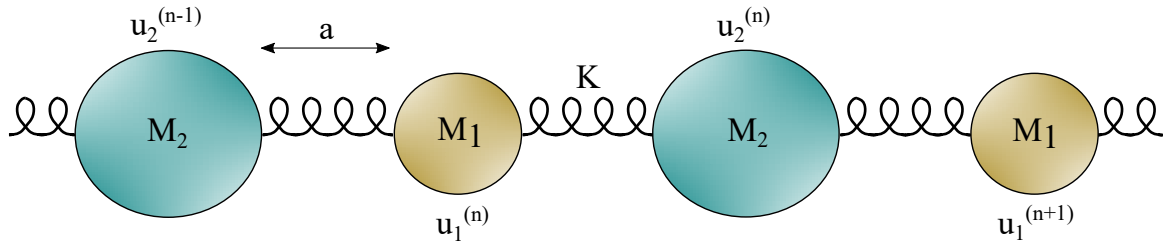


Figure 4.1: Linear diatomic chain of two distinguishable atoms, each with a respective mass of M_1 and M_2 and uniform spring constant K . Each atom is separated by distance a .

$$\begin{aligned} M_1 \ddot{u}_1 &= K(u_2^n - u_1^n) + K(u_2^{n-1} - u_1^n), \\ M_2 \ddot{u}_2 &= K(u_1^{n+1} - u_2^n) + K(u_1^n - u_2^n), \end{aligned} \tag{4.1}$$

where u_i^n ($i = 1, 2$ and $n \in [0, 1, 2, \dots, N - 1]$) represents the atomic deviation from the equilibrium position, and N is the total number of atoms. We are interested in a plane wave solution:

$$u_i = A_i e^{iqna - i\Omega t}, \quad (4.2)$$

where q is the wavevector, Ω is the angular frequency, t is time, and A_i is a constant. Upon substitution of into Eqn 4.2 into Eqn 4.1 and taking the second derivative, we find

$$\begin{aligned} -M_1\Omega^2 A_1 &= K(-2A_1 + A_2 + A_2 e^{-iqa}), \\ -M_2\Omega^2 A_2 &= K(-2A_2 + A_1 e^{iqa} + A_1). \end{aligned} \quad (4.3)$$

The set of linear equations only have a solution if the determinant is zero [1], hence we obtain

$$\begin{bmatrix} 2K - M_1\Omega^2 & -K(1 + e^{-iqa}) \\ -K(1 + e^{iqa}) & 2K - M_2\Omega^2 \end{bmatrix} \begin{bmatrix} A_1 \\ A_2 \end{bmatrix} = 0, \quad (4.4)$$

which can be expanded to yield

$$M_1 M_2 \Omega^4 - 2K\Omega^2(M_1 + M_2) + 2K^2(1 - \cos qa) = 0. \quad (4.5)$$

Using the small angle approximation $\cos ka \approx 1 - \frac{1}{2}q^2 a^2$ and solving for Ω^2 yields the following roots (valid for small q) [1]:

$$\begin{aligned} \Omega &= \sqrt{2K \left(\frac{1}{M_1} + \frac{1}{M_2} \right)}, \\ \Omega &= qa \sqrt{\frac{K}{2(M_1 + M_2)}}, \end{aligned} \quad (4.6)$$

which correspond to the optic and acoustic phonon branch, respectively.

Fig 4.2 shows a schematic of how optic and acoustic phonon branches evolve with increasing wavevector. As seen in the figure, optic phonons are higher energy and non-linear due to out of phase atomic vibrations. Conversely, acoustic phonons have an intercept at zero frequency, a frequency that is linear with increasing wavevector for small q , and are much lower in energy when compared to optic phonons due to in phase atomic vibrations [2].

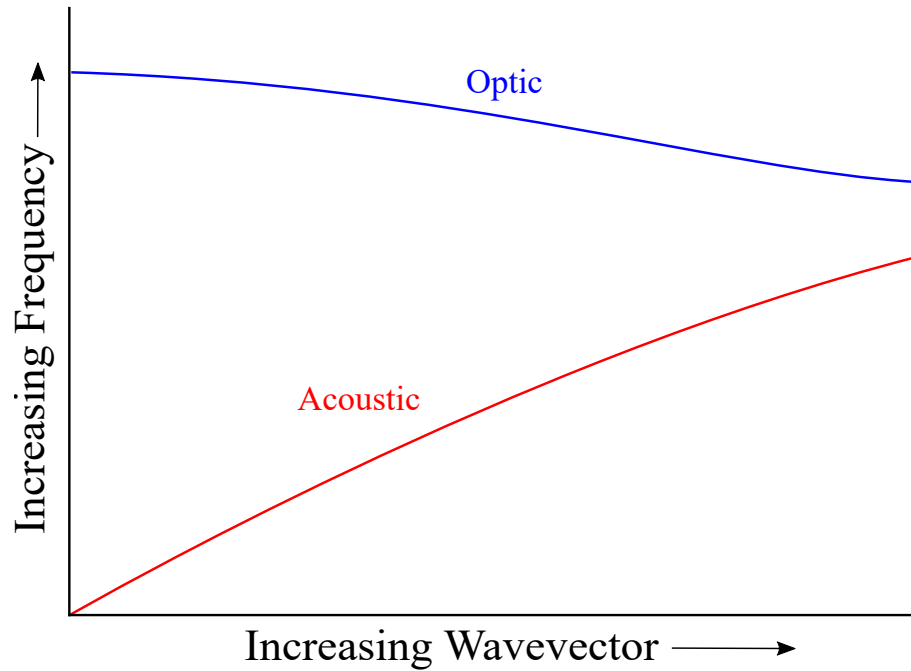


Figure 4.2: Schematic of the phonon dispersion curve confined to region where the acoustic branch is approximately linear.

4.2 Inelastic light scattering

Inelastic scattering events are governed by the conservation laws

$$\begin{aligned}\hbar\omega_s &= \hbar\omega_i \pm \hbar\Omega, \\ \hbar\mathbf{k}_s &= \hbar\mathbf{k}_i \pm \hbar\mathbf{q},\end{aligned}\tag{4.7}$$

where $\omega_i(\omega_s)$ is the angular frequency of the incident(scattered) photon, Ω is the angular frequency of the phonon, \mathbf{q} is the wavevector of the phonon, and $\mathbf{k}_i(\mathbf{k}_s)$ is the incident(scattered) wavevector of the photon [3]. Photons are scattered over a range of frequencies, and for crystalline materials, the overall scattering intensity depends not only on the transmission of light, but also on the scattering angle and crystallographic orientation relative to the incident light source [3].

Fig 4.3 shows a schematic example of what a typical crystalline solid spectrum looks like in an inelastic light scattering experiment. Inelastic peaks due to photon-phonon interaction are found on either side of the elastically scattered central line due to the scattered photon either losing or gaining energy in the scattering process (see Eqn

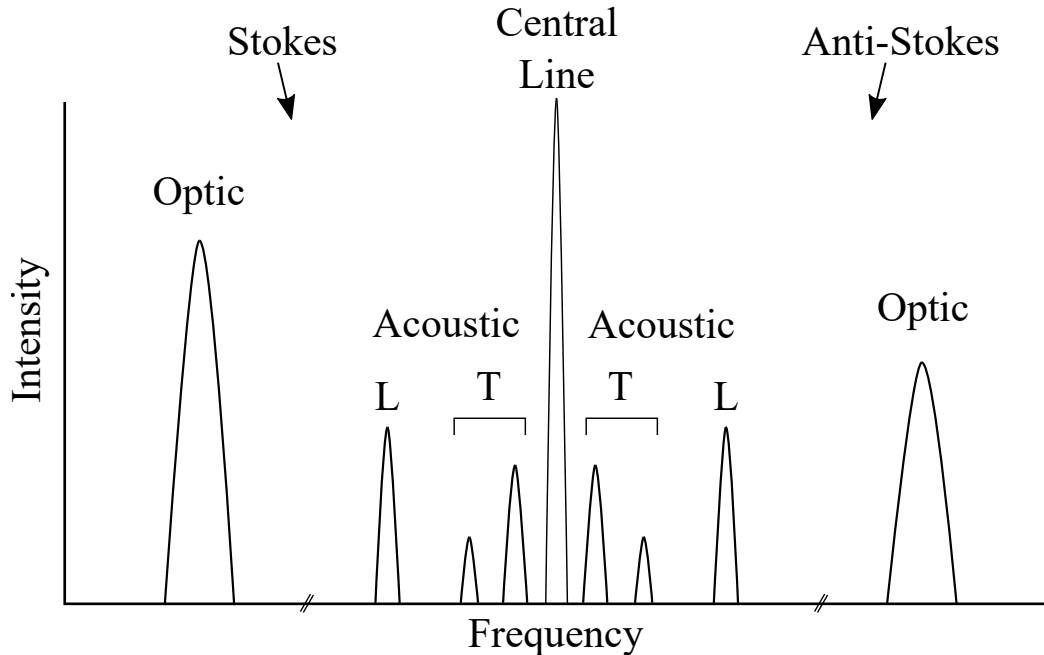


Figure 4.3: Schematic depicting a typical spectrum due to phonons for a typical crystalline solid for an inelastic light scattering experiment. T - bulk transverse acoustic, L - bulk longitudinal acoustic.

4.7). These processes are referred to as Stokes and Anti-Stokes scattering processes, respectively.

The inner three peaks from the elastic central line in Fig 4.3 correspond to the three bulk acoustic modes (as seen in Fig 4.2). These modes are symmetric about the central line and correspond to one bulk longitudinal (L) and two bulk transverse (T) acoustic phonon modes, where each has a frequency shift that is typically $\lesssim 30$ GHz ($< 1 \text{ cm}^{-1}$) [3]. Optic phonon modes typically occur at much higher frequency shifts ($10 - 1000 \text{ cm}^{-1}$ [3]) and as shown in the figure, have an asymmetric intensity between both Stokes and Anti-Stokes scattering peaks. This asymmetry is a result of Stokes and Anti-Stokes processes respectively requiring that a phonon either be already present in the material or created. This intensity asymmetry can be defined as

$$\frac{I^{AS}}{I^S} = e^{-\beta\hbar\Omega}, \quad (4.8)$$

where I is the intensity of the peak, S (AS) refers to Stokes (Anti-Stokes) scattering, and $\beta = 1/k_B T$.

4.2.1 Brillouin light scattering spectroscopy

Brillouin light scattering is an inelastic light scattering technique commonly used to investigate thermally excited acoustic phonons. The interaction between incident photons and acoustic phonons in a solid cause the photons to scatter by two means: the surface ripple mechanism and the bulk elasto-optic effect [4]. The surface ripple mechanism occurs when a photon that is incident on a solid is reflected from the surface due to surface deformation. This results in the wavevector of the scattered phonon having only a single component that is parallel to the solids surface. The bulk elasto-optic effect is a result of coupling between incident and scattered photons due to acoustic modulation of the solids dielectric constant.

Of vital importance surrounding the surface ripple and bulk elasto-optic mechanisms is the solids level of transparency [4]. For a transparent solid, incident light illuminates a large volume of the solid and the bulk elasto-optic mechanism is the dominant mechanism which produces photon scattering. This ultimately leads to sharp peaks due to bulk quasilongitudinal and quasitransverse acoustic phonons in the Brillouin spectrum. As the solid becomes more opaque, the imaginary parts of the optical wavevector destroy the conservation of the wavevector component perpendicular to the solids surface and lead to an increase in width of these acoustic phonon peaks in the Brillouin spectrum due to opacity broadening. For solids which are highly opaque, only the wavevector component parallel to the solids surface remains, leading to a Brillouin spectrum containing just a single peak due to the Rayleigh surface wave phonon. Further details surrounding the theory of Brillouin scattering from opaque solids and acoustic mode polarization can be found in Refs [5–7].

From Fig 4.4, one can apply Snell’s law to the conservation of momentum in Eqn 4.7 to define the parallel and perpendicular components of the phonon wavevector as

$$\begin{aligned} q_B^{\parallel} &= nk_i \sin \theta'_i + nk_s \sin \theta'_s, \\ q_B^{\perp} &= nk_i \cos \theta'_i + nk_s \cos \theta'_s, \end{aligned} \tag{4.9}$$

where n is the refractive index of the medium, k is the magnitude of the photon wavevector, and $\theta(\theta')$ is the external(internal) angle between the surface normal and the wavevector, and i and s subscripts correspond to incident and scattered, respectively. Given that the phonon velocity is much less than the speed of light, one can

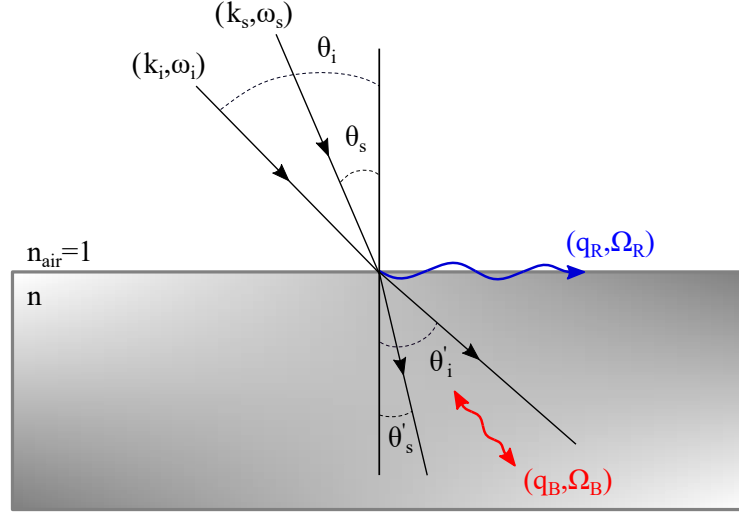


Figure 4.4: Schematic depicting the scattering process of incident photons with thermally excited acoustic phonons in a solid. k - photon wavevector, q - phonon wavevector, ω - photon frequency, Ω - phonon angular frequency, θ - external angle, θ' - internal angle, n - refractive index of the solid, R - Rayleigh surface mode, B - bulk acoustic phonon mode, i - incident, s - scattered.

assume $k_i \approx k_s$ and thus the magnitude of \mathbf{q}_B can be written as

$$q_B = nk_i \sqrt{2 + 2(\sin \theta'_i \sin \theta'_s + \cos \theta'_i \cos \theta'_s)}. \quad (4.10)$$

This can be further simplified using the identity $\sin \theta'_i \sin \theta'_s + \cos \theta'_i \cos \theta'_s = \cos(\theta'_i - \theta'_s)$ such that

$$q_B = nk_i \sqrt{2[1 + \cos(\theta'_i - \theta'_s)]}. \quad (4.11)$$

Using the conservation of energy in Eqn 4.7 and the fact that $\Omega = 2\pi f = vq$ and $k_i = 2\pi/\lambda_i$,

$$f_B = \frac{v_B n}{\lambda_i} \sqrt{2[1 + \cos(\theta'_i - \theta'_s)]}, \quad (4.12)$$

where f_B and v_B are the bulk phonon frequency and velocity respectively, and λ_i is the wavelength of the incident photon. Eqn 4.12 can be rewritten in the form

$$f_B = \frac{2v_B n}{\lambda_i} \sin\left(\frac{\Theta}{2}\right), \quad (4.13)$$

where the identity $\sin \frac{\Theta}{2} = \pm \sqrt{\frac{1 - \cos \Theta}{2}}$ has been used and $\Theta = \pi - \theta'_i + \theta'_s$ is the scattering angle. For backscattering geometry, as used in this thesis, $\Theta = 180^\circ$ and thus the bulk phonon velocity can be calculated via

$$v_B = \frac{f_B \lambda_i}{2n}. \quad (4.14)$$

Phonons propagating along the surface only have parallel wavevector component due to the exponential decay of amplitude with depth, resulting in a wavevector magnitude of magnitude of

$$q_R = q_B^{\parallel} = k_i \sin \theta_i + k_s \sin \theta_s. \quad (4.15)$$

Similar to the derivation above for bulk phonon velocities, the surface phonon velocity is equal to

$$v_R = \frac{f_R \lambda_i}{2 \sin \theta_i}, \quad (4.16)$$

where f_R and V_R are the surface phonon frequency and velocity, respectively. This relation is commonly used to describe the velocity of the surface Rayleigh phonon, however, other surface excitations, such as resonance modes [8], follow the same behaviour.

Lastly, we also note that for opaque materials where phonon lifetimes are negligible, the refractive index and extinction coefficient (κ) are related to the bulk acoustic phonon frequency shift and spectral linewidth (Γ) via [9]:

$$\frac{\Gamma}{f} = \frac{2\kappa}{n}. \quad (4.17)$$

Eqn. 4.17 is especially useful as the ratio of Γ and f from the Brillouin spectral profile are therefore related to many important optical properties of interest such as the penetration depth (d), optical absorption coefficient (α), and complex dielectric constant ($\tilde{\epsilon}$), each defined to be

$$\begin{aligned} d &= \frac{\lambda_i}{4\pi\kappa}, \\ \alpha &= \frac{1}{d}, \\ \tilde{\epsilon} &= (n^2 - \kappa^2) + i2n\kappa. \end{aligned} \quad (4.18)$$

4.3 Elastic theory in solids

For wavelengths much larger than the dimensions of the unit cell of the target material, the acoustic phonon modes measured in Brillouin scattering experiments behave as sound waves in a continuous medium and therefore can be described by macroscopic elasticity theory [3]. In such a situation, the equations of motion of the solid can be written as:

$$\rho \ddot{u}_i = \frac{\partial S_{ix}}{\partial x} + \frac{\partial S_{iy}}{\partial y} + \frac{\partial S_{iz}}{\partial z}, \quad (4.19)$$

where u is the perturbed displacement from equilibrium ($\mathbf{r} = \mathbf{r}_0 + \mathbf{u}(\mathbf{r}_0, t)$, where $\mathbf{r}_0 = x, y, z$) and ρ is the density. In Eqn 4.19, $S_{\alpha\beta}$ are the components of the second rank stress tensor equal to

$$S_{ij} = C_{ijkl} s_{kl}, \quad (4.20)$$

where C_{ijkl} is a component the rank four elastic stiffness tensor and s_{kl} is a component of the second rank strain tensor, equal to

$$s_{kl} = \frac{1}{2} \left(\frac{\partial u_i}{\partial x_j} + \frac{\partial u_j}{\partial x_i} \right). \quad (4.21)$$

With $x_\alpha = x, y, z$, Eqn 4.19 can be written in the general form [3]

$$\rho \ddot{u}_i = C_{ijkl} \frac{\partial^2 u_k}{\partial x_j \partial x_l}, \quad (4.22)$$

where ρ is the mass density. By assuming a plane wave solution and recalling the acoustic phonon velocity is equal to $v = \omega/q$, Eqn 4.22 can be written as

$$\rho v^2 u_i = C_{ijkl} e_j e_l u_k, \quad (4.23)$$

where $e_{j,l}$ = are directional cosines. While C_{ijkl} is a 9x9 tensor, utilizing the symmetry of both the stress and strain tensors, along with the fact that $C_{ijkl} = C_{klij}$, one ends up with a reduced 6x6 tensor with 21 independent components [10]. The number of independent components can be further reduced by considering the symmetry of the material. For cuprate systems which are either tetragonal or orthorhombic symmetry, this reduces the number of independent elastic components to six and nine, respectively, and will be discussed further in the following subsections.

By rewriting Eqn 4.23 as

$$\Gamma_{ik} - \rho v^2 \delta_{ik} = 0, \quad (4.24)$$

where $\Gamma_{ik} = C_{ijkl} e_j e_l$ and δ_{ik} is the Kronecker delta function, we obtain the Christoffel equation which allows one to determine the relationship between elastic constants and acoustic phonon velocities along specific propagation directions. Given Γ_{ik} is real and symmetric ($ik = ki$) its determinant can be written as

$$\begin{vmatrix} \Gamma_{11} - \rho v^2 & \Gamma_{12} & \Gamma_{13} \\ \Gamma_{12} & \Gamma_{22} - \rho v^2 & \Gamma_{23} \\ \Gamma_{13} & \Gamma_{23} & \Gamma_{33} - \rho v^2 \end{vmatrix} = 0, \quad (4.25)$$

where each of the six independent coefficients are [10]:

$$\begin{aligned} \Gamma_{11} &= e_x^2 C_{11} + e_y^2 C_{66} + e_z^2 C_{55} + e_y e_z 2C_{56} + e_x e_z 2C_{15} + e_x e_y 2C_{16} \\ \Gamma_{22} &= e_x^2 C_{66} + e_y^2 C_{22} + e_z^2 C_{44} + e_y e_z 2C_{24} + e_x e_z 2C_{46} + e_x e_y 2C_{26} \\ \Gamma_{33} &= e_x^2 C_{55} + e_y^2 C_{44} + e_z^2 C_{33} + e_y e_z 2C_{34} + e_x e_z 2C_{35} + e_x e_y 2C_{45} \\ \Gamma_{12} &= e_x^2 C_{16} + e_y^2 C_{26} + e_z^2 C_{45} + e_y e_z (C_{25} + C_{46}) + e_x e_z (C_{56} + C_{14}) + e_x e_y (C_{12} + C_{66}) \\ \Gamma_{13} &= e_x^2 C_{15} + e_y^2 C_{46} + e_z^2 C_{35} + e_y e_z (C_{45} + C_{36}) + e_x e_z (C_{13} + C_{55}) + e_x e_y (C_{14} + C_{56}) \\ \Gamma_{23} &= e_x^2 C_{56} + e_y^2 C_{24} + e_z^2 C_{34} + e_y e_z (C_{44} + C_{23}) + e_x e_z (C_{45} + C_{36}) + e_x e_y (C_{46} + C_{25}), \end{aligned} \quad (4.26)$$

where we have introduced the use of Voigt notation where $11 \rightarrow 1$, $22 \rightarrow 2$, $33 \rightarrow 3$, $23 \rightarrow 4$, $13 \rightarrow 5$, and $12 \rightarrow 6$.

Application to orthorhombic symmetry

For a system with orthorhombic symmetry, the elastic tensor is reduced to nine independent components:

$$C_{\alpha\beta} = \begin{pmatrix} C_{11} & C_{12} & C_{13} & 0 & 0 & 0 \\ C_{12} & C_{22} & C_{23} & 0 & 0 & 0 \\ C_{13} & C_{23} & C_{33} & 0 & 0 & 0 \\ 0 & 0 & 0 & C_{44} & 0 & 0 \\ 0 & 0 & 0 & 0 & C_{55} & 0 \\ 0 & 0 & 0 & 0 & 0 & C_{66} \end{pmatrix}, \quad (4.27)$$

where we have again introduced the use of Voigt notation. Given the reduction of nonzero elastic constants, Eqn 4.26 simplifies to give

$$\begin{aligned}
\Gamma_{11} &= e_x^2 C_{11} + e_y^2 C_{66} + e_z^2 C_{55}, \\
\Gamma_{22} &= e_x^2 C_{66} + e_y^2 C_{22} + e_z^2 C_{44}, \\
\Gamma_{33} &= e_x^2 C_{55} + e_y^2 C_{44} + e_z^2 C_{33}, \\
\Gamma_{12} &= e_x e_y (C_{12} + C_{66}), \\
\Gamma_{13} &= e_x e_z (C_{13} + C_{55}), \\
\Gamma_{23} &= e_y e_z (C_{44} + C_{23}).
\end{aligned} \tag{4.28}$$

From here, one just needs to select a propagation direction and solve Eqn 4.25 to determine the relationship between acoustic phonon velocities and the non-vanishing elastic constants. For example, if one is interested in elastic waves propagating in the [100] direction, one simply sets $e_x = 1$ and $e_y = e_z = 0$ resulting in $\Gamma_{11} = C_{11}$, $\Gamma_{22} = C_{66}$, and $\Gamma_{33} = C_{55}$ via Eqn 4.28. This leaves Eqn 4.25 as a simple diagonal matrix, yielding three trivial roots, shown in Table 4.1, along with the other high symmetry directions along the crystallographic axes of an orthorhombic structure.

Table 4.1: Bulk acoustic phonon velocities and the derived elastic constant quantity for a given phonon propagation direction for a crystal with orthorhombic symmetry.

Direction	Γ_{ik}	V_L	V_T
[100]	$\Gamma_{11} = C_{11}$ $\Gamma_{22} = C_{66}$ $\Gamma_{33} = C_{55}$	$\sqrt{\frac{C_{11}}{\rho}}$	$\sqrt{\frac{C_{55}}{\rho}}, \sqrt{\frac{C_{66}}{\rho}}$
[010]	$\Gamma_{11} = C_{66}$ $\Gamma_{22} = C_{22}$ $\Gamma_{33} = C_{44}$	$\sqrt{\frac{C_{22}}{\rho}}$	$\sqrt{\frac{C_{44}}{\rho}}, \sqrt{\frac{C_{66}}{\rho}}$
[001]	$\Gamma_{11} = C_{55}$ $\Gamma_{22} = C_{44}$ $\Gamma_{33} = C_{33}$	$\sqrt{\frac{C_{33}}{\rho}}$	$\sqrt{\frac{C_{44}}{\rho}}, \sqrt{\frac{C_{55}}{\rho}}$

Application to tetragonal symmetry

As shown in the previous section, the same application can be applied to crystals of tetragonal symmetry. The elastic constant tensor for such systems has six independent, non-zero components:

$$C_{\alpha\beta} = \begin{pmatrix} C_{11} & C_{12} & C_{13} & 0 & 0 & 0 \\ C_{12} & C_{11} & C_{13} & 0 & 0 & 0 \\ C_{13} & C_{13} & C_{33} & 0 & 0 & 0 \\ 0 & 0 & 0 & C_{44} & 0 & 0 \\ 0 & 0 & 0 & 0 & C_{44} & 0 \\ 0 & 0 & 0 & 0 & 0 & C_{66} \end{pmatrix}, \quad (4.29)$$

reducing Eqn 4.26 to:

$$\begin{aligned} \Gamma_{11} &= e_x^2 C_{11} + e_y^2 C_{66} + e_z^2 C_{44}, \\ \Gamma_{22} &= e_x^2 C_{66} + e_y^2 C_{11} + e_z^2 C_{44}, \\ \Gamma_{33} &= C_{44}(e_x^2 + e_y^2) + e_z^2 C_{33}, \\ \Gamma_{12} &= e_x e_y (C_{12} + C_{66}), \\ \Gamma_{13} &= e_x e_z (C_{13} + C_{44}), \\ \Gamma_{23} &= e_y e_z (C_{44} + C_{13}). \end{aligned} \quad (4.30)$$

By again considering the high symmetry directions along the three crystallographic axes, one obtains the elastic constant and velocity relations shown in Table 4.2.

Table 4.2: Bulk acoustic phonon velocities and the derived elastic constant quantity for a given phonon propagation direction for a crystal with tetragonal symmetry.

Direction	Γ_{ik}	V_L	V_T
[100]	$\Gamma_{11} = C_{11}$ $\Gamma_{22} = C_{66}$ $\Gamma_{33} = C_{44}$	$\sqrt{\frac{C_{11}}{\rho}}$	$\sqrt{\frac{C_{44}}{\rho}}, \sqrt{\frac{C_{66}}{\rho}}$
[010]	$\Gamma_{11} = C_{66}$ $\Gamma_{22} = C_{11}$ $\Gamma_{33} = C_{44}$	$\sqrt{\frac{C_{11}}{\rho}}$	$\sqrt{\frac{C_{44}}{\rho}}, \sqrt{\frac{C_{66}}{\rho}}$
[001]	$\Gamma_{11} = C_{44}$ $\Gamma_{22} = C_{44}$ $\Gamma_{33} = C_{33}$	$\sqrt{\frac{C_{33}}{\rho}}$	$\sqrt{\frac{C_{44}}{\rho}}$

4.3.1 Rayleigh surface velocity and elastic constants

In previous work surrounding the propagation of elastic surface waves in materials with orthorhombic symmetry [11], relationships between the Rayleigh surface velocity (i.e., the velocity of an acoustic phonon propagating along the material surface) and select elastic constants were derived. In general, the relationship is defined as

$$\sqrt{1 - \frac{\rho V_R^2}{C_{ii}}} \left[1 - \frac{C_{jk}^2}{C_{jj} C_{kk}} - \frac{\rho V_R^2}{C_{jj}} \right] = \sqrt{\frac{C_{jj}}{C_{kk}}} \left[\frac{\rho V_R^2}{C_{jj}} \right] \sqrt{1 - \frac{\rho V_R^2}{C_{jj}}}. \quad (4.31)$$

where the elastic constants subscripts for a particular direction of propagation and plane are shown in Table 4.3. These relationships are particularly useful in the case of Brillouin scattering experiments as the technique can directly observe the Rayleigh surface mode. Lastly, it is noted that in theory, Eqn 4.31 can also be applied to materials of tetragonal symmetry by considering $C_{11} = C_{22}$, $C_{13} = C_{23}$, and $C_{44} = C_{55}$.

Table 4.3: Elastic constants and identifying subscripts (i, j, k) in Eq. 4.31 for particular directions and planes of phonon propagation.

Direction	Plane	i, j, k	Elastic Constants
[010]	(100)	6, 2, 1	$C_{66}, C_{12}, C_{11}, C_{22}$
[001]	(100)	5, 3, 1	$C_{55}, C_{11}, C_{33}, C_{13}$
[100]	(010)	6, 1, 2	$C_{66}, C_{11}, C_{22}, C_{12}$
[001]	(010)	4, 3, 2	$C_{44}, C_{33}, C_{22}, C_{23}$
[010]	(001)	4, 2, 3	$C_{44}, C_{22}, C_{33}, C_{23}$
[100]	(001)	5, 1, 3	$C_{55}, C_{11}, C_{33}, C_{13}$

4.4 Aperiodic crystallography

Aperiodic, or incommensurate, crystals are systems which do not possess three-dimensional translational symmetry along one or more directions. Due to this, both their structure and symmetry are characterized in what is referred to as superspace (a d -dimensional space where $d > 3$) [12, 13]. To illustrate this, we define the generalized

formula for a wavevector,

$$\mathbf{q} = \sum_{i=1}^d m_i \mathbf{b}_i, \quad (4.32)$$

where d is the dimension, \mathbf{b}_i are the reciprocal space primitive lattice vectors, and m_i is any integer [2]. For a periodic, or commensurate, crystal there is translational symmetry present in three dimensions in all directions and thus there are three integer values of m_i and $d = 3$. For aperiodic crystals, one or more directions (i.e., the incommensurate direction(s)) result in $d = 3 + D$, where D are the additional superspace dimensions. As a general rule in aperiodic crystals, if the number of m_i values is not equal to d , the crystal is said to be aperiodic [14, 15]. Moreover, aperiodic structures are highly complex as their atomic positions exist at the planar intersection points between the three physical dimensions of real space and the additional D -dimensional atomic surface [14, 16, 17].

To date, aperiodic structures have been identified in compounds which include crystalline materials (such as minerals and van Der Waals heterostructures), inorganic and organic compounds, and molecular systems [15, 18]. Moreover, theoretical work surrounding aperiodic crystallography has led to the construction of three main subclasses of incommensurate systems [14, 19]; modulated structures, composite structures, and quasicrystals. Due to the complex nature of incommensurate crystals and scarcity of experimental data [12], many specific distinctions between these subclasses are still up for debate [17, 20]. For the purposes of this thesis, we restrict the following discussion to incommensurately modulated and composite structures and focus on the expected differences in their resulting phonon structure.

In the case of incommensurately modulated crystals, there are periodic atomic displacements which occur out of phase from the “lattice-symmetric” positions (i.e., equilibrium positions in a periodic lattice). The ratio of these two periodicities is an irrational number, leading to an incommensurate structure [12, 17]. Conversely, incommensurate composite crystals have no average translational symmetry as the unit cell is comprised of *at least* two incommensurate sublattice systems which are interacting and in many cases interpenetrated [21–23].

Fig 4.5 shows a simplified schematic lattice system for commensurate, incommensurate modulated (panel (b)), and incommensurate composite (panel (c)) crystals. In the case of the commensurate system shown in panel (a), a periodicity spans over

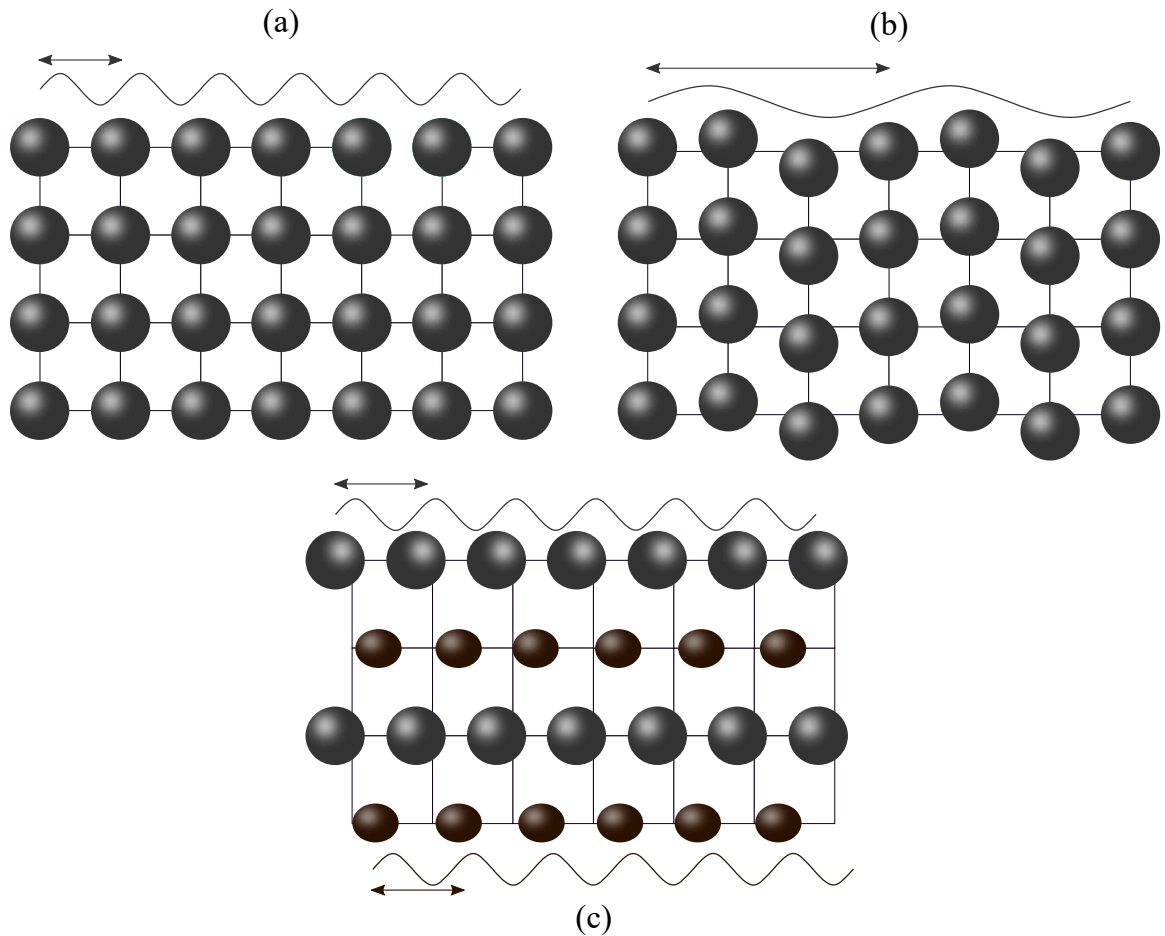


Figure 4.5: Schematic depicting the lattice system of a (a) commensurate (periodic) crystal, (b) incommensurate modulated crystal, and (c) incommensurate composite crystal.

the distance from the equilibrium lattice positions. For the incommensurately modulated system shown in panel (b), there is a displacive periodicity which is drastically different than that of the commensurate crystal. Lastly, in panel (c) depicting the composite crystal, there are two separate sublattice systems depicted by the gray and brown spheres. The overall structure has no periodicity in either the lattice-symmetric positions *or* in atomic displacivity, however each individual sublattice has a periodicity. More information regarding the atomic differences in these crystals may be found in Ref. [19].

In terms of vibrational structure, there will be obvious distinctions between lattice systems depicted in Fig. 4.5. While commensurate crystals will have $3N$ modes (as

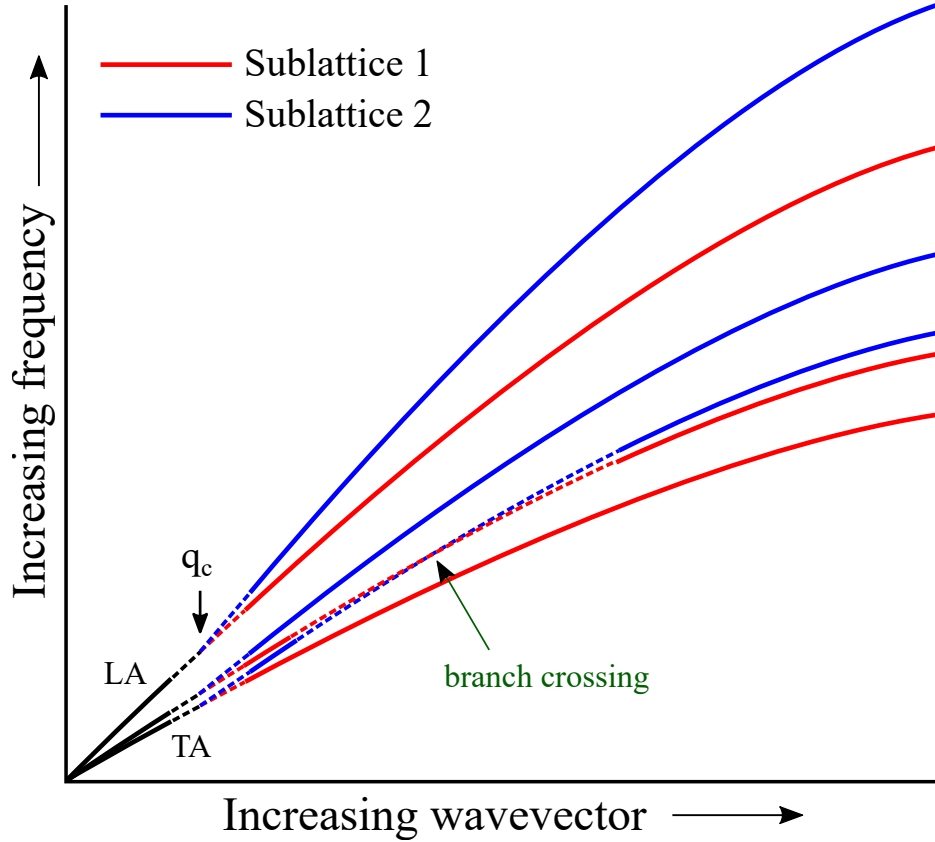


Figure 4.6: Schematic depicting the acoustic phonon dispersion along a general direction of an incommensurate composite system consisting of two sublattices. Dashed lines indicate branch crossing regions. q_c - crossover wavevector, LA - longitudinal acoustic phonon branch, TA - transverse acoustic phonon branches.

presented in section 4), this is not the case of incommensurate modulated or composite crystals as they do not possess true translational symmetry spanning in three dimensions [12]. While it is generally agreed upon that there are additional vibrational modes present in incommensurate crystals, their analysis and identification still remains unclear. For modulated structures, their averaged 3D translational symmetry means they have an acoustic phonon structure similar to that of commensurate systems, however, there also exist additional collective excitations, called phasons, which are a direct result of the atomic displacivity [17]. In the case of incommensurate composites, the unit cell contains a number of individual Brillouin zones proportional to the number of sublattices. This in turn means that for a composite system comprised of n sublattices, there will be n longitudinal acoustic phonons and $2n$ transverse acoustic phonons along the incommensurate direction [22].

While the full dynamical structure of phonons remains elusive in composites, we depict in Fig. 4.6 what a typical acoustic phonon dispersion along a general direction looks like for a composite crystal comprised of two sublattices based on the current theoretical models [17, 21, 22]. In the short-wavelength limit (large q), there are 2 longitudinal acoustic and 4 transverse acoustic phonon modes, while in the long-wavelength limit (small q), these modes become degenerate at a critical wavevector (q_c) and frequency (ω_c) crossover. Below this threshold, three acoustic modes exist; two averaged transverse acoustic phonon modes and one averaged longitudinal acoustic phonon mode. From a harmonic oscillator argument, the analytical function of the velocity of this averaged longitudinal phonon mode in the long-wavelength limit has been derived for a two sublattice system as [23]:

$$V_L^{q \rightarrow 0} = \sqrt{\frac{m_A V_{L_A}^2 + m_B V_{L_B}^2}{m_A + m_B}}, \quad (4.33)$$

where A and B refer to the two sublattices, however, an equivalent relationship for transverse acoustic phonon modes has not been explicitly derived.

Also shown in Fig. 4.6 are regions of potential branch crossings (indicated by dashed lines). Due to the lack of experimental data on incommensurate systems, it is unclear how the phonon dynamics change at these crossover regions, and if there are branch crossings for $(\omega, q) > (\omega_c, q_c)$ as indicated in the figure.

4.5 Acoustic phonons & elastic constants of Bi-2212

4.5.1 Brillouin light scattering measurements

To date, three Brillouin light scattering experiments have been performed on Bi-2212 [24–26]. Collectively, these works provide solid preliminary information surrounding the surface modes at room-temperature, however, present limited data surrounding bulk acoustic modes due to poor single crystal growing techniques for cuprates at the time of publication [27]. To date, no temperature dependent Brillouin studies exist on Bi-2212 or any cuprate system.

The first reported Brillouin spectra of Bi-2212 were presented on single crystal samples at room-temperature [24]. Only two surface acoustic modes were observed, the longitudinal surface resonance (LR) and the Rayleigh surface (R) modes. The resulting velocities were estimated to be $v_{LR} = 4650 \pm 300$ m/s and $v_R = 1525 \pm 150$ m/s, respectively, in an unspecified direction on the (001) plane. An independent study also presented surface Rayleigh velocities equal to 1560 m/s and 1310 m/s for the [100] and [010] directions, respectively, on the same plane [25]. However, this study focused on crystals grown with different stoichiometric ratios during the crystal growing process, which ultimately results in samples with varying crystal quality and vastly different dopant levels ($10 \text{ K} \leq T_c \leq 88 \text{ K}$).

Ref. [26] contains the most thorough Brillouin scattering study on crystalline Bi-2212 to date. Single crystals with a T_c ranging between 78 – 92 K were probed at multiple high symmetry directions on the ab and ac planes, however, only limited information could be obtained due to poor sample quality. In total, one bulk longitudinal and two bulk transverse acoustic phonons were observed, along with the Rayleigh surface (R) and longitudinal surface resonance modes (LR). A loose approximation was made whereby $V_R \approx V_T$ and $V_{LR} \approx V_L$ on specific directions to obtain the elastic constant estimates $C_{11} = 125$ GPa and $C_{33} = 76$ GPa. These estimates were used to obtain numerical estimates of $C_{12} = 79$ GPa, $C_{13} = 56$ GPa, and $C_{44} = 16$ GPa.

4.5.2 Ultrasonic measurements

Three ultrasonic studies have been performed on polycrystalline Bi-2212 with samples exhibiting a preferred grain orientation along the c-axis [28–30].

For work presented in Ref. [28], measurements along an unspecified direction yielded longitudinal (V_L) and transverse (V_T) acoustic phonon velocities of $V_L = 2847$ m/s and $V_T = 1740$ m/s. Using a model described in Ref. [31], these velocities were used to determine the void-free acoustic phonon velocities (i.e., velocities accounting for sample porosity) as 3110 m/s and 1900 m/s, respectively. These velocities are comparable to another ultrasonic study on polycrystalline Bi-2212 which yielded $V_L = 2670$ m/s and $V_T = 1750$ m/s along an arbitrary direction, while a second unknown direction resulted in $V_L = 4370$ m/s, $V_{T_1} = 1956$ m/s, and $V_{T_2} = 2311$ m/s, where the two independent transverse acoustic phonon modes are a result of preferential grain orientation [29].

This observation is similar to data presented in Ref. [30]. In this study, ultrasonic measurements were conducted on polycrystalline Bi-2212 samples produced by two different methods; sinter forging and hot isostatic pressing. Along the crystallographic c-axis, it was determined that the former samples yielded $V_L = 2464$ m/s and $V_T = 1710$ m/s, while measurements on the latter samples resulted in $V_L = 3330$ m/s and $V_T = 1968$ m/s. Additional measurements in the ab-plane of each set of samples yielded $V_L \approx 4000$ m/s, $V_{T_1} \approx 1700$ m/s, and $V_{T_2} \approx 2400$ m/s. The latter set of samples revealed a similar longitudinal velocity, however the transverse velocities were measured as $V_{T_1} \approx 2000$ m/s and $V_{T_1} \approx 2300$ m/s.

Ultrasonic measurements on single crystal Bi-2212 have also been conducted over wide temperature ranges. In Ref. [32, 33], longitudinal sound waves were propagated along the a and b crystallographic axes which yielded velocities of ~ 4580 m/s and ~ 4150 m/s respectively. With a systematic temperature decrease to ~ 8 K, anomalous phase-like transitions were observed at ~ 250 K, 150 K, and 90 K. Shear waves were also propagated along the crystallographic b-axis, where a velocity of ~ 2460 m/s was determined near room temperature.

In Refs. [34, 35], authors performed additional ultrasonic measurements on flux grown Bi-2212 single crystals to study the dependence of temperature on propagating longitudinal and shear waves and their resulting elastic constants. At 250 K, longitudinal velocities along the crystallographic a and b axes were measured to be within $\lesssim 5\%$ of those obtained previously near room temperature [32, 33]. Shear waves along the b-axis at the same temperature yielded a velocity of 2762 m/s, $\sim 11\%$ larger than that presented in Ref. [32, 33]. With orthorhombic crystal symmetry and a quoted density of 6600 kg/m³, these velocities were used to calculate the elastic constants $C_{11} = 123$ GPa, $C_{12} = 67$ GPa, $C_{22} = 111$ GPa and $C_{66} = 50$ GPa at 250 K, with the latter two in agreement with those obtained at room temperature from previous Brillouin scattering experiments [26]. Upon decreasing the temperature, stiffening was present in both C_{11} and C_{22} , while three minima were observed in C_{66} at 100 K, 140 K, and 240 K, similar to those seen previously [32, 33], which were attributed to instabilities caused by geometric misfit layers.

4.5.3 Inelastic neutron scattering measurements

Perhaps the most interesting study to date surrounding the acoustic phonon dynamics in Bi-2212 is presented in Ref. [36]. In this work, the incommensurate structure within the BiO and SrO layers are studied at room temperature using high quality, single crystal samples. In particular, the three crystallographic axes were probed. Along the a and c axes, a single transverse mode is observed, each with an estimated velocity of 3000 m/s and 1830 m/s respectively. Along the b-axis however, two independent longitudinal phonons were observed, each with an estimated velocity of 2400 m/s and 5900 m/s. The result of two independent longitudinal acoustic phonon modes is significant as it implies the superstructure contained in Bi-2212 cannot be incommensurately modulated as previously surmised as such a structure would produce only one longitudinal phonon mode. The authors indicate that these findings are more in-line with the so-called incommensurate composite model, which describes a system comprised of two sublattices which produces two separate longitudinal acoustic phonons (one for each sublattice) at large wavevectors (q) that degenerate to a single propagating longitudinal mode as $q \rightarrow 0$. The authors note that use of their estimated longitudinal velocities, along with a previously derived result which determines the $q \rightarrow 0$ velocity by consideration of the two independent longitudinal velocities and each sublattice mass [23, 37], yields an estimated long-wavelength longitudinal velocity in close proximity to the previously mentioned b-axis measurements of Bi-2212 via ultrasonic measurements [32, 33]. These experiments were repeated on Bi-2201 [38], which also showed a presence of two independent longitudinal acoustic phonons, suggesting all BiSrCaCuO compounds which exhibit an incommensurate structure are not simply incommensurately modulated.

4.6 Bi-2212 Samples

Bi-2212 samples subject to experimentation in this work were provided by Dr. Pat Clancy (McMaster University). In particular, three bulk single crystal samples were studied, each with a T_c of 78 K, 90 K, and 91 K (corresponding to oxygen dopant content of ~ 0.12 , ~ 0.16 , and ~ 0.17 , respectively, as seen in Fig. 1.6) and a cleavage plane perpendicular to the crystallographic c-axis.

Double sided adhesive tape was used to mechanically exfoliate small flakes from each

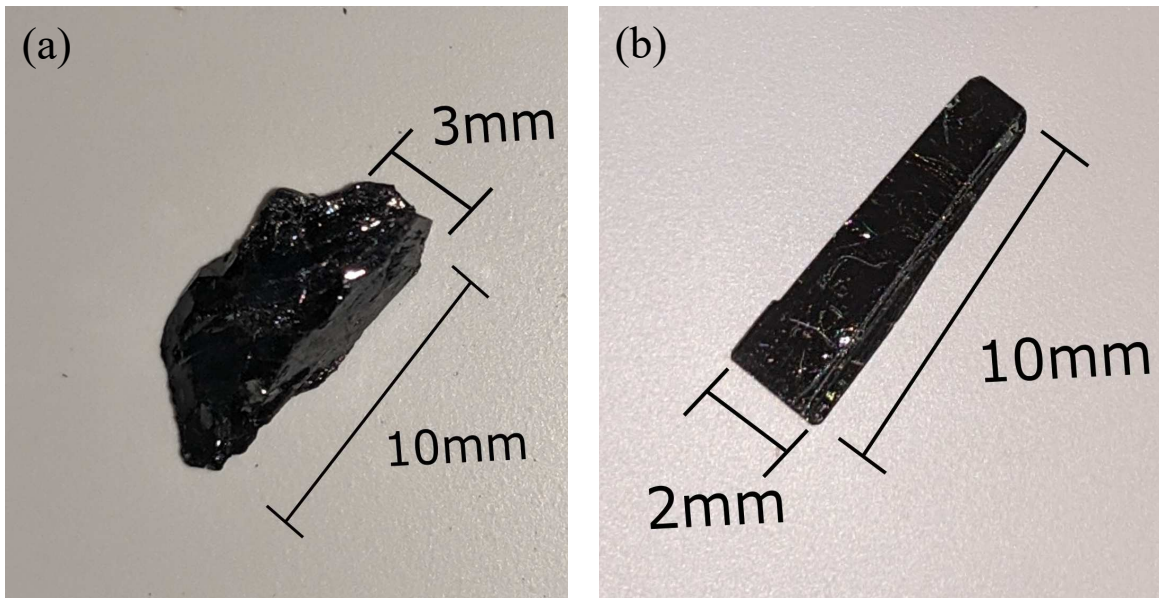


Figure 4.7: Parent Bi-2212 samples with (a) $T_c = 78$ K and (b) $T_c = 91$ K. Note $T_c = 90$ K is not shown as it is nearly identical in appearance and dimension to the $T_c = 91$ K parent crystal. Original images are found in Ref. [39].

bulk parent sample (see Fig. 4.7) and mounted to the sample stage in the Brillouin apparatus. These exfoliated flakes had estimated thicknesses ranging from ~ 0.05 to several mm. Extra care was taken to ensure the surface of the flakes was as pristine as possible to obtain the largest achievable signal-to-noise ratio. Further details surrounding these samples may be found in Ref. [39].

4.7 Brillouin scattering apparatus

Fig 4.8 shows a schematic of the Brillouin light scattering apparatus with backscattering geometry used in this thesis. Light is emitted from a Nd:YVO₄ laser source which has a wavelength of 532 nm and an output power of 1.63 W. The incident beam is first attenuated by passing through a variable neutral density filter, after which is passed through a half-wave plate to change the incident light from vertical (V) to horizontal (H) polarization. The beam then passes through a beam splitter, where part of the incident light is reflected back on an angle, and the remaining portion is transmitted through. The reflected portion acts as a reference beam for the six-pass tandem Fabry-Perot interferometer (FPI) used to analyze the optical signal. It first

passes through an aperture where it is reflected by a mirror to another variable neutral density filter before passing through the reference pin hole of the FPI.

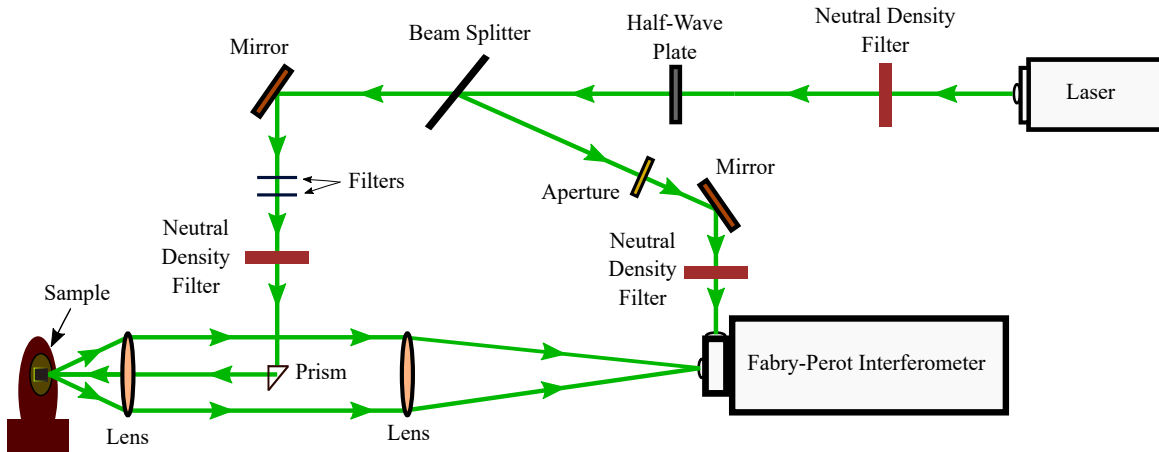


Figure 4.8: Schematic depicting the Brillouin light scattering apparatus used in this work.

The remaining incident light which has transmitted through the beam splitter is reflected by 90° and further attenuated via several filters to a power of ~ 10 mW to avoid sample heating and/or damage. The beam is then totally internally reflected by a right angle prism, where it first passes through a Nikon camera lens of focal length 5 cm and an aperture of $f/2.8$ and subsequently strikes the sample which is mounted a rotation stage which allows for the incident angle to be fixed between $0^\circ - 80^\circ$. The incident light scattered from the sample is then collected and collimated by the camera lens and then passes through a focusing lens with a focal length of 40 cm which focuses the scattered light onto the entrance pinhole of the FPI. The size of the pinhole is set to either $300 \mu\text{m}$ or $450 \mu\text{m}$, the former being selected when the width of the central elastic peak needed to be reduced to reveal Brillouin peaks at very small frequency shifts close to the laser line. Lastly, it is noted that when necessary, a polarizer was placed between the focusing lens and the entrance pinhole of the FPI to allow for the collection of HH (pp) and HV (ps) polarized spectra.

Fig 4.9 shows a schematic of the JRS Scientific Instruments manufactured tandem FPI used to analyze the scattered light. As shown in the figure, the tandem FPI is constructed of two FPIs (FPI_1 and FPI_2), each of which consists of two partially reflective planar mirrors that are each separated by a distance d_i ($i = 1, 2$). For scattered light which has entered the tandem FPI and is normally incident on $\text{FPI}_{1,2}$, only that which constructively interferes will pass through, meaning the scattered

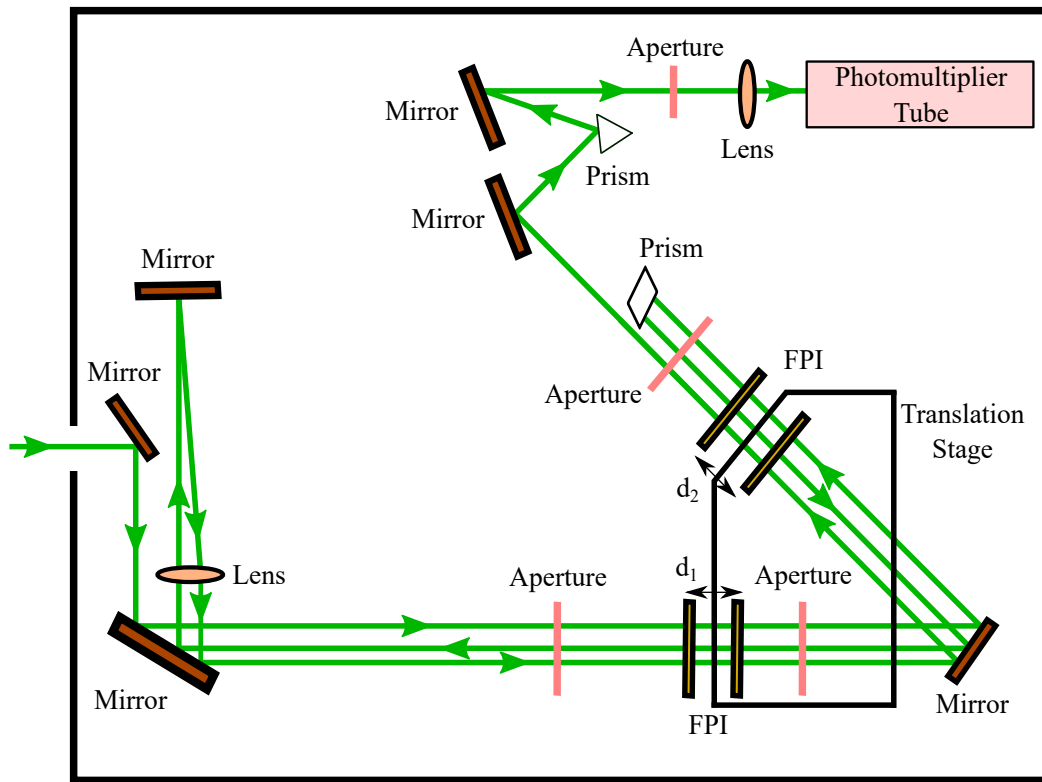


Figure 4.9: Schematic depicting the six-pass tandem Fabry Perot interferometer used in this work.

light must satisfy the condition for constructive interference:

$$d_i = \frac{m\lambda_m}{2} = \frac{mc}{2f_m}. \quad (4.34)$$

Here, m is any integer, λ_m (f_m) is the m^{th} wavelength (frequency) corresponding to constructive interference, and c is the speed of light. An analogous way to describe this is in terms of allowed transmitted frequencies:

$$f_m = \frac{mc}{2d_i} = mf_{FSR}, \quad (4.35)$$

where f_{FSR} is the free spectral range (FSR), or the difference in frequency between two consecutive transmission maxima.

As seen in Fig 4.9, light with a frequency that meets the requirements of Eqn. 4.35 is passed through FPI₁ and FPI₂ a combined total of six times before it is focused onto the entrance pinhole of a photomultiplier tube which converts the photon signal

to an electronic signal to display on a computer. Due to the relatively weak signal acquired by acoustic phonons, Fabry-Perot interferometry is an ideal instrument to detect these excitations as the contrast (i.e., signal-to-noise ratio) is increased with each pass through FPI_{1,2} [40]. From knowledge of the elastic peaks full-width at half-maximum (Γ_E) and f_{FSR} , the finesse of the tandem FPI setup can be determined by

$$\mathcal{F} = \frac{f_{FSR}}{\Gamma_E}. \quad (4.36)$$

Bibliography

- [1] C. Kittel, *Introduction to Solid State Physics - 8th Edition*. (Wiley Publisher, 2004).
- [2] M. P. Marder, *Condensed matter physics* (John Wiley & Sons, 2010).
- [3] W. Hayes and R. Loudon, *Scattering of Light by Solids* (Wiley-Interscience, 1978).
- [4] R. Loudon and J. R. Sandercock, *J. Solid State Phys* **13**, 2609 (1980).
- [5] K. R. Subbaswamy and A. A. Maradudin, *Phys. Rev. B* **18**, 4181 (1978).
- [6] N. L. Rowell and G. I. Stegeman, *Phys. Rev. B* **18**, 2598 (1978).
- [7] P. A. FLEURY (Academic Press, 1970) pp. 1–64.
- [8] R. E. Camley and F. Nizzoli, *J. Phys. C: Solid State Phys.* **18**, 4795 (1985).
- [9] J. Sandercock, *Phys. Rev. Lett.* **28**, 237 (1972).
- [10] C. Malgrange, C. Ricolleau, and M. Schlenker, *Symmetry and physical properties of crystals* (Springer, 2014).
- [11] R. Stoneley, *Geophys. J. Int.* **8**, 176 (1963).
- [12] D. Schmicker and S. van Smaalen, *Int. J. Mod. Phys. B* **10**, 2049 (1996).
- [13] T. Janssen, A. Janner, A. Looijenga-Vos, and P. De Wolff, *International tables for crystallography* **100**, 907 (2006).
- [14] T. Janssen and A. Janner, *Adv. Phys.* **36**, 519 (1987).

- [15] G. Chapuis and A. Arakcheeva, *Rend. Fis. Acc. Lincei* **24**, 77 (2013).
- [16] T. Janssen and J. A. Tjon, *J. Phys. C: Solid State Phys.* **16**, 4789 (1983).
- [17] O. Radulescu, T. Janssen and J. Etrillard, *Eur. Phys. J. B* **29**, 385 (2002).
- [18] Z. Zhu, P. Cazeaux, M. Luskin, and E. Kaxiras, *Phys. Rev. B* **101**, 224107 (2020).
- [19] S. Van Smaalen, *Incommensurate crystallography*, Vol. 21 (OUP Oxford, 2007).
- [20] T. Janssen, O. Radulescu, and A. Rubtsov, *Eur. Phys. J. B* **29**, 85 (2002).
- [21] R. Currat, E. Kats, and I. Luk'yanchuk, *Eur. Phys. J. B* **26**, 339 (2002).
- [22] J. Axe and P. Bak, *Phys. Rev. B* **26**, 4963 (1982).
- [23] W. Finger and T. M. Rice, *Phys. Rev. B* **28**, 340 (1983).
- [24] P. Baumgart, S. Blumenröder, A. Erle, B. Hillebrands, P. Splittgerber, G. Güntherodt and H. Schmidt, *Physica C* **162-164**, 1073 (1989).
- [25] V. V. Aleksandrov, T. S. Velichkina, V. I. Voronkova, A. A. Gippius, S. V. Rek'ko, I. A. Yakovlev and V. K. Yanovskii, *Solid State Commun.* **76**, 685 (1990).
- [26] M. Boekholt, J.V. Harzer, B. Hillebrands and G. Güntherodt, *Physica C* **179**, 101 (1991).
- [27] R. Laudise, L. Schneemeyer, and R. Barns, *J. Cryst. Growth* **85**, 569 (1987).
- [28] L. Sihan, H. Yusheng, W. Chongde and S. Zhaohui, *Supercond. Sci. Tech.* **2**, 145 (1990).
- [29] F. Chang, P.J. Ford, G.A. Saunders, L. Jiaqiang, D.P. Almond, B. Chapman, M. Cankurtaran, R.B. Poeppel and K.C. Goretta, *Supercond. Sci. Tech.* **6**, 184 (1993).
- [30] C. Y. Chu, J. L. Routbort, N. Chen, A. C. Biondo, D. S. Kupperman and K. C. Goretta, *Supercond. Sci. Tech.* **5**, 306 (1992).
- [31] H. M. Ledbetter and S. K. Datta, *J. Acoust. Soc. Am.* **79**, 239 (1986).

- [32] Y. Wang, J. Wu, J. Zhu, H. Shen, Y. Yan and Z. Zhao, *Physica C* **162-164**, 454 (1989).
- [33] Y. Wang, J. Wu, J. Zhu, H. Shen, J. Zhang, Y. Yang, and Z. Zhao, in *Beijing International Conference on High Temperature Superconductivity*, Vol. 22 (World Scientific Beijing, 1989) pp. 426–429.
- [34] J. Wu, Y. Wang, H. Shen and J. Zhu, *Phys. Lett. A* **148**, 127 (1990).
- [35] J. Wu, Y. Wang, P. Guo, H. Shen, *Phys. Rev. B* **47**, 2806 (1993).
- [36] J. Etrillard, Ph Bourges, H.F. He, B. Keimer, B. Liang and C.T. Lin, *EPL* **55**, 201 (2001).
- [37] W. Finger and T. M. Rice, *Phys. Rev. Lett.* **49**, 468 (1982).
- [38] J. Etrillard, L. Bourges, B. Liang, C.T. Lin and B. Keimer, *Europhys. Lett.* **66**, 246 (2004).
- [39] B. D. E. McNiven, *Optical Properties and Acoustic Phonon Dynamics of $Bi_2Sr_2CaCu_2O_{8+\delta}$ Crystals*, Master's thesis, Memorial University of Newfoundland (2020).
- [40] R. Mock, B. Hillebrands, and R. Sandercock, *J. Phys. E: Sci. Instrum.* **20**, 656 (1987).

Chapter 5

Experimental publications

5.1 Optical constants of crystalline $\text{Bi}_2\text{Sr}_2\text{CaCu}_2\text{O}_{8+\delta}$ by Brillouin light scattering spectroscopy

In this section, we reproduce the preprint version of the manuscript titled “Optical constants of crystalline $\text{Bi}_2\text{Sr}_2\text{CaCu}_2\text{O}_{8+\delta}$ by Brillouin light scattering spectroscopy” presented in Superconductor Science and Technology 34, 065005 (2021), with permission from authors B. D. E. McNiven, J. P. F. LeBlanc, and G. T. Andrews.

© IOP Publishing. Reproduced with permission. All rights reserved.

Optical Constants of Crystalline $\text{Bi}_2\text{Sr}_2\text{CaCu}_2\text{O}_{8+\delta}$ by Brillouin Light Scattering Spectroscopy

B. D. E. McNiven,¹ J. P. F. LeBlanc,¹ and G. T. Andrews^{1,*}

¹*Department of Physics and Physical Oceanography, Memorial University of Newfoundland, St. John's, Newfoundland & Labrador, Canada A1B 3X7*

(Dated: March 1, 2024)

Room-temperature optical constants of crystalline $\text{Bi}_2\text{Sr}_2\text{CaCu}_2\text{O}_{8+\delta}$ were determined using data extracted from Brillouin light scattering spectra. Optical extinction coefficient-to-refractive index ratios at a wavelength of 532 nm were obtained from bulk phonon peak linewidth and frequency shift measurements and range from $0.19 \leq 2\kappa/n \leq 0.29$ for directions close to the crystallographic c -axis. These ratios, and optical extinction coefficients, absorption coefficients, and imaginary parts of the dielectric function determined from these ratios and known refractive index, are in general agreement with values found in optical reflectance studies, but are 5-7 times larger than those extracted from optical interference measurements.

INTRODUCTION

$\text{Bi}_2\text{Sr}_2\text{CaCu}_2\text{O}_{8+\delta}$ (Bi-2212) is one of three commonly studied crystalline phases of the high- T_c superconductor $\text{Bi}_2\text{Sr}_2\text{Ca}_{n-1}\text{Cu}_n\text{O}_{2n+4+\delta}$ (BSCCO). Similar to other members of the cuprate family, Bi-2212 possesses orthorhombic symmetry and has been described as micaceous due to its layered morphology, with a cleavage plane perpendicular to the crystallographic c -axis [1]. Bi-2212 is structurally complex, exhibiting birefringence [2] and incommensurability due to sublattice coupling along the b and c crystallographic axes [3, 4].

Many properties of Bi-2212, especially the electronic and structural properties, have been studied in detail [3, 5], but the optical properties have received relatively little attention. Measurements of the dielectric function at visible wavelengths are scant and, with the exception of one study [6], report only the real [7] or imaginary [8] part of this quantity in this region of the electromagnetic spectrum. Furthermore, there is significant variation in these values. Two independent measurements of the complex refractive index of Bi-2212 have been reported [9, 10] but, while the real parts of this quantity lie within 5% of one another, the imaginary parts (*i.e.*, the extinction coefficients) differ by about a factor of 5. Moreover, a third value of extinction coefficient extracted from a measurement of optical penetration depth [6] is more than an order of magnitude greater than the lowest value reported in these three studies. It is therefore clear that additional studies of the optical properties of Bi-2212 are necessary to establish the true values of optical constants which appear in the literature and to broaden the knowledge base on these properties through characterization of as yet unmeasured optical constants.

In this paper, room-temperature optical extinction coefficient-to-refractive index ratios for a Bi-2212 crystal at the commonly-used wavelength of 532 nm are extracted from Brillouin spectra by measurement of bulk acoustic mode peak frequency shifts and linewidths.

Knowledge of these ratios, together with published refractive index values, allows optical extinction coefficients to be determined and, consequently, other optical properties via the Kramers-Kronig transformations.

EXPERIMENTAL DETAILS

Sample

The Bi-2212 crystal used in the present study was grown by the flux method [11] and has a critical temperature $T_c = 78$ K. A $1 \times 1 \times 0.5$ mm³ (001)-oriented sample for Brillouin scattering experiments was obtained from a parent crystal using mechanical exfoliation. This turned out to be somewhat challenging due to the irregular shape of the sample.

Brillouin Light Scattering Experiments

Brillouin scattering experiments were carried out in air at room temperature using a backscattering geometry (see Fig. 1) with the set-up shown in ref. [12]. A single mode Nd:YVO₄ laser emitting at a wavelength of $\lambda_i = 532$ nm served as the incident light source. To minimize reflection losses, the polarization of the laser beam was rotated from vertical to horizontal by use of a half-wave plate. It was then passed through attenuating filters to reduce the power to ~ 10 mW and subsequently focused onto the sample using a $f = 5$ cm lens with $f/\# = 2.8$. Scattered light was collected and collimated by the same lens and focused by a $f = 40$ cm lens onto the entrance pinhole ($d = 450$ μm) of a six-pass tandem Fabry-Perot interferometer which frequency-analyzed the scattered light. The free spectral range of the interferometer was set to 30 GHz. It should be noted that the use of such a low incident light power level was necessary to avoid sample damage and thermal effects caused by optical absorption; trial runs at power levels of ≥ 20 mW

generated noticeable sample heating and/or damage. As a result, spectrum acquisition times of ~ 20 hours were required and even in these circumstances only limited data could be obtained.

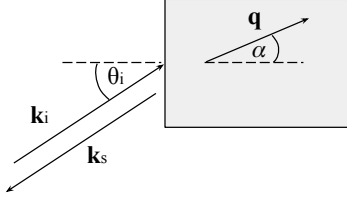


Figure 1: Backscattering geometry for Brillouin scattering experiments. \mathbf{k}_i (\mathbf{k}_s) - incident (scattered) photon wavevector; \mathbf{q} - phonon wavevector; θ_i - angle of incidence; α - direction of bulk acoustic phonon propagation as measured from the crystallographic c-axis.

RESULTS AND DISCUSSION

Brillouin Spectra

Fig. 2 shows room-temperature spectra of Bi-2212 collected at incident angles $20^\circ \leq \theta_i \leq 60^\circ$. The peak associated with the Rayleigh surface mode (R) was identified by the characteristic linear dependence of its frequency shift on $\sin \theta_i$ [13] and its narrow linewidth relative to those of bulk mode peaks in the spectra of opaque solids.

The peak of primary importance for this study (B) is due to a bulk acoustic mode. This assignment is based upon the relatively large width of B compared to that of the R peak and the fact that the frequency shift is essentially independent of θ_i over the range probed. It is noted that while previous Brillouin studies have explicitly assigned longitudinal or transverse character to spectral peaks originating from bulk modes [14], such information is not required to extract optical constants of Bi-2212 via the method used in the present study. This is especially fortuitous given that neutron scattering studies [3, 15] reveal the potential for multiple bulk acoustic modes (more than the usual three) in the spectrum of Bi-2212 due to its incommensurate nature, thereby complicating what is usually routine assignment of spectral peaks to either quasi-transverse or quasi-longitudinal modes.

Table I shows the peak frequency shift (f_B) and physical linewidth (Γ_B) for peak B at various incident angles. Frequency shifts were obtained directly from Lorentzian fits to the raw as-collected Brillouin peaks. The Γ_B values were obtained by subtracting the instrumental width (0.28 GHz, the width of the central elastic peak) from the fitted linewidth. This method for obtaining the phys-

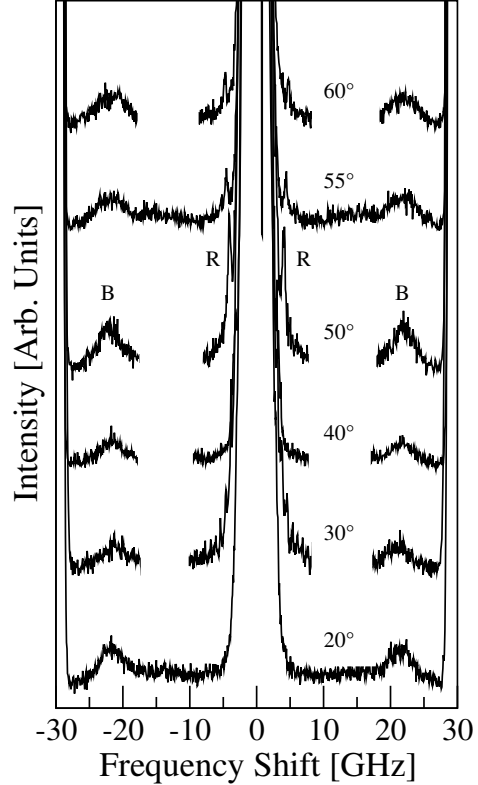


Figure 2: Room-temperature Brillouin spectra of crystalline Bi-2212 collected at incident angles ranging from $20^\circ \leq \theta_i \leq 60^\circ$. R - Rayleigh surface acoustic mode peak; B - bulk acoustic mode peak. Note: To avoid confusion, spectral regions containing a strong signal from sample mounting tape were removed. This unwanted signal swamped features that might otherwise have been observed, including weak Brillouin peaks known to be located in this spectral region [14].

ical linewidth makes use of the fact that the convolution of two Lorentzian profiles is a Lorentzian of width equal to the sum of the widths of the two constituent Lorentzians [16], and that the instrumental function and measured Brillouin peak profiles can be well-represented by Lorentzian functions [17, 18]. It also requires that the contribution of aperture broadening to the measured linewidth be negligibly small. This was confirmed in experiments on a strongly-scattering source (acrylic) in which the difference in Brillouin linewidths obtained using collection apertures of $f/2.8$ and $f/22$ was immeasurably small. Other studies have also shown that aperture broadening is very small when a backscattering geometry is employed [19].

Table I: Bulk acoustic mode frequency shifts (f_B) and associated linewidths (Γ_B) obtained from Brillouin spectra of crystalline $\text{Bi}_2\text{Sr}_2\text{CaCu}_2\text{O}_{8+\delta}$. θ_i - incident angle; S (A) - Stokes (Anti-Stokes) scattering.

θ_i [deg]	f_B^S [± 0.1 GHz]	Γ_B^S [GHz]	Γ_B^S/f_B^S	f_B^A [± 0.1 GHz]	Γ_B^A [GHz]	Γ_B^A/f_B^A
20	21.6	4.4(2)	0.20(1)	21.4	4.6(3)	0.21(1)
30	21.3	6.5(6)	0.31(3)	21.0	6.1(5)	0.29(1)
40	21.6	4.2(3)	0.19(1)	21.6	4.1(2)	0.19(1)
50	21.9	5.7(5)	0.26(2)	21.8	4.2(5)	0.25(3)
55	21.6	5.7(3)	0.26(1)	21.6	5.7(4)	0.26(2)
60	21.6	6.4(4)	0.30(2)	21.8	5.8(3)	0.27(1)

Determination of Optical Constants

The refractive index (n) and extinction coefficient (κ) for an opaque material are related to the bulk Brillouin peak linewidth, Γ_B , and frequency shift, f_B , through the equation

$$\frac{\Gamma_B}{f_B} = \frac{2\kappa}{n}, \quad (1)$$

when κ is large enough so that the contribution of phonon lifetime effects to the linewidth are negligible [20].

To obtain optical extinction coefficient-to-refractive index ratios for crystalline Bi-2212, the function

$$g(\xi) = w_B^S \left[\frac{\Gamma_B^S}{f_B^S} - \xi \right]^2 + w_B^A \left[\frac{\Gamma_B^A}{f_B^A} - \xi \right]^2 \quad (2)$$

was constructed, where $\xi = 2\kappa/n$, and w_B^S and w_B^A are weighting factors equal to the reciprocals of the variances in Γ_B^S/f_B^S and Γ_B^A/f_B^A , respectively. The value of this function is a minimum when

$$\xi = \frac{w_B^S \left[\frac{\Gamma_B^S}{f_B^S} \right] + w_B^A \left[\frac{\Gamma_B^A}{f_B^A} \right]}{w_B^S + w_B^A}. \quad (3)$$

Values of $\xi = 2\kappa/n$ can then be obtained by direct substitution of pairs of Γ_B^i/f_B^i ($i = S, A$) for a given direction from Table I into Eq. 3.

Table II shows values of $2\kappa/n$ at 532 nm obtained using the method described above, along with derived quantities and literature values of other related optical constants. As can be seen, the extinction coefficient-to-refractive index ratios $2\kappa/n$ obtained in the present work lie in the range $0.19 \leq 2\kappa/n \leq 0.29$ and show reasonably good agreement with those determined using n and κ values from a reflectance spectroscopy study [10]. In contrast, values of these ratios extracted from the results of a combined reflectance-ellipsometry approach [6] and optical interference [9] are $\sim 50\%$ higher and 5-7 times smaller than those of the present study, respectively.

Previous studies place the refractive index of Bi-2212 at 532 nm within 5% of a mean value of $n = 2.0$, but extinction coefficients reported in the same studies show an order of magnitude variation: $0.04 \leq \kappa \leq 0.42$ (see Table II) [6, 9, 10]. Using the $2\kappa/n$ ratios of the present work and the tightly constrained refractive index of $n = 2.0$ gives extinction coefficients for directions close to the c -axis of $0.19 \leq \kappa \leq 0.29$. These values are in good agreement with those determined using optical reflectance methods [6, 10], but are ~ 7 times larger than those obtained via optical interference [9]. Similar behaviour is seen for the optical absorption coefficient ($\alpha = 4\pi\kappa/\lambda_i$), optical penetration depth ($d = 1/\alpha$), and imaginary part of the dielectric function ($\epsilon_2 = 2n\kappa$) due to the strong dependence of these quantities on κ . On the contrary, the real part of the dielectric function $\epsilon_1 = n^2 - \kappa^2$ obtained using a refractive index of $n = 2.0$ and the κ values of the present study, are similar to those of all other studies listed in Table II [6, 9, 10] due to the fact that $n^2 \gg \kappa^2$.

CONCLUSION

Brillouin light scattering spectroscopy was used to determine room temperature optical constants of crystalline Bi-2212 at a wavelength of 532 nm. Extinction coefficient-to-refractive index ratios, and optical extinction coefficients, absorption coefficients, and imaginary parts of the dielectric function determined from these ratios and known refractive index, are consistent with values found in optical reflectance studies, but are several times larger than those obtained from optical interference measurements. The real part of the dielectric function determined in this study is in general agreement with those of several previous studies.

ACKNOWLEDGEMENTS

The authors would like to acknowledge Dr. J. P. Clancy at McMaster University, Canada, for supplying the samples used in this work and Dr. J. Hwang at Sungkyunkwan University, South Korea, for provid-

Table II: Room-temperature optical properties of crystalline $\text{Bi}_2\text{Sr}_2\text{CaCu}_2\text{O}_{8+\delta}$ at a wavelength of 532 nm. T_c - critical temperature; n - refractive index; κ - extinction coefficient; α - optical absorption coefficient; d - optical penetration depth; ϵ_1 - real part of dielectric function; ϵ_2 - imaginary part of dielectric function. Entries in the “Direction” column specify the direction of incident light propagation inside the material, as measured from the crystallographic c -axis. The arrows in the “ κ ” column indicate that the κ values are the same as the corresponding values of $2\kappa/n$ for $n = 2.0$.

Technique	T_c [K]	Direction [deg]	n	$2\kappa/n$	κ	α [nm ⁻¹]	d [nm]	ϵ_1	ϵ_2
Brillouin Spectroscopy [Present Work]	78	10		0.21(1)	↓	0.0050(2)	202(10)	3.96(2)	0.84(4)
		14		0.29(1)	↓	0.0068(2)	146(5)	3.92(2)	1.16(4)
		19		0.19(1)	↓	0.0044(2)	229(12)	3.96(2)	0.76(4)
		23		0.26(2)	↓	0.0061(5)	163(13)	3.93(4)	1.04(8)
		24		0.26(1)	↓	0.0061(2)	163(6)	3.93(2)	1.04(4)
		26		0.28(1)	↓	0.0066(2)	151(5)	3.92(2)	1.12(4)
Optical Interference [9]	85	-	1.9	0.04	0.04	0.0009 ^c	1060 ^a	3.6 ^b	0.15 ^b
Optical Reflectance [10]	96		1.9	0.24	0.23	0.005 ^c	184 ^a	3.6 ^b	0.87 ^b
	69	~ 0	2.0	0.19	0.19	0.004 ^c	223 ^a	4.0 ^b	0.76 ^b
	60		2.1	0.25	0.26	0.006 ^c	163 ^a	4.3 ^b	1.1 ^b
Optical Reflectance-Ellipsometry [6]	-	~ 0	2.1 ^b	0.40	0.42 ^a	0.01 ^c	100	3.4	1.7

^a Estimated using $d = \lambda_i/4\pi\kappa$.

^b Estimated using $\epsilon_1 = n^2 - \kappa^2$, $\epsilon_2 = 2n\kappa$.

^c Estimated using $\alpha = 1/d$.

ing raw reflectance data for their samples. This work was partially funded by the Natural Sciences and Engineering Council of Canada (NSERC) through Discovery Grants to Andrews (#RGPIN-2015-04306) and LeBlanc (#RGPIN-2017-04253).

* tandrews@mun.ca

- [1] T. P. Sheahen, *Introduction to High Temperature Superconductivity*. (Kluwer Academic Publishers, 1994).
- [2] J. Kobayashi, T. Asahi, M. Sakurai, M. Takahashi, K. Okubo, and Y. Enomoto, *Phys. Rev. B* **53**, 11784 (1996).
- [3] J. Etrillard, Ph Bourges, H.F. He, B. Keimer, B. Liang, and C.T. Lin, *Europhys. Lett.* **55**, 201 (2001).
- [4] A. Yurgens, D. Winkler, T. Claeson, T. Murayama, and Y. Ando, *Phys. Rev. Lett.* **82**, 3148 (1999).
- [5] V. Bellini, C. Ambrosch-Draxl, and F. Manghi, *Mater. Sci. Eng. C* **23**, 885 (2003).
- [6] I. Bozovic, *Phys. Rev. B* **42**, 1969 (1990).
- [7] M. A. Quijada, D. B. Tanner, R. J. Kelley, M. Onellion, H. Berger, and G. Margaritondo, *Phys. Rev. B* **60**, 14917 (1999).
- [8] H. L. Liu, G. Blumberg, M. V. Klein, P. Guptasarma, and D. G. Hinks, *Phys. Rev. Lett.* **82**, 3524 (1999).
- [9] X. Wang, L. X. You, X. M. Xie, C. T. Lin, and M. H. Jiang, *J. Raman Spectrosc.* **43**, 949 (2012).
- [10] J. Hwang, T. Timusk, and G. D. Gu, *J. Condens. Matter Phys.* **19**, 125208 (2007).
- [11] M. G. Kanatzidis, R. Pöttgen, and W. Jeitschko, *Angew. Chem. Int. Edit.* **44**, 6996 (2005).
- [12] G. T. Andrews, A. M. Polomska, E. Vazsonyi, and J. Volk, *Phys. Stat. Sol. (a)* **204**, 1372 (2007).
- [13] J. R. Sandercock, *Solid State Commun.* **26**, 547 (1978).
- [14] M. Boekholt, J. V. Harzer, B. Hillebrands, and G. Güntherodt, *Physica C* **179**, 101 (1991).
- [15] A. M. Merritt, J.-P. Castellan, T. Keller, S.R. Park, J.A. Fernandez-Baca, G.D. Gu, and D. Reznik, *Phys. Rev. B* **100**, 144502 (2019).
- [16] H. W. Leidecker and J. T. LaMacchia, *J. Acoust. Soc. Am.* **43**, 143 (1968).
- [17] H. G. Danielmeyer, *J. Acoust. Soc. Am.* **47**, 331 (1970).
- [18] H. Boukari, E. D. Palik, and R. W. Gammon, *Appl. Opt.* **34**, 69 (1995).
- [19] C. Gigault and J. R. Dutcher, *Appl. Opt.* **37**, 3318 (1998).
- [20] J. R. Sandercock, *Phys. Rev. Lett.* **28**, 237 (1972).

5.2 Long-wavelength phonon dynamics in incommensurate $\text{Bi}_2\text{Sr}_2\text{CaCu}_2\text{O}_{8+\delta}$ crystals by Brillouin light scattering spectroscopy

In this section, we include the manuscript (and associated erratum) titled “Long-wavelength phonon dynamics in incommensurate $\text{Bi}_2\text{Sr}_2\text{CaCu}_2\text{O}_{8+\delta}$ crystals by Brillouin light scattering spectroscopy” presented in the journal Physical Review B (reference: PRB 106, 054113 (2022)). Reprinted with permission from authors B. D. E. McNiven, J. P. F. LeBlanc, and G. T. Andrews, and Physical Review B. Copyright (2022) by the American Physical Society.

Long-wavelength phonon dynamics in incommensurate $\text{Bi}_2\text{Sr}_2\text{CaCu}_2\text{O}_{8+\delta}$ crystals by Brillouin light scattering spectroscopy

B. D. E. McNiven , J. P. F. LeBlanc , and G. T. Andrews 

Department of Physics and Physical Oceanography, Memorial University of Newfoundland and Labrador, St. John's, Newfoundland & Labrador, Canada A1B 3X7

 (Received 4 February 2022; revised 12 July 2022; accepted 22 August 2022; published 31 August 2022; corrected 1 September 2022)

Room-temperature phonon dynamics in crystals of the high- T_c superconductor $\text{Bi}_2\text{Sr}_2\text{CaCu}_2\text{O}_{8+\delta}$ were probed using Brillouin light scattering spectroscopy. Six distinct bulk acoustic modes were observed and identified: two quasilongitudinal bulk modes and four quasitransverse bulk modes. A peak at a frequency shift of ~ 95 GHz with behavior reminiscent of an optic phonon was also observed in the spectra. The existence and nature of these modes is a manifestation of the incommensurate structure of $\text{Bi}_2\text{Sr}_2\text{CaCu}_2\text{O}_{8+\delta}$ and suggests that it may be categorized as a so-called composite incommensurate crystal comprised of two weakly interacting sublattices. A mass ratio of $m_1/m_2 = 2.8$ obtained from the two measured quasilongitudinal acoustic velocities led to sublattice assignments of $\text{Bi}_2\text{Sr}_2\text{O}_4$ and CaCu_2O_4 . Two surface acoustic modes were also observed in the spectra, the number and character of which suggest that the incommensurate structure in the near-surface region is disrupted due to microscopic-scale damage and/or the presence of defects. The Brillouin data also place an upper limit of ~ 10 GHz on the crossover frequency between commensurate and incommensurate phonon dynamics.

DOI: [10.1103/PhysRevB.106.054113](https://doi.org/10.1103/PhysRevB.106.054113)

I. INTRODUCTION

Quasiparticle dynamics in incommensurate systems are not well understood, with the scarcity of knowledge being particularly acute for long-wavelength acoustic phonons. While the “usual” phonon dispersion for a typical commensurate crystal consists of $3N-3$ optic and three acoustic phonon modes, where N is the number of atoms in the unit cell, theoretical studies predict modifications to the phonon dispersions of incommensurate crystals due to their unique structure [1–6]. Moreover, complementary experimental work on acoustic phonon dynamics in such systems is limited despite the fact that many have incommensurate phases at ambient temperatures, making them prime candidates for laboratory investigation. The crystalline form of high-temperature superconductor $\text{Bi}_2\text{Sr}_2\text{CaCu}_2\text{O}_{8+\delta}$ (Bi-2212) is one such material [7–9].

Experiments aimed at probing acoustic phonon dynamics in Bi-2212 reveal complex dispersion with branch crossings and the unexpected absence or presence of particular modes arising from the incommensurate structure. For example, inelastic neutron scattering results suggest that coupling of longitudinal acoustic phonons to electrons is limited to zone center phonons by branch anticrossings, and that low-energy spectral weight near a charge density wave ordering wave vector arises from an extra low-lying acoustic phonon branch emanating from a nearby superlattice modulation reflection [10]. Possibly consistent with this second suggestion is the observation of two (instead of the usual one) longitudinal acousticlike modes along the incommensurate direction in

another neutron scattering study [11]. Interestingly, only one longitudinal mode was measured in this direction in ultrasonic pulse-echo experiments conducted at 7.5 MHz [12]. These last two observations suggest an undiscovered crossover from two propagating longitudinal modes to one such mode in the 10 MHz–150 GHz frequency regime inaccessible to these two techniques. Furthermore, neutron scattering experiments conducted along the incommensurate direction in Bi-2212 detected only one transverse mode instead of the two that were expected [11]. Additionally, Ref. [10] indicates that multiple phonon branches beyond a normal limit can be expected for Bi-2212. Given that the GHz-frequency regime remains largely unexplored, it is likely that one or more of these branches could exist in this frequency range.

This paper reports on Brillouin light scattering experiments on high-quality single crystals of Bi-2212, the need for which has been repeatedly articulated in the literature [11,13]. By probing with sub-GHz resolution a frequency range inaccessible to ultrasonics and neutron scattering techniques, the results of this study provide insight into the dynamics of long-wavelength hypersonic phonons in Bi-2212. In particular, the incommensurate structure of Bi-2212 is manifested in the Brillouin spectrum through the presence of multiple acoustic phonon peaks in excess of those expected for a typical crystal. This observation places an upper limit of ~ 10 GHz on the “separate sublattice-to-standard single crystal” crossover frequency and suggests that Bi-2212 is more accurately described as a composite incommensurate crystal rather than a modulated incommensurate crystal. Moreover, quasilongitudinal phonon velocities determined in this work permit identification of the two sublattices that comprise the incommensurate Bi-2212 crystal. The damping-out, with increasing proximity to the incommensurate direction, of a previously

*tandrews@mun.ca

unreported low-lying opticlike mode at ~ 95 GHz may be another manifestation of the incommensurate character of Bi-2212. Based on the above observations, this Brillouin scattering study reveals the incommensurate nature of Bi-2212.

II. EXPERIMENTAL DETAILS

Brillouin spectroscopy is an inelastic laser light scattering technique used to probe thermally excited acoustic phonons in condensed-matter systems. In this technique, monochromatic light is directed at the sample of interest, and the light scattered in some predefined direction is frequency-analyzed. Depending upon the nature of the sample and the scattering geometry, the resulting spectrum may contain peaks due to surface, interface, film-guided, and/or bulk acoustic phonons in the target material at frequencies shifted from that of the incident light due to the inelastic nature of the scattering. Measurement of these peak shifts, which are typically in the GHz range, yield phonon velocities from which elastic moduli may be determined. Knowledge of Brillouin peak widths gives information on phonon attenuation and, in opaque materials like Bi-2212, optical constants [14]. Further details on the instrumentation and scattering geometries employed, the types of excitations probed, the methods used to facilitate mode identification, and the variety of systems that may be studied using this technique are provided in several comprehensive review articles [15–17].

Brillouin scattering experiments were performed at room temperature using a 180° backscattering geometry on (001)-oriented flakes of Bi-2212 exfoliated from three parent crystals with critical temperatures of 78, 90, and 91 K. Incident light was provided by a single-mode frequency-doubled Nd:YVO₄ laser emitting at a wavelength of $\lambda_i = 532$ nm. The beam was horizontally (“*p*”) polarized by use of a half-wave plate and then passed through neutral density filters to reduce the power at the sample to ~ 10 mW to minimize heating due to optical absorption. The scattered light was collected and collimated by a high-quality camera lens with an aperture setting of $f/2.8$ and subsequently focused onto the entrance pinhole of a six-pass tandem Fabry-Pérot interferometer using an $f = 40$ cm lens. The pinhole diameter was set to 300 or 450 μm , with the former being used when the central elastic peak width needed to be reduced to reveal Brillouin peaks at very small frequency shifts. A photograph and a schematic diagram of the complete setup used in these experiments are given in Ref. [18].

Brillouin spectra were collected for angles of incidence ranging from 10° to 75° , corresponding via Snell’s law to internal angles of refraction, and therefore probed phonon propagation directions, from $\sim 5^\circ$ to $\sim 29^\circ$ from the crystallographic *c*-axis. It was not possible to obtain spectra for angles of incidence $< 10^\circ$ due to the signal being swamped by intense reflected light.

III. RESULTS AND DISCUSSION

A. Brillouin spectra—General features

Figure 1 shows representative Brillouin spectra of three Bi-2212 crystals. Eight different Brillouin peak doublets (labeled *R*, *LR*, QT_i with $i = 1-4$, and QL_j with $j = 1-2$) are

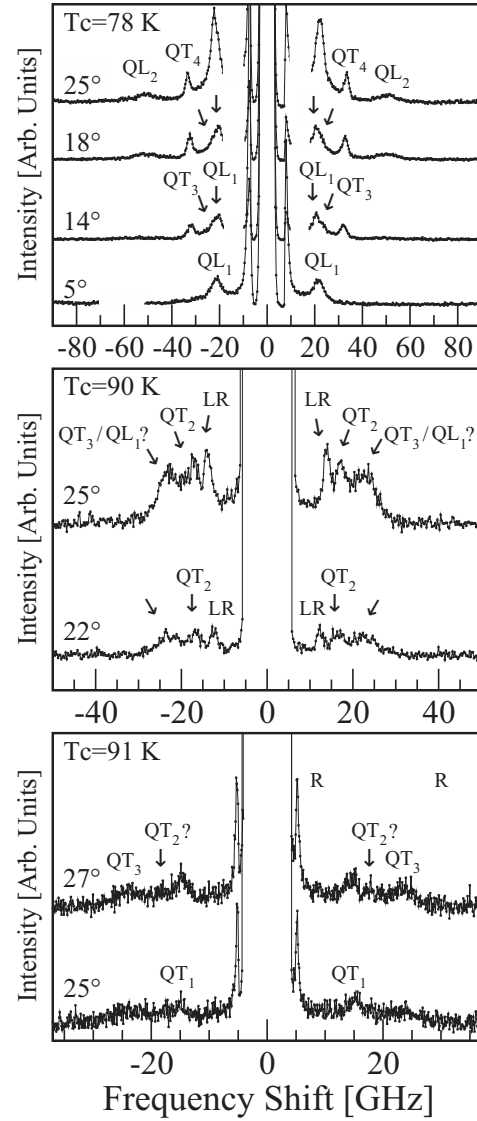


FIG. 1. Room-temperature Brillouin spectra of Bi-2212 crystals with $T_c = 78$ K (upper panel), 90 K (middle panel) and 91 K (lower panel) for phonon propagation directions as measured from the crystallographic *c*-axis. Eight acoustic modes are observed. *R*, surface Rayleigh; *LR*, longitudinal surface resonance; QT_i , quasitransverse; QL_i , quasilongitudinal. The $QT_3/QL_1?$ peak in the middle panel is labeled in this way because it is not clear if it is QT_3 or QL_1 due to the similarity in shifts. The assignment of the $QT_2?$ peak in the lower panel to the QT_2 mode is not definitive because, although it appears at the same shift as the QT_2 peak in the middle panel, it is barely discernible in the spectrum. Note: In the upper panel, QT_1 is omitted due to being overshadowed by a strong signal from sample mounting tape. The region near 60 GHz is omitted in the 5° spectrum due to a known experimental artefact. For all spectra shown in this figure, the incident light was *p*-polarized, and no polarizer was present in the scattered beam.

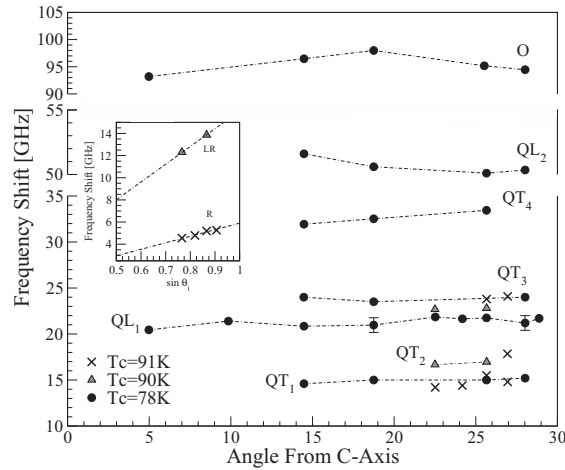


FIG. 2. Brillouin shift vs propagation direction for peaks due to bulk quasitransverse (QT_1 , QT_2 , QT_3 , and QT_4), quasilongitudinal (QL_1 , QL_2) acoustic phonon modes, and a low-lying optic mode (O). The inset shows the Rayleigh (R) and longitudinal surface resonance (LR) acoustic phonon modes fitted through the origin. Omitted error bars are approximately the size of the associated data point symbols.

present in the spectra, with the number and intensity of these modes varying with angle of incidence and from sample to sample. The overall quality of the spectra is strongly sample-dependent, with the $T_c = 78$ K sample giving those of the highest quality. In fact, spectra like those shown in the top panel of Fig. 1 were obtained on multiple flakes of this sample. Spectra obtained from the other two crystals are only of fair quality despite single-spectrum collection times of ≥ 20 h. These differences may be due to crystal quality effects possibly related to the growth method. In any case, the Brillouin spectra in this work are of the highest quality yet obtained for Bi-2212.

The directional dependence of the Brillouin peak frequency shifts is shown in Fig. 2. For the lowest angles of incidence (i.e., directions closest to the c -axis) only peak QL_1 is present in the spectra. At larger angles of incidence ($> 14^\circ$ from the c -direction), the R , LR , QT_1 , QT_2 , QT_3 , QT_4 , and QL_2 peaks appear in the spectra of one or more of the three samples. It is noted that the large width and asymmetry of the peak at ~ 21 GHz for the $T_c = 90$ K sample (the unlabeled peak indicated by arrows in the middle panel of Fig. 1) suggests that it may in fact be two closely spaced peaks due to the QT_2 and QL_1 modes, similar to what was observed for the $T_c = 78$ K sample (see the top panel of Fig. 1). With the exception of the R and LR peaks (see Fig. 2, inset), the peak shifts show only a small variation with propagation direction. This apparent lack of appreciable anisotropy is primarily an artefact of the relatively limited angular ranges probed, over which a large variation in shift is not expected. Variation in the peak frequency shift of similar magnitude over comparable ranges of angles from the crystallographic c -axis was observed for bulk acoustic modes in Brillouin scattering studies of several other layered materials including V_2O_5 [19], $CdPS_3$ [20], and muscovite mica [21]. Acoustic modes in some artificial hybrid

layered systems, however, can show substantial anisotropy over a relatively small range of directions [22].

B. Mode assignment

1. Surface acoustic phonon modes

The shifts of the peaks labeled R and LR show a strong linear dependence on the sine of the angle of incidence, and they are therefore assigned to the Rayleigh surface mode and longitudinal resonance, the latter being observed only in the spectra of the sample with $T_c = 90$ K. Accordingly, the velocities of these modes were determined by fitting the Brillouin equation for surface modes, $f_S = 2V_S \sin \theta_i / \lambda_i$, where V_S is the velocity of the Rayleigh mode ($S = R$) or the longitudinal resonance ($S = LR$), to the experimental frequency shift (f_S) versus $\sin \theta_i$ data. The velocities, determined from the slopes of the lines of best fit, were found to be $V_R = 1570 \pm 20$ m/s and $V_{LR} = 4260 \pm 40$ m/s for the $T_c = 91$ and 90 K samples, respectively, and they are comparable to those found in a previous Brillouin scattering study of Bi-2212 [23]. The widths of the R and LR peaks are also noticeably smaller than those of the other peaks, further supporting the assignment of these peaks to surface modes.

2. Bulk quasitransverse acoustic phonon modes

Peaks QT_1 , QT_2 , QT_3 , and QT_4 are assigned to quasitransverse acoustic modes because the shifts show little dependence on direction and because they are absent in small-angle spectra [24] and show an overall increase in intensity with increasing angle of incidence. Moreover, the frequency shifts of QT_1 and QT_3 are close to those of peaks identified as quasitransverse acoustic modes in previous Brillouin scattering experiments [23], although it is also possible that the peak identified as the fast quasitransverse mode in Ref. [23] is actually QL_1 due to its proximity to QT_3 , as shown in the top panel of Fig. 1. Further support for this mode assignment is provided by ultrasonics measurements on ceramic Bi-2212 samples with the c -axis of grains preferentially aligned, which give transverse mode velocities within $\leq 10\%$ of those of QT_1 and QT_2 (see Table I). Incidentally, the longitudinal acoustic mode velocity measured along the c -axis in the same study is also in excellent agreement with that of QL_1 determined in the present work [25].

It is also worth noting here that the close proximity of QT_2 and QT_3 to QL_1 (a range spanning ~ 6 GHz) could explain why inelastic neutron scattering experiments have consistently measured only one transverse acoustic mode [11], since that technique lacks the resolution necessary to resolve two peaks separated by only a few GHz.

3. Bulk quasilongitudinal acoustic phonon modes

The most surprising result of the present study is the presence of two distinct quasilongitudinal bulk mode peaks (QL_1 and QL_2) in the Brillouin spectrum of Bi-2212, neither of which was seen in previous Brillouin scattering studies [23,26,27]. The longitudinal character of these modes was confirmed by polarization analysis of the scattered light. To perform this analysis, it was first noted that for normally incident p -polarized light, the light scattered from longitudinal

TABLE I. Room-temperature transverse (V_{T_i}) and longitudinal (V_{L_i}) bulk acoustic phonon velocities along various directions for crystalline Bi-2212. V_L is the longitudinal acoustic phonon velocity in the $q \rightarrow 0$ limit determined by (i) ultrasonics or Brillouin scattering measurement, or (ii) Eq. (1) through knowledge of velocities V_{L_1} and V_{L_2} , and sublattice masses m_1 and m_2 , with use of the latter method indicated by a footnote. Note: V_{T_i} and V_{L_i} for the present Brillouin scattering studies refer to quasitransverse and quasilongitudinal velocities, respectively. Bulk phonon velocities determined in the present work have an associated $\sim 5\%$ uncertainty.

Technique	Study	T_c (K)	Direction	V_{T_1} (m/s)	V_{T_2} (m/s)	V_{T_3} (m/s)	V_{T_4} (m/s)	V_{L_1} (m/s)	V_{L_2} (m/s)	V_L (m/s)
Brillouin Light Scattering	Present work	78	5° from [001]							2700
			28° from [001]	1900		3200	4400	2700	6700	
		90	26° from [001]		2300					
		91	27° from [001]	2000	2400					
	Ref. [23] ^a	78–92	[001] [010]							3413 4380
Inelastic Neutron Scattering	Ref. [11]		[001]	1830						
			[010]					2400	5900	4700 ^e
Ultrasonic	Ref. [10] ^b		[001]	1780						2440
	Refs. [12,34] ^c	84.5	[010]		2460					4150
	Ref. [25] ^d		[001]	1750						2670
			In (001) plane	1740	2460					4370

^aEstimated from longitudinal resonance measurements, uncertainties are $\sim 5\%$.

^bEstimated from inelastic neutron scattering measurements at $T \leq T_c$.

^cEstimated from velocity vs temperature curves.

^dVelocities obtained from polycrystalline samples that show a preferred grain orientation.

^eEstimated from data in Ref. [11] substituted into Eq. (1).

and transverse bulk modes is p - and s -polarized, respectively [28]. Modes with longitudinal polarization will therefore be present in spectra for which the incident and scattered light are p -polarized (pp configuration) and absent when the incident light is p -polarized and the scattered light is s -polarized (ps configuration). Although it was not possible to obtain spectra for normally incident light, QL_1 was observed in pp -spectra obtained at an internal angle of incidence of 6° to the crystallographic c -axis, but not in the corresponding ps -spectra, verifying that it is a longitudinal mode (see Fig. 3). A similar result was obtained for QL_2 , but for an angle of 19° from the c -axis because this mode could not be readily observed at lower angles (see Figs. 1 and 2). It is noted that QL_1 is still visible but at reduced intensity in the 19° ps -polarized spectrum due to the fact that this mode has some transverse character for such general directions of propagation.

The fact that the QL_1 peak is quite intense in low incident angle spectra also supports its assignment to a quasilongitudinal acoustic mode because strong peaks due to quasitransverse modes are not expected to be present in Brillouin spectra under these circumstances [24]. Furthermore, the rather large shift of the QL_2 peak (~ 50 GHz) is consistent with this assignment.

4. Low-lying optic phonon mode

Figure 4 shows that the Brillouin spectra contain a weak peak at $\sim \pm 95$ GHz. The large frequency shift of this peak relative to others in the spectrum and the intensity difference between the Stokes and anti-Stokes scattering suggest that it

is due to an extremely low-lying optic phonon mode. As the right panel of Fig. 4 shows, this peak is strongest for phonon propagation directions close to the commensurate c -axis

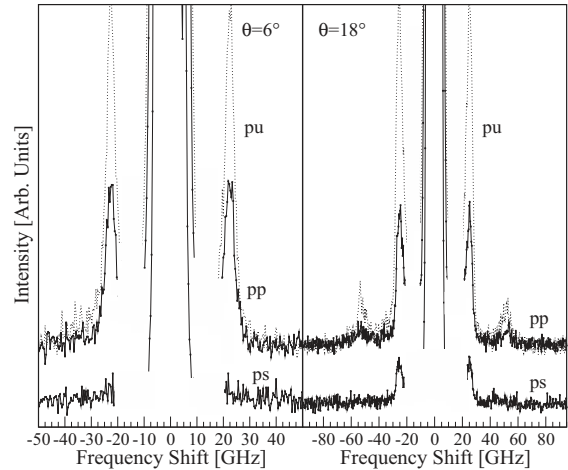


FIG. 3. Polarized spectra of a Bi-2212 crystal with $T_c = 78$ K. The notation “ XY ,” where $X, Y = u, p, s$, indicates the polarization state of the incident and scattered light, respectively. u, p , and s refer to unpolarized, p -polarized, and s -polarized light, respectively. Note: The spectral region inside 20 GHz was removed because it contained a strong signal from sample mounting tape.

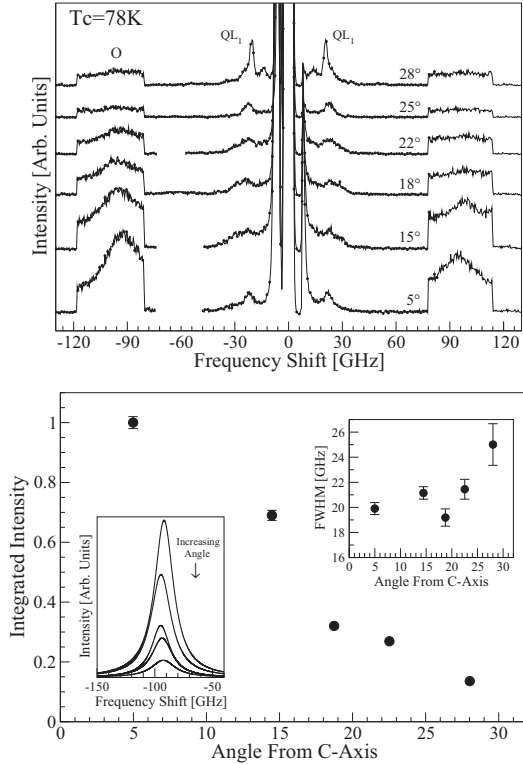


FIG. 4. Top panel: room-temperature Brillouin spectra of single-crystal Bi-2212. The region from $\sim \pm 80$ GHz to $\sim \pm 120$ GHz was segmented such that the collection time per channel in this region was $10\times$ that in the remainder of the spectrum. Note: to avoid confusion, portions of some spectra are omitted due to a known artefact at ~ 60 GHz. Bottom panel: integrated intensity of an apparent low-lying opticlike mode vs propagation direction as measured from the crystallographic c -axis. Left inset: peak intensity vs frequency shift for the same mode. Right inset: FWHM of low-lying opticlike mode.

(5° from the c -axis for $\theta_i = 10^\circ$) and becomes progressively less intense as the propagation direction moves away from this direction toward the ab -plane, being weakest at $\sim 28^\circ$ ($\theta_i = 70^\circ$) from the c -axis, the largest angle probed. This decrease in integrated intensity is accompanied by a corresponding decrease in peak intensity and an increase in peak width (FWHM), as seen in the left- and right-hand insets of Fig. 4, respectively. The peak frequency shift remains relatively constant over the range of directions probed, varying by a maximum of only 2–3 % from its mean value of 95.5 GHz (see Fig. 2). It was also noted that this peak appeared in both pp - and ps -spectra collected at angles of incidence very close to the c -axis ($<5^\circ$), suggesting that it is not due to a typical acoustic mode.

C. Incommensurate structure

The unusual Brillouin scattering results described above are a consequence of the incommensurate nature of Bi-2212. Surprisingly, this is the first time that the incommensurate

character of Bi-2212 has been observed in the Brillouin spectrum—previous studies make no mention of its incommensurate structure, nor are there any obvious signatures of it in published spectra. This is primarily because the spectral region beyond shifts of ± 30 GHz was not explored, but may also be related to recent improvements in crystal quality. As seen in Fig. 1, the presence of peaks in excess of those expected for a typical commensurate crystal is highly sample dependent and therefore may be a sensitive function of doping. In fact, the presence or absence of some optic phonon peaks in Raman spectra of Bi-2212 and other cuprate systems has been shown to depend on doping [29,30].

1. Signatures

The most striking manifestation of the incommensurate structure of Bi-2212 in the Brillouin spectrum is the presence of two peaks, QL_1 and QL_2 , due to quasilongitudinal modes. These peaks are both present in spectra for phonon propagation directions between $\sim 15^\circ$ and $\sim 28^\circ$ from the c -axis. In contrast, only QL_1 is present for propagation directions within $\sim 10^\circ$ of the commensurate c -direction (see Fig. 2). This can be explained by noting that for phonon propagation directions at relatively large angles to the c -axis, the projection of the probed phonon wave vector in the ab plane, and therefore the component of \vec{q} along the incommensurate b -direction, will be appreciable, resulting in the presence of spectral features due to the incommensurate nature of Bi-2212, including QL_2 . As the direction of probed phonon propagation approaches the c -axis, the b -component of \vec{q} approaches zero and the incommensurate nature is no longer apparent in the spectrum, accounting for the absence of QL_2 in small-angle spectra. The situation just described will be true unless, by coincidence, \vec{q} happens to lie precisely in the ac plane, in which case the b -component will be zero. This is, however, extremely unlikely.

The presence of two quasilongitudinal modes due to incommensurate structure in Brillouin spectra of Bi-2212 is consistent with the results of neutron scattering studies in which two longitudinal acoustic modes were observed along the incommensurate b -direction in Bi-2212 and Bi-2201 [11,13]. As Table I shows, the velocities of these modes for Bi-2212 were found to be 2400 and 5900 m/s, and they are comparable in magnitude to, and in the same ratio as, the velocities of the QL_1 and QL_2 modes (2700 ± 100 and 6700 ± 300 m/s at 28° from the c -axis, the closest direction to the b -axis probed; calculated using $V_B = f_B \lambda_i / 2n$, where B refers to bulk and $n = 2.0 \pm 0.1$ at 532 nm, where the estimated uncertainty was taken as the spread in published refractive index values of $1.9 \leq n \leq 2.1$ [31–33]). The fact that the velocities determined in the neutron scattering experiments are lower than those of QL_1 and QL_2 may seem counterintuitive given that the magnitudes of the latter are partially determined by the elastic constant(s) associated with the weak interlayer bonding in Bi-2212. This can be reconciled by noting both the lower resolution of neutron scattering in the $q \rightarrow 0$ limit when compared to Brillouin scattering, and the fact that it probes acoustic phonons at much higher q values where the velocity is typically expected to be lower due to a reduction in dispersion curve slope with increasing q . This

potential for the pertinent analytical techniques to measure different velocity values for a given mode due to changes in dispersion curve slope was also highlighted in Ref. [6]. Underestimation of refractive index n could also contribute to the Brillouin scattering velocities being larger than those obtained by neutron scattering. A refractive index that is 5% higher than that used here (i.e., 2.1 instead of 2.0, as dictated by the uncertainty of 0.1) would give Brillouin velocities V_B that are $\sim 5\%$ lower and therefore closer to those measured by inelastic neutron scattering [11].

A second signature of the incommensurate structure of Bi-2212 is the existence of four distinct QT modes for some propagation directions (see Fig. 2). The observation of twice as many QT peaks (i.e., two sets of 2 QT peaks) as would be expected for a commensurate crystal makes sense because of the two different periodicities associated with the incommensurate structure of Bi-2212. This reasoning also explains nicely the presence of two QL peaks in the Bi-2212 spectrum instead of the lone QL peak normally observed in the spectrum of a commensurate crystal.

The behavior of the low-lying optic mode may also be a consequence of the incommensurate structure of Bi-2212. The trends in integrated intensity, peak intensity, FWHM, and peak frequency shift described above (see Sec. III B 4) collectively suggest that the incommensurate structure of Bi-2212 causes this mode to be damped out. This reasoning may also explain why this mode is not observed in studies for which the primary or sole focus is phonon dynamics in the vicinity of the incommensurate b -direction.

The observation of a single Rayleigh surface mode peak (R) and a single longitudinal surface resonance peak (LR) in the Brillouin spectra suggests that the Bi-2212 surface does not possess incommensurate structure. Consistent with this conclusion is that both of these modes have velocities that are quite similar to those obtained in previous Brillouin studies of Bi-2212 for which no incommensurability was observed [23], and in the case of the LR mode, a velocity ($V_{LR} = 4260$ m/s) that is nearly identical to the $q \rightarrow 0$ limit velocity obtained by ultrasonics along the incommensurate direction ($V_L = 4150$ m/s [12,34]), and quite different from V_{QL_1} or V_{QL_2} (see Table I). The reason for the absence of incommensurate surface structure is not known, but it may be that the pristine incommensurate structure that exists in the bulk of the crystal is disturbed in the near-surface region due to microscopic-scale roughness and/or damage, effects to which Brillouin scattering is highly sensitive [35]. In fact, an early Brillouin study on crystalline Bi-2212 for which no signatures of incommensurability were observed notes the presence of surface roughness and points to it as a major contributor to poor spectrum quality [26]. It is also conceivable that adsorbed contaminants could be responsible for disrupting the incommensurate structure at the surface, although this seems unlikely given that one R peak rather than a set of two was observed in He-atom scattering spectra of Bi-2212 crystal surfaces prepared by cleaving under UHV conditions [36].

2. Consistency with the composite incommensurate crystal model

The existence of two sets of three acoustic phonon modes [$2 \times (1 QL + 2 QT)$] suggests that Bi-2212 may be categorized

as a composite incommensurate crystal, a class of aperiodic crystal in which the incommensurability arises from interpenetrating, mutually incommensurate sublattices [37] and for which, in contrast to modulated incommensurate crystals, an average periodicity cannot be defined [2]. This result also suggests that the two sublattices that comprise Bi-2212 are weakly interacting. In fact, two independent sets of phonon branches are observed in a model consisting of two interpenetrating atomic chains of different periods when there is no coupling between the chains [2]. Moreover, while there do not appear to be any explicit theoretical or experimental results on acoustic phonon dispersion in composite incommensurate crystals for general phonon propagation directions, the results obtained in the present work do bear some similarities to the results of previous studies of acoustic phonon dynamics in high-symmetry directions in Bi-2212. In particular, the presence of two distinct longitudinal acoustic modes is consistent with the predictions of the incommensurate composite model and also with inelastic neutron scattering results [11,13].

Knowledge of the sublattice velocities V_{QL_1} and V_{QL_2} makes it possible to identify the composition of the two sublattices via their estimated mass ratio [38],

$$\frac{m_1}{m_2} = \frac{V_{QL_2}^2 - V_{q \rightarrow 0}^2}{V_{q \rightarrow 0}^2 - V_{QL_1}^2}, \quad (1)$$

where $V_{q \rightarrow 0}$ velocity is the longitudinal mode velocity in the $q \rightarrow 0$ limit, and m_i and V_{QL_i} , $i = 1, 2$, are the mass and quasilongitudinal velocity of the i th sublattice, respectively. Given that ultrasonic experiments measure only a single longitudinal velocity equal to 4150 m/s in the MHz range in the incommensurate b -direction [12,34], this velocity can be taken as $V_{q \rightarrow 0}$. Using this, along with $V_{QL_1} = 2700 \pm 100$ m/s and $V_{QL_2} = 6700 \pm 300$ m/s in Eq. (1), gives $m_1/m_2 = 2.8 \pm 0.5$. While the relatively large uncertainty in m_1/m_2 permits a number of possible sublattice pair candidates, that of $\text{Bi}_2\text{Sr}_2\text{O}_4$ with mass 658 u and CaCu_2O_4 with mass = 232 u (neglecting δ) gives $m_1/m_2 = 2.8$, in excellent agreement with the value obtained from Eq. (1). This result is nearly a factor of 2 larger than the value of $m_1/m_2 = 1.5$ obtained in neutron scattering studies, which led to sublattice assignments of $\text{Bi}_2\text{SrO}_{2+\delta}$ and $\text{SrCaCu}_2\text{O}_6$ [11].

3. Crossover frequency

Figure 5 schematically shows the relatively low- q portion of the acoustic phonon dispersion (low-lying optic mode not shown) for Bi-2212 for a general propagation direction as informed by collective consideration of ultrasonics [12,34], inelastic neutron scattering [11], and current Brillouin scattering data. At very small q , as probed by ultrasonic techniques at frequencies of ~ 10 MHz, two transverse modes and a single longitudinal mode (QT_1 , QT_2 , and QL_1) would be observed as for a typical commensurate crystal. That this is the case can be inferred from the ‘‘Ultrasonics’’ data at the bottom of Table I. At a critical wave vector, q_c , higher than has been probed in ultrasonics experiments, there is a crossover from three to six propagating bulk acoustic modes due to the incommensurate structure of Bi-2212. These six modes are those observed in the present Brillouin scattering study, which probed phonons with a q -value greater than q_c and

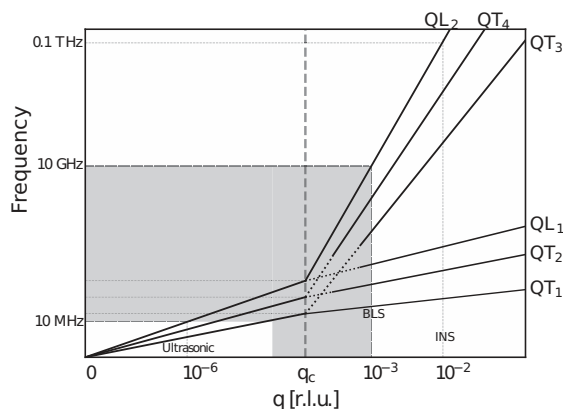


FIG. 5. Simplified schematic representation of low- q acoustic phonon dispersion for Bi-2212 for a general direction of propagation. q_c is the wave vector corresponding to the crossover frequency between commensurate and incommensurate dynamics. Approximate values of phonon wave vectors (q) in r.l.u. are shown for ultrasonic, Brillouin, and neutron scattering experiments.

with frequencies on the order of ~ 10 GHz. The frequency(ies) at which the crossover occurs therefore lie(s) in the range 10 MHz–10 GHz, one to four orders of magnitude higher than the value of ~ 1 MHz predicted by theory for the crossover from one to two propagating longitudinal acoustic modes in the Hg-chain compounds $\text{Hg}_{3+\delta}\text{AsF}_6$, the only composite incommensurate crystal system for which an estimate of crossover frequency has been provided [38]. Intuitively, one might expect an analogous crossover at comparable frequencies for quasitransverse modes, but this does not seem to be discussed in the literature. Inelastic neutron scattering accesses phonons with still higher q values in the $q > q_c$ region but with lower frequency resolution than Brillouin spectroscopy. While there do not appear to be any measure-

ments for directions other than along crystallographic axes, two longitudinal phonons were observed in the incommensurate b -direction in neutron scattering experiments on Bi-2212 [11], consistent with the scheme shown in Fig. 5. One of the consequences of the lower resolution, however, is that modes that are closely spaced in frequency may not be resolved in neutron scattering experiments. This could explain the absence of otherwise anticipated modes in previous neutron scattering studies of Bi-2212 [11].

IV. CONCLUSION

In summary, low-frequency phonon dynamics of Bi-2212 single crystals were studied using Brillouin light scattering spectroscopy. From collected spectra, two quasilongitudinal acoustic and four quasitransverse acoustic phonon modes were observed, with the former in agreement with previous inelastic neutron scattering studies [11] indicating that Bi-2212 is a composite incommensurate crystal. The measured frequency shifts of the six bulk acoustic phonon modes allowed for the assignment of each mode to a given sublattice, while the quasilongitudinal acoustic phonon velocities were used to propose sublattice assignments of $\text{Bi}_2\text{Sr}_2\text{O}_4$ and CaCu_2O_4 . Furthermore, a low-lying opticlike mode was also observed and appears to be another manifestation of the incommensurate nature of Bi-2212. The rich and highly unusual Brillouin spectra obtained here make it clear that further attention is warranted to fully understand phonon behavior in Bi-2212 in the $q \rightarrow 0$ limit. Moreover, the insights into long-wavelength phonon dynamics revealed in the current work will lead to a deeper understanding of the role of phonons and of electron-phonon coupling in high- T_c superconductivity.

ACKNOWLEDGMENT

The authors would like to acknowledge J. P. Clancy, Department of Physics and Astronomy, McMaster University, Canada, for supplying the samples used in this work.

- [1] J. D. Axe and P. Bak, *Phys. Rev. B* **26**, 4963 (1982).
- [2] R. Currat, E. Kats, and I. Luk'yanchuk, *Eur. Phys. J. B* **26**, 339 (2002).
- [3] M. Dzugutov and J. Phillips, *J. Non-Cryst. Solids* **192–193**, 397 (1995).
- [4] W. Finger and T. M. Rice, *Phys. Rev. Lett.* **49**, 468 (1982).
- [5] T. Janssen, O. Radulescu, and A. N. Rubtsov, *Eur. Phys. J. B* **29**, 85 (2002).
- [6] O. Radulescu, T. Janssen, and J. Etrillard, *Eur. Phys. J. B* **29**, 385 (2002).
- [7] P. Miles, S. Kennedy, G. McIntyre, G. Gu, G. Russell, and N. Koshizuka, *Phys. C: Supercond.* **294**, 275 (1998).
- [8] X. B. Kan and S. C. Moss, *Acta Cryst. B* **48**, 122 (1992).
- [9] D. Ariosa, H. Berger, T. Schmauder, D. Pavuna, G. Margaritondo, S. Christensen, R. Kelley, and M. Onellion, *Phys. C: Supercond.* **351**, 251 (2001).
- [10] A. M. Merritt, J.-P. Castellán, T. Keller, S. R. Park, J. A. Fernandez-Baca, G. D. Gu, and D. Reznik, *Phys. Rev. B* **100**, 144502 (2019).
- [11] J. Etrillard, Ph. Bourges, H. F. He, B. Keimer, B. Liang, and C. T. Lin, *Europhys. Lett.* **55**, 201 (2001).
- [12] Y. Wang, J. Wu, J. Zhu, H. Shen, Y. Yan, and Z. Zhao, *Physica C* **162–164**, 454 (1989).
- [13] J. Etrillard, L. Bourges, B. Liang, C. T. Lin, and B. Keimer, *Europhys. Lett.* **66**, 246 (2004).
- [14] B. D. E. McNiven, J. P. F. LeBlanc, and G. T. Andrews, *Supercond. Sci. Technol.* **34**, 065005 (2021).
- [15] J. R. Sandercock, in *Light Scattering in Solids III*, edited by M. Cardona and G. Guntherodt (Springer, Berlin, 1982), Chap. 6, pp. 173–206.
- [16] S. Speziale, H. Marquardt, and T. S. Duffy, *Rev. Min. Geochem.* **78**, 543 (2014).
- [17] J. G. Dil, *Rep. Prog. Phys.* **45**, 285 (1982).
- [18] G. T. Andrews, in *Handbook of Porous Silicon*, edited by L. Canham (Springer International, 2018), Chap. 53, pp. 691–703.
- [19] B. W. Reed, V. Huynh, C. Tran, and K. J. Koski, *Phys. Rev. B* **102**, 054109 (2020).

- [20] B. W. Reed and K. J. Koski, *J. Appl. Phys.* **131**, 165109 (2022).
- [21] L. E. McNeil and M. Grimsditch, *J. Phys.: Condens. Matter* **5**, 1681 (1993).
- [22] Z. Wang, K. Rolle, T. Schilling, P. Hummel, A. Philipp, B. A. F. Kopera, A. M. Lechner, M. Retsch, J. Breu, and G. Fytas, *Angew. Chem. Int. Ed.* **59**, 1286 (2020).
- [23] M. Boekholt, J. V. Harzer, B. Hillebrands, and G. Güntherodt, *Physica C* **179**, 101 (1991).
- [24] C. E. Bottani and D. Fioretto, *Adv. Phys. X* **3**, 607 (2018).
- [25] F. Chang, P. J. Ford, G. A. Saunders, L. Jiaqiang, D. P. Almond, B. Chapman, M. Cankurtaran, R. B. Poeppel, and K. C. Goretta, *Supercond. Sci. Technol.* **6**, 484 (1993).
- [26] P. Baumgart, S. Blumenröder, A. Erle, B. Hillebrands, P. Splittgerber, G. Güntherodt, and H. Schmidt, *Physica C* **162–164**, 1073 (1989).
- [27] V. V. Aleksandrov1, T. S. Velichkina, V. I. Voronkova, A. A. Gippius, S. V. Rek'ko, I. A. Yakovlev, and V. K. Yanovskii, *Solid State Commun.* **76**, 685 (1990).
- [28] H. Z. Cummins and P. E. Schoen, in *Laser Handbook*, edited by F. T. Arecchi, E. O. Schulz-Dubois, and M. L. Stitch (North-Holland, New York, 1972) Chap. E1, Vol. 2, pp. 1029–1075.
- [29] S. Benhabib, Y. Gallais, M. Cazayous, M.-A. Méasson, R. D. Zhong, J. Schneeloch, A. Forget, G. D. Gu, D. Colson, and A. Sacuto, *Phys. Rev. B* **92**, 134502 (2015).
- [30] P. E. Sulewski, P. A. Fleury, and K. B. Lyons, in *Laser Optics of Condensed Matter: The Physics of Optical Phenomena and Their Use as Probes of Matter*, edited by E. Garmire, A. A. Maradudin, and K. K. Rebane (Springer, Boston, 1991), Vol. 2, pp. 121–130.
- [31] J. Hwang, T. Timusk, and G. Gu, *J. Phys.: Condens. Matter* **19**, 125208 (2007).
- [32] X. Wang, L. X. You, X. M. Xie, C. T. Lin, and M. H. Jiang, *J. Raman Spectrosc.* **43**, 949 (2012).
- [33] I. Bozovic, *Phys. Rev. B* **42**, 1969 (1990).
- [34] Y. N. Wang, J. Wu, J. S. Zhu, H. M. Shen, J. Z. Zhang, Y. F. Yang, and Z. X. Zhao, in *Beijing International Conference on High Temperature Superconductivity*, edited by Z. X. Zhao, G. J. Cui, and R. S. Han (World Scientific, Beijing, 1989), Vol. 22, pp. 426–429.
- [35] S. Sathish, M. Mendik, A. Kulik, G. Gremaud, and P. Wachter, *Appl. Phys. Lett.* **59**, 167 (1991).
- [36] U. Paltzer, D. Schmicker, F. W. de Wette, U. Schroder, and J. P. Toennies, *Phys. Rev. B* **54**, 11989 (1996).
- [37] O. Radulescu and T. Janssen, *J. Phys. A* **30**, 4199 (1997).
- [38] W. Finger and T. M. Rice, *Phys. Rev. B* **28**, 340 (1983).

Correction: The last sentence of the first paragraph in Sec. III A contained a copyediting error and has been set right.

Erratum: Long-wavelength phonon dynamics in incommensurate $\text{Bi}_2\text{Sr}_2\text{CaCu}_2\text{O}_{8+\delta}$ crystals by Brillouin light scattering spectroscopy [Phys. Rev. B **106, 054113 (2022)]**B. D. E. McNiven , J. P. F. LeBlanc, and G. T. Andrews

(Received 22 June 2023; published 12 July 2023)

DOI: [10.1103/PhysRevB.108.019901](https://doi.org/10.1103/PhysRevB.108.019901)

Subsequent experiments have revealed that the peak observed at ~ 95 GHz in the Brillouin spectrum of $\text{Bi}_2\text{Sr}_2\text{CaCu}_2\text{O}_{8+\delta}$ is an artifact of the experimental apparatus and not due to an “opticlike” phonon mode as reported. As a result, the following content should be struck from the paper:

- (1) The third sentence in the Abstract.
- (2) The second sentence in Sec. I.
- (3) The data labeled “O” in Fig. 2 and the associated text that refers to these data in the figure caption.
- (4) The entirety of Sec. III B. 4. *Low-lying optic phonon mode*.
- (5) The peak doublet labeled “O” in the top panel of Fig. 4 and the entire bottom panel of Fig. 4.
- (6) The second paragraph of Sec. III C. 1. *Signatures*.
- (7) The fourth sentence in Sec. IV.

This change does not impact the other results nor the conclusions drawn in the paper.

5.3 Influence of incommensurate structure on the elastic constants of crystalline $\text{Bi}_2\text{Sr}_2\text{CaCu}_2\text{O}_{8+\delta}$ by Brillouin light scattering spectroscopy

In this section, we include the manuscript presented in Materials Research Express 10 (2), 026001 (2023) with permission from the authors B. D. E. McNiven, J. P. F. LeBlanc, G. T. Andrews, and IOP Publishing.

Materials Research Express



OPEN ACCESS

RECEIVED
21 November 2022REVISED
23 December 2022ACCEPTED FOR PUBLICATION
6 February 2023PUBLISHED
14 February 2023Original content from this work may be used under the terms of the [Creative Commons Attribution 4.0 licence](https://creativecommons.org/licenses/by/4.0/).

Any further distribution of this work must maintain attribution to the author(s) and the title of the work, journal citation and DOI.



PAPER

Influence of incommensurate structure on the elastic constants of crystalline $\text{Bi}_2\text{Sr}_2\text{CaCu}_2\text{O}_{8+\delta}$ by Brillouin light scattering spectroscopy

B D E McNiven , J P F LeBlanc and G T Andrews

Department of Physics and Physical Oceanography, Memorial University of Newfoundland, St. John's, Newfoundland & Labrador, A1B 3X7, Canada

E-mail: tandrews@mun.ca

Keywords: Bi-2212, brillouin light scattering, elastic constants, incommensurate structure, acoustic phonons, cuprates

Abstract

Brillouin light scattering spectroscopy was used to probe the room-temperature elasticity of crystalline high- T_c superconductor $\text{Bi}_2\text{Sr}_2\text{CaCu}_2\text{O}_{8+\delta}$. A complete set of best-estimate elastic constants was obtained using established relationships between acoustic phonon velocities and elastic constants along with a simple expression relating crystal elastic constant C_{22} to the corresponding constants of the constituent incommensurate sublattices. This latter relationship, which was derived and validated in the present work, has important implications for those studying incommensurate systems as it appears that it may be applied in its general form to any composite incommensurate crystal. The results obtained in this work are also consistent with sublattice assignments of $\text{Bi}_2\text{Sr}_2\text{O}_4$ and CaCu_2O_4 reported in a previous Brillouin scattering study.

1. Introduction

$\text{Bi}_2\text{Sr}_2\text{CaCu}_2\text{O}_{8+\delta}$ (Bi-2212) is one of the most intensely studied high- T_c superconductors yet its elastic properties have not been definitively characterized nor its acoustic phonon dynamics deeply probed. Early studies of Bi-2212 elasticity focused on the use of Brillouin light scattering spectroscopy and ultrasonics techniques to determine acoustic phonon velocities, room-temperature elastic moduli, and, in one case, a subset of the full set of elastic constants at selected temperatures between 80 K and 250 K [1–7]. Some elastic constants, however, remain unmeasured even under ambient conditions at room temperature and the values of others uncertain due to factors such as the nature of approximations employed, sub-optimal crystal quality, and, in the case of Brillouin studies, extremely weak signals and the apparent lack of a reliable refractive index value from which to determine bulk acoustic phonon velocities from spectral peak frequency shifts [6, 7]. Moreover, recent studies have uncovered interesting new acoustic phonon physics associated with the incommensurate structure of Bi-2212 [8–11], the investigation and understanding of which is in its infancy. In particular, Brillouin [8] and neutron scattering [9] studies revealed acoustic modes in excess of those expected for a typical commensurate crystal, calling into question mode assignments and consequently, elastic constants, reported in previous studies in which the incommensurability of Bi-2212 was not considered. Furthermore, while both of these studies find that Bi-2212 is better classed as a composite rather than a modulated incommensurate crystal, they differ in constituent sublattice assignments, the former suggesting $\text{Bi}_2\text{Sr}_2\text{O}_4$ and CaCu_2O_4 [8] and the latter, $\text{Bi}_2\text{SrO}_{2+\delta}$ and $\text{SrCaCu}_2\text{O}_6$ [9].

This paper describes a series of Brillouin light scattering experiments aimed at addressing the paucity of experimental data on the elasticity of crystalline Bi-2212. It does so by providing a set of best-estimate room-temperature elastic stiffness constants for crystalline Bi-2212 and its two constituent sublattices through the use of Brillouin peak frequency shift data and both established and newly-derived relationships between acoustic phonon velocities and elastic moduli.

By reporting first values for previously unmeasured elastic constants, correcting or confirming early published values of others, and establishing connections between the incommensurate structure and elastic properties, this work provides new insights into the elasticity and acoustic phonon dynamics of Bi-2212. The results deepen understanding of bonding in this material and in layered materials in general, but perhaps more importantly, aid in deciphering the role of electron-phonon coupling in high- T_c superconductivity and in the development and refinement of models of elasticity and acoustic phonon dynamics in incommensurate systems.

2. Experimental details

Brillouin scattering experiments were performed under ambient conditions using a backscattering geometry on (001)-oriented flakes of Bi-2212 obtained from three larger parent single crystals with T_c values of 78 K, 90 K, and 91 K. A single mode Nd:YVO₄ laser emitting at $\lambda = 532$ nm served as the incident light source. The laser beam was horizontally polarized using a half-wave plate and then passed through several attenuating filters to reduce the incident power to ~ 10 mW in order to avoid sample damage. It was then focused to a diameter of ~ 50 μm onto the sample using a $f = 5$ cm lens with $f/\# = 2.8$. This lens was also used to collect and collimate backscattered light, which was subsequently focused onto the entrance pinhole of a six-pass tandem Fabry–Perot interferometer by a $f = 40$ cm lens. Further details on the set-up used in these experiments are provided in [12].

Brillouin spectra were collected for light incident at angles ranging from $10^\circ \leq \theta_i \leq 75^\circ$ (corresponding to $\sim 5^\circ$ – 28° from the crystallographic c -axis) to the sample normal by rotating the sample about an axis normal to the plane of incidence as shown in [13]. Bulk acoustic phonon velocities, V_B , were determined directly from spectral peak frequency shifts using the well-known Brillouin equation $f_B = 2nV_B/\lambda$, where f_B is the bulk phonon frequency shift and $n = 2.0$ is the refractive index of Bi-2212 [14–16]. Surface acoustic mode velocities were extracted from linear fits of the Brillouin equation for surface modes, $f_R = 2V_R \sin \theta_i/\lambda$, to experimental shift (i.e. f_R) versus $\sin \theta_i$ data. In problematic cases in which two spectral peaks were very closely-spaced (e.g., QT_3 and QL_1), Lorentzian functions were fitted to the peaks to facilitate extraction of accurate frequency shift values. For all other peaks, the frequency shift was obtained directly from the spectra as the value of the abscissa associated with maximum intensity.

3. Results

3.1. Spectra

Figure 1 shows representative spectra for each of the three samples, with additional spectra being presented in figure 1 of [8]. In total, Brillouin peaks due to six distinct bulk acoustic phonon modes and two surface acoustic modes were observed. These peaks have previously been assigned to four quasi-transverse sublattice modes (QT_i , $i = 1 - 4$), two quasi-longitudinal sublattice modes (QL_1 and QL_2), the Rayleigh surface mode (R) and the longitudinal surface resonance (LR), the number and character of the bulk modes reflecting the incommensurate structure of Bi-2212 [8]. The incommensurate structure is not manifested in the surface modes for which only the R and LR peaks were observed. Moreover, the surface mode velocities V_R are nearly independent of direction of propagation in the ab -crystallographic plane, while the bulk mode velocities showed little dependence on propagation direction over the range probed (as measured by angle from the crystallographic c -axis) [8]. These velocities are presented in table 1.

3.2. Elastic constants

3.2.1. Influence of incommensurate structure

The elastic stiffness tensor for an incommensurate composite crystal with ‘average’ orthorhombic symmetry is given by

$$C_{ij} = \begin{pmatrix} C_{11} & C_{12} & C_{13} & 0 & 0 & 0 \\ C_{12} & C_{22} & C_{23} & 0 & 0 & 0 \\ C_{13} & C_{23} & C_{33} & 0 & 0 & 0 \\ 0 & 0 & 0 & C_{44} & 0 & 0 \\ 0 & 0 & 0 & 0 & C_{55} & 0 \\ 0 & 0 & 0 & 0 & 0 & C_{66} \end{pmatrix}. \quad (1)$$

Diagonal elastic constants C_{11} , C_{22} , C_{33} , C_{44} , C_{55} , and C_{66} can be determined directly from the density ρ and phonon velocities in high symmetry directions via the following expressions [17, 18]:

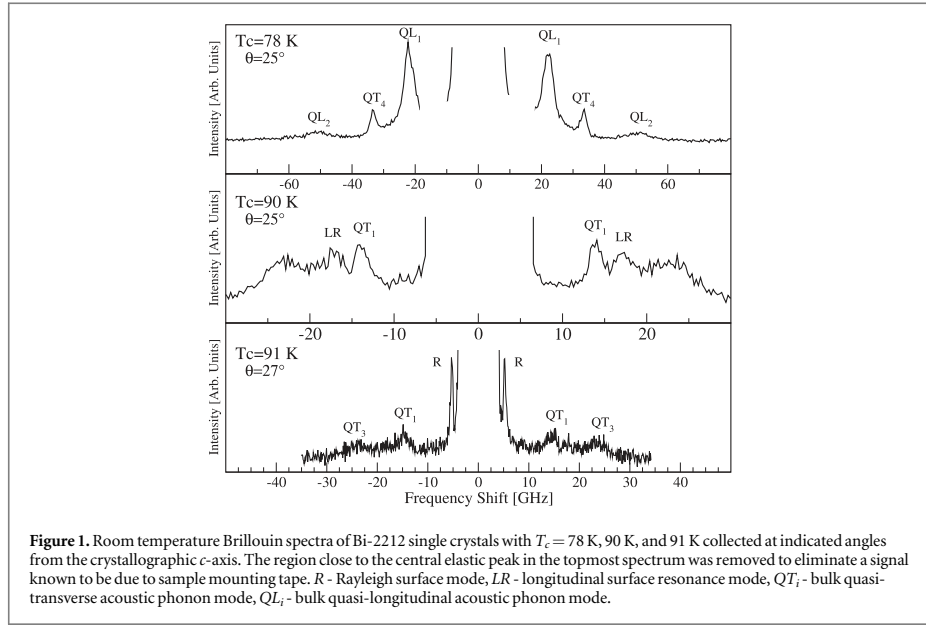


Table 1. Room-temperature surface and bulk phonon velocities (in m/s) for crystalline Bi-2212.

Note: (i) $V_{R(001)}$ is the average of Rayleigh mode velocities for crystals with $T_c = 90$ K and $T_c = 91$ K in the ab -plane; (ii) $V_{L[001]}$ is the velocity of a bulk longitudinal mode that propagated along a direction $\sim 5^\circ$ from the c -axis, while the remaining bulk mode velocities were measured for longitudinal modes that propagated at larger angles to this axis; (iii) bulk velocities are rounded to the nearest hundred due to an uncertainty of $\sim 5\%$. See [8] for further details.

$V_{R(001)}$	V_{LR}	V_{QT1}	V_{QT2}	V_{QT3}	V_{QT4}	V_{QL1}	V_{QL2}	$V_{L[001]}$
1590	4260	2000	2400	3200	4440	2700	6700	2700

$$\begin{aligned}
 C_{11} &= \rho(V_{L[100]}^{[100]})^2, \\
 C_{22} &= \rho(V_{L[010]}^{[010]})^2, \\
 C_{33} &= \rho(V_{L[001]}^{[001]})^2, \\
 C_{44} &= \rho(V_{TS[001]}^{[010]})^2 = \rho(V_{TS[010]}^{[001]})^2, \\
 C_{55} &= \rho(V_{TF[001]}^{[100]})^2 = \rho(V_{TF[100]}^{[001]})^2, \\
 C_{66} &= \rho(V_{TF[010]}^{[100]})^2 = \rho(V_{TF[100]}^{[010]})^2,
 \end{aligned} \tag{2}$$

where the subscript (superscript) denotes the propagation (polarization) direction and V_{TS} , V_{TF} and V_L are the slow transverse, fast transverse, and longitudinal acoustic phonon velocities, respectively.

In incommensurate composite crystals, at a critical wavevector q_c (or equivalently, a critical frequency f_c for each mode i), the bulk phonon dispersion exhibits a crossover from the familiar three-branch (TS , TF , and L) structure typical of a standard commensurate crystal to one containing multiple branches for each sublattice comprising the crystal. For the particular case of two sublattices, the longitudinal bulk acoustic mode velocity in the incommensurate direction for $q \ll q_c$ (i.e. the long-wavelength limit) is given by [19]

$$V_L^{q \rightarrow 0} = \left[\frac{m_A V_{L_A}^2 + m_B V_{L_B}^2}{m_A + m_B} \right]^{1/2}, \tag{3}$$

where m_α and V_{L_α} ($\alpha = A, B$), are the sublattice masses and longitudinal phonon velocities, respectively. This equation (equation (3)) has been used to determine $V_L^{q \rightarrow 0}$ of BSCCO crystals in neutron scattering [9, 20] and Brillouin light scattering [8] experiments for which the crossover frequency from commensurate to incommensurate acoustic phonon dynamics lies in the range $10 \text{ MHz} < f_c < 10 \text{ GHz}$ [8]. [19] implies that analogous relationships exist for transverse modes although these were not explicitly shown.

A particularly simple and useful relationship between crystal elastic constant C_{22} and the associated sublattice constants can be derived by recalling the fundamental equation relating elastic modulus to acoustic phonon velocity and mass density, $C = \rho V^2$. Substitution of this into equation (3) gives

$$C_{22} = \rho_A V_{L_A}^2 + \rho_B V_{L_B}^2 = C_{22}^A + C_{22}^B \quad (4)$$

where ρ_A and ρ_B are the sublattice densities $\rho_\alpha = \rho m_\alpha / (m_A + m_B)$ and V_{L_α} ($\alpha = A, B$) are sublattice longitudinal acoustic phonon velocities in the incommensurate direction. This result states that crystal elastic constant C_{22} is simply the sum of the corresponding sublattice constants C_{22}^A and C_{22}^B . Thus, for an incommensurate composite system with ‘average’ orthorhombic symmetry and incommensurate direction along the crystallographic b -axis as for Bi-2212, knowledge of the velocities V_{L_A} and V_{L_B} along with sublattice densities allows C_{22} to be determined.

3.2.2. C_{11} , C_{33} and C_{66}

Elastic constants C_{11} , C_{33} , and C_{66} were determined from the pertinent members of equation (2). To obtain C_{11} in this way, a value for $V_{L_{[100]}}^{[100]}$ is required. For practical reasons, however, this velocity could not be measured in the current experiments. Instead, the velocity of the surface LR mode (which is approximately equal to that of the bulk longitudinal mode [21]), $V_{LR} = 4260 \text{ m s}^{-1}$, in an unspecified direction on the (001) plane was used. The justification for this replacement is twofold: (i) the velocity of the LR mode is essentially independent of direction on the (001) plane [7] and thus the fact that the direction of propagation is not known is of no consequence, and (ii) the incommensurate structure of Bi-2212 is not manifested in the surface phonon dynamics and therefore surface phonons behave as they would in a typical commensurate crystal [8]. This yields $C_{11} = 120 \text{ GPa}$. By a similar process, but more straightforward substitution, $C_{33} = 48 \text{ GPa}$ was obtained directly from the third member of equation (2) using a velocity of 2720 m/s for a propagation direction very close ($< 5^\circ$) to the crystallographic c -axis for $V_{L_{[001]}}^{[001]}$. The final member of equation (2) gives $C_{66} = 40 \text{ GPa}$ with $V_{TF_{[010]}}^{[100]} = 2460 \text{ m/s}$ from ultrasonics experiments on crystalline Bi-2212 at 270 K [22] as this velocity was not measured in the present work. It is noted that for $270 \text{ K} < T < 290 \text{ K}$, the velocity of ultrasonic shear modes polarized and propagating in the ab -plane of quasi-crystalline Bi-2212 is nearly independent of temperature (a decrease of only $\sim 10 \text{ m/s}$ from 270 K to 290 K), suggesting that the room temperature value of $V_{TF_{[010]}}^{[100]}$ in crystalline Bi-2212, and therefore C_{66} , is not appreciably different from its value at 270 K . Moreover, extrapolation of the $V_{TF_{[010]}}^{[100]}$ versus temperature data for crystalline Bi-2212 [22] from $T > 255 \text{ K}$ to room temperature, results in essentially the same velocity, and therefore C_{66} value, as at 270 K due to its very weak temperature dependence.

3.2.3. C_{ii}^α and C_{22}

Sublattice constants $C_{ii}^\alpha = \rho_\alpha V_{X_\alpha}^2$, where $\alpha = A, B$ and $X = L, TS, TF$ for $i = 2, 4, 6$, respectively, were determined from sublattice densities ρ_α and the velocities of the appropriate QL_i and QT_i modes from table 1 for V_{X_α} . In particular, V_{QL_4} and V_{QL_2} are substituted for V_{L_A} and V_{L_B} , the slow-quasi-transverse sublattice velocities V_{QT_4} and V_{QT_2} are substituted for V_{TS_A} and V_{TS_B} and, lastly, the fast-transverse sublattice velocities V_{QT_6} and V_{QT_4} are substituted for V_{TF_A} and V_{TF_B} . The rationale for replacing the sublattice phonon velocities with V_{QT_i} and V_{QL_i} is provided in [8]. The sublattice densities $\rho_A = 4900 \pm 880 \text{ kg}\cdot\text{m}^{-3}$ and $\rho_B = 1700 \pm 300 \text{ kg}\cdot\text{m}^{-3}$ were determined from $\rho_\alpha = \rho m_\alpha / (m_A + m_B)$ using a Bi-2212 density of $\rho = 6600 \text{ kg}\cdot\text{m}^{-3}$ and sublattice assignments of $\text{Bi}_2\text{Sr}_2\text{O}_4$ and CaCu_2O_4 for which $m_A = 658 \text{ u}$ and $m_B = 232 \text{ u}$ [8]. Numerical values for the sublattice constants are provided in table 3.

As per equation (4), elastic constant $C_{22} = 112 \pm 24 \text{ GPa}$ was obtained by adding sublattice constants C_{22}^A and C_{22}^B . While similar expressions to determine shear moduli from sublattice constants are not available in the literature as noted in section 3.2.1 and, furthermore, are anticipated to be somewhat more complicated than that for C_{22} based on related calculations [19, 23], values for C_{44}^A , C_{44}^B , C_{66}^A , and C_{66}^B were computed based on the definition above and are provided in table 3 in the event that they prove useful.

3.2.4. C_{12} , $C_{4\phi}$, C_{23} and C_{55}

Estimates of C_{12} , C_{23} , C_{44} , and C_{55} were obtained from established relationships between select elastic constants and Rayleigh wave velocities V_R in high symmetry directions on particular crystal planes [24]. Specifically, these equations are:

$$\begin{aligned} & \sqrt{1 - \frac{\rho V_R^2}{C_{ii}} \left[1 - \frac{C_{jk}^2}{C_{jj} C_{kk}} - \frac{\rho V_R^2}{C_{jj}} \right]} \\ &= \sqrt{\frac{C_{ij}}{C_{kk}} \left[\frac{\rho V_R^2}{C_{jj}} \right]} \sqrt{1 - \frac{\rho V_R^2}{C_{jj}}} \end{aligned} \quad (5)$$

where the elastic constants subscripts for a particular direction of propagation and plane are given in table 2.

Table 3. Room-temperature elastic constants (in GPa) and sublattice constants of crystalline Bi-2212 obtained in the present work and in previous studies.

Technique/study	C_{11}	C_{22}	C_{33}	C_{44}	C_{55}	C_{66}	C_{12}	C_{13}	C_{23}	C_{22}^A	C_{22}^B	C_{44}^A	C_{44}^B	C_{66}^A	C_{66}^B
Brillouin scattering - Pres	120 ± 12	112 ± 24	48 ± 5	20 ± 2	20 ± 3	—	101 ± 16	44 ± 8	44 ± 8	36 ± 8	76 ± 16	19 ± 4	17 ± 4	25 ± 5	33 ± 7
Brillouin scattering [7]	125 ± 10	—	76 ± 9	16 ± 1	—	—	79 ± 7	56 ± 6	—	—	—	—	—	—	—
Ultrasonics [3, 22] ^a	134	114	—	—	—	40	—	—	—	—	—	—	—	—	—
Neutron scattering [11] ^b	—	—	39	—	—	—	—	—	—	—	—	—	—	—	—
Neutron scattering [9] ^c	—	—	—	—	—	—	—	—	—	15	139	—	—	—	—
Deformation Theory [25]	118	—	76	29	—	37	40	26	—	—	—	—	—	—	—
Deformation Theory [26]	119	—	72	27	—	40	40	27	—	—	—	—	—	—	—
Best Estimate	126 ± 11 ^d	113 ± 24 ^d	48 ± 5	20 ± 2	20 ± 3	40	101 ± 17	44 ± 8	44 ± 8	36 ± 8	76 ± 16	19 ± 4	17 ± 4	25 ± 5	33 ± 7

^a Determined by estimating $V_{L,T}$ at 270 K from velocity vs temperature curves in the quoted study.^b Obtained by fitting $\omega = qV_{L(001)}$ to experimental data provided in the quoted study.^c Estimated using velocities provided in the quoted study.^d Average of tabulated experimental values.

Table 2. Elastic constants, identifying subscripts (i, j, k), and Rayleigh mode velocities (V_R) in equation (5) for particular directions and planes of phonon propagation.

Direction	Plane	V_R [m/s]	i, j, k	Elastic constants appearing in equation (5)
[100]	(010)	1396 ^a	6, 1, 2	$C_{66}, C_{11}, C_{22}, C_{12}$
[001]	(010)	1508 ^a	4, 3, 2	$C_{44}, C_{33}, C_{22}, C_{23}$
[010]	(001)	1590	4, 2, 3	$C_{44}, C_{22}, C_{33}, C_{23}$
[100]	(001)	1590	5, 1, 3	$C_{55}, C_{11}, C_{33}, C_{13}$

^a From [7].

Substituting the values of C_{11} , C_{22} , C_{66} , and $V_{R[100]}^{(010)}$ into equation (5) with $i, j, k = 6, 1, 2$ yields $C_{12} = 102$ GPa. Moreover, C_{44} and C_{23} are solved for simultaneously via equations (5) with $i, j, k = 4, 3, 2$ and $i, j, k = 4, 2, 3$ using C_{22} , C_{33} , $V_{R[001]}^{(010)}$, and $V_{R(001)}$ from table 1 (noting the observed isotropy in the ab -plane [7, 8]), which yield 20 GPa and 44 GPa, respectively. Lastly, substituting C_{11} , C_{33} , and $V_{R(001)}$, into equation (5) with $i, j, k = 5, 1, 3$, and utilizing the approximation $C_{13} = C_{23}$, due to the fact that Bi-2212 is pseudo-tetragonal, gives $C_{55} = 20$ GPa.

4. Discussion

Table 3 shows the elastic constants obtained in the present work and in previous ultrasonics [3, 22] and Brillouin scattering [7] studies, as well as estimated values extracted from inelastic neutron scattering data [9, 11] and calculated values from deformation theory [25, 26]. Some of the elastic constants of the present work show excellent agreement with literature values while others are considerably different. A critical comparison of values is given below with the aims of providing a set of best-estimate room-temperature elastic constants for Bi-2212, establishing the validity of the simple model outlined in section 3.2.1, and evaluating the accuracy of the deformation theory calculations.

4.1. C_{11}, C_{22} : confirmation of published values

Elastic constants C_{11} and C_{22} agree with previously published results within experimental uncertainty. $C_{11} = 120 \pm 12$ GPa and $C_{22} = 112 \pm 24$ GPa lie within $\sim 4\%$ and $< 2\%$ of values obtained in previous Brillouin scattering [7] and ultrasonics experiments [3, 22], respectively. It is also noted that the excellent agreement between C_{11} of the present work and that reported in [7], both of which were determined from surface LR mode velocities, is consistent with the finding that effects arising from the incommensurate structure are not manifested in the surface acoustic phonon dynamics of Bi-2212 [8].

4.2. $C_{33}, C_{44}, C_{12}, C_{13}$: refinement of published values

Elastic constants C_{33} , C_{44} , and C_{12} of the current work differ considerably from published values. In particular, the values of C_{33} , C_{44} , and C_{12} are $\sim 35\%$ lower, $\sim 20\%$ higher, and $\sim 30\%$ higher than those reported in a previous Brillouin scattering study [7], respectively. Comparison of the available data suggests that the values of C_{33} , C_{44} , and C_{12} obtained in the current work most accurately reflect the true values of these constants.

In the present study, C_{33} was determined from the third member of equation (2) using a velocity calculated from the frequency shift of a well-defined spectral peak arising from a bulk QL mode propagating very nearly along [001]. The only other published value was that reported in a previous Brillouin study in which C_{33} was estimated to be 76 GPa using a surface LR mode velocity extracted from visibly lower quality spectra [7]. It is therefore likely that the value of $C_{33} = 48 \pm 5$ GPa obtained here more accurately reflects the true value of this constant. Consistent with this conclusion is $C_{33} \approx 40$ GPa from neutron scattering results on crystalline Bi-2212 in which the velocity was estimated by fitting $\omega = qV_L^{[001]}$ to a portion of the phonon dispersion curve constructed using data presented in figure 1(a) of [11]. Moreover, ultrasonics experiments on highly-textured ceramic Bi-2212 with preferred grain orientation (i.e. c -axis \perp sample surface plane) yielded $C_{33} = 44$ GPa [27].

The value of $C_{44} = 20 \pm 2$ GPa obtained from solving equations (5) simultaneously for C_{44} and C_{23} is in only fair agreement with the lone published experimental value of 16 GPa [7]. The latter, however, was determined using an approximation applicable to isotropic materials in which V_{TS} is replaced with V_R [7], and when used in equation (5) along with C_{22} , C_{33} , and $V_{R(001)}$, gives the unphysical result that C_{23} is complex.

The high quality of the data used in determining C_{12} via equation (5) suggests that the value obtained in the present study is an accurate measure of this constant despite it being considerably higher than that obtained in previous Brillouin scattering experiments [7]. More specifically, the accuracy of the values of C_{11} , C_{22} obtained here and used in equation (5) has been verified by independent measurements as described in section 4.1. The

value of C_{66} used in this equation, while not independently verifiable, was determined by straightforward calculation using the last member of equation (2) with the velocity from ultrasonics measurements that, while measured at 270 K, does not differ significantly from its room temperature value due to it being nearly independent of temperature over the range 270 K to 290 K [22, 27]. In addition, the Rayleigh mode velocity required by equation (5) was determined from a sharp, well-defined spectral peak resulting in a relatively low associated uncertainty [7]. Moreover, in [7], C_{12} was calculated from questionable values of C_{33} and C_{44} , as discussed in the preceding two paragraphs.

4.3. C_{55} , C_{23} , C_{66} : first values

The values of $C_{55} = 20$ GPa, $C_{23} = 44$ GPa and $C_{66} = 40$ GPa are the first reported for these elastic constants at room temperature. In the case of C_{55} and C_{23} , while there are no other published values to which to directly compare, one can invoke the fact that Bi-2212 is pseudo-tetragonal and compare to literature values of C_{44} and C_{13} , respectively, to make a semi-quantitative statement on their accuracy.

The value of C_{55} obtained in the current study is quite close to that of C_{44} , as expected for a pseudo-tetragonal system. Conversely, as mentioned above, $C_{23} = C_{13} = 44 \pm 8$ GPa. This value is $\sim 20\%$ smaller than that reported previously for C_{13} [7]. As stated above, the value of $C_{13} = 56$ GPa from [7] was determined using questionable values of $C_{33} = 76$ GPa and $C_{44} = 16$ GPa.

As described in detail in section 4.3, the value of $C_{66} = 40$ GPa should be robust as it was determined in a straightforward way from the last member of equation (2) using an ultrasonics measurement on crystalline Bi-2212 at 270 K of a shear mode velocity that is, with high probability, virtually independent of temperature over the range 270 K to 290 K. Moreover, use of this value in calculations highlighted in the previous section yield values for other elastic constants that are in good agreement with those obtained in previous work.

4.4. C_{ii}^{α} : sublattice elastic constants

Table 3 also reports sublattice elastic constants C_{ii}^{α} , ($i = 2, 4, 6$ and $\alpha = A, B$). These are the only such values explicitly available in the literature and therefore direct comparison with the results of other studies was not possible. Inspection of the C_{22}^A and C_{22}^B values obtained in the current work and those computed from available neutron scattering data [9], however, shows the former to be $\sim 250\%$ larger and $\sim 50\%$ smaller than the latter, respectively. This large discrepancy suggests that at least one C_{22}^A - C_{22}^B pair is incorrect. Cognizant of this, the C_{22}^A and C_{22}^B values of the present work were added according to the simple model given by equation (4) to yield $C_{22} = 112$ GPa. This value is within $\sim 4\%$ of a published value considered accurate [7]. In contrast, one obtains the seemingly unreasonably high value of $C_{22} = 154$ GPa if the sublattice longitudinal mode velocities and densities based on the sublattice assignments in neutron scattering studies [9] are used in equation (4). Use of V_{QL_1} and V_{QL_2} from the present work with the sublattice densities from neutron scattering studies in equation (4) gives an even higher value of $C_{22} = 199$ GPa.

4.5. Best estimates

The last row of table 3 contains the best estimates of the room temperature elastic constants of Bi-2212 based on the above comparative analysis. While most of the entries are those determined in the present work, the values of C_{11} and C_{22} obtained in the current study and in Refs.[3, 7, 22] were considered equally accurate and therefore the average of these appears in the last row.

The set of experimental best-estimate elastic constants in table 3 can be compared to those obtained via deformation theory [25, 26]. Remarkably, the calculated values of C_{11} and C_{66} are within $<10\%$ of the corresponding measured values. Conversely, the calculated and experimental values of C_{33} , C_{44} , C_{12} , and C_{13} are very different, possibly due to exclusion of incommensurate structure effects in the calculations.

4.6. Validity of composite incommensurate crystal model

The excellent agreement of elastic constant C_{22} , determined in this work by addition of the two associated sublattice constants, with a previously published value provides some measure of validation for the simple model outlined section 3.2.1, the foundation of which is equation (3). It also suggests that the sublattice assignment in [8] is correct. While an in-depth investigation is beyond the scope of this paper, intuitively, there appears to be no obvious reason why equations analogous to that used here to determine C_{22} (i.e. equation (4)) could not be derived for other incommensurate composite crystals provided due consideration is given to crystal symmetry and the incommensurate structure.

5. Conclusion

Brillouin light scattering experiments were performed on crystalline Bi-2212 at room-temperature yielding, through use of established and new relationships between phonon velocities and elastic moduli that take into account effects of incommensurate structure, a full set of best-estimate elastic constants and constituent sublattice constants. Elastic constant C_{22} , determined from the associated sublattice constants, showed remarkable agreement with a value obtained in previous work, providing support for the simple model linking this constant to sublattice constants and also for the sublattice assignment of $\text{Bi}_2\text{Sr}_2\text{O}_4$ and CaCu_2O_4 for Bi-2212 presented in [8]. The data obtained in the present work could serve as a second check of the validity of this model if expressions relating other (particularly, shear) elastic constants or phonon velocities to sublattice constants or velocities were available in the literature. More generally, the elastic constants presented in this work could aid in further development and refinement of models of elasticity and phonon dynamics in composite incommensurate systems. In particular, the lack of agreement between several measured elastic constants provided in the present study and available theoretical values highlights the importance of extending elasticity theory to accurately connect the elastic properties of composite incommensurate crystals to those of the constituent sublattices. A deeper understanding of the elastic properties and unusual acoustic phonon behaviour in Bi-2212 will also further understanding of electron-phonon coupling and bonding in layered cuprate superconductors and prove useful to those in the field of phonon engineering for the design and development of new acoustic and elasto/acousto-optic devices.

Acknowledgments

The authors would like to acknowledge Dr. J. P. Clancy at McMaster University, Canada, for supplying the samples used in this work. This work was partially funded by the Natural Sciences and Engineering Council of Canada (NSERC) through Discovery Grants to Andrews (#RGPIN-2015-04306) and LeBlanc (#RGPIN-2022-03882).

Data availability statement

All data that support the findings of this study are included within the article (and any supplementary files).

ORCID iDs

B D E McNiven  <https://orcid.org/0000-0003-3111-1419>

G T Andrews  <https://orcid.org/0000-0002-3152-2106>

References

- [1] Wu J, Wang Y, Guo P, Shen H, Yan Y and Zhao Z 1993 *Phys. Rev. B* **47** 2806
- [2] Wu J, Wang Y, Shen H and Zhu J 1990 *Phys. Lett. A* **148** 127
- [3] Wang Y, Wu J, Zhu J, Shen H, Yan Y and Zhao Z 1989 *Physica C* **162-164** 454
- [4] Saint-Paul M and Tholence J L 1990 *Physica C* **166** 405
- [5] Aleksandrov V V, Velichkina T S, Voronkova V I, Gippius A A, Rek'ko S V, Yakovlev I A and Yanovskii V K 1990 *Solid State Commun.* **76** 685
- [6] Baumgart P, Blumenröder S, Erle A, Billebrands B, Splittgerber P, Güntherodt G and Schmidt H 1989 *Physica C* **192-164** 1073
- [7] Boekholt M, Harzer J V, Hillebrands B and Güntherodt G 1991 *Physica C* **179** 101
- [8] McNiven B D E, LeBlanc J P F and Andrews G T 2022 *Phys. Rev. B* **106** 054113
- [9] Etrillard J, Bourges P, He H F, Keimer B, Liang B and Lin C T 2001 *Europhys. Lett.* **55** 201
- [10] He Y et al 2018 *Phys. Rev. B* **98** 035102
- [11] Merritt A M, Castellan J-P, Keller T, Park S R, Fernandez-Baca J A, Gu G D and Reznik D 2019 *Phys. Rev. B* **100** 144502
- [12] Andrews G T 2018 *Handbook of Porous Silicon* ed L Canham (Springer International) pp 691–703 Ch 53
- [13] McNiven B D E, LeBlanc J P F and Andrews G T 2021 *Supercond. Sci. Technol.* **34** 065005
- [14] Bozovic I 1990 *Phys. Rev. B* **42** 1969
- [15] Hwang J, Timusk T and Gu G 2007 *J. Phys. Condens. Matter* **19** 125208
- [16] Wang X, You L X, Xie X M, Lin C T and Jiang M H 2012 *J. Raman Spectrosc.* **43** 949
- [17] Mah M and Schmitt D R 2003 *J. Geophys. Res. Solid Earth, ECV* **108** 6
- [18] Auld B A 1973 *Acoustic Fields and Waves in Solids* vol 1 (New York: Wiley)
- [19] Finger W and Rice T M 1983 *Phys. Rev. B* **28** 340
- [20] Etrillard J, Bourges L, Liang B, Lin C T and Keimer B 2004 *Europhys. Lett.* **66** 246
- [21] Camley R E and Nizzoli F 1985 *J. Phys. C: Solid State Phys.* **18** 4795

- [22] Wang Y N, Wu J, Zhu J S, Shen H M, Zhang J Z, Yang Y F and Zhao Z X 1989 Ultrasonic study on anisotropic elasticity of $\text{Bi}_2\text{Sr}_2\text{CaCu}_2\text{O}_8$ single crystal *Beijing International Conference on High Temperature Superconductivity* vol 22 ed Z X Zhao *et al* (Beijing: World Scientific) pp 426–9
- [23] Axe J D and Bak P 1982 *Phys. Rev. B* **26** 4963
- [24] Stoneley R 1963 *Geophys. J. Int.* **8** 176
- [25] Jayachandran K P and Menon C S 2002 *J. Phys. Condens. Matter* **14** 59
- [26] Jayachandran K P and Menon C S 1999 *J. Phys. Chem. Solids* **60** 267
- [27] Chang F, Ford P J, Saunders G A, Jiaqiang L, Almond D P, Chapman B, Cankurtaran M, Poeppel R B and Goretta K C 1993 *Supercond. Sci. Technol.* **6** 484

Chapter 6

Conclusion

In this work, we studied high-temperature superconducting systems by experimental and numerical methods. Numerically, we studied the temperature and doping dependence on the static and dynamical charge and spin susceptibilities on the single-band 2D $t - t' - U$ Hubbard model on a square lattice in the weak coupling limit via diagrammatic perturbation theory. By varying particle-hole asymmetry through different choices of t' , we found the static susceptibilities have maxima at different densities and a strong dynamical change surrounding the van Hove singularity of the non-interacting problem, while additional calculations of the double occupancy and compressibility as functions of density showed the same behaviour. Moreover, calculations of the dynamical susceptibilities showed that for decreasing density approaching the van Hove singularity, there is a clear split in both branches, while the charge branch reforms and the spin branch remains split for densities less than this point.

Brillouin light scattering experiments at 532 nm were performed at room-temperature on three Bi-2212 samples with T_c values of 78 K, 90 K, and 91 K and identified eight acoustic phonon modes as the Rayleigh surface mode, two quasi-longitudinal bulk modes, four quasi-transverse bulk modes, and a longitudinal resonance mode. From the collected spectra, we analyzed the spectral line profiles and calculated each respective acoustic phonon velocity and determined the optical extinction and absorption coefficients, optical penetration depth, and the complex dielectric function. Due to the Bi-2212 phonon structure being strikingly similar to that expected in an incommensurate composite material, we calculated the long-wavelength longitudinal acoustic

phonon velocity from the two measured sublattice longitudinal modes and found excellent agreement with previous ultrasonic studies. Additionally, from analysis of the Brillouin spectra, we obtained mass ratios of the two sublattices which allowed for us to propose a sublattice assignment of $\text{Bi}_2\text{Sr}_2\text{O}_4$ and CaCu_2O_4 and their respective densities. Along with the calculated acoustic phonon velocities, these sublattice densities were used to calculate for the first time the sublattice elastic constants of Bi-2212, along with the elastic constants C_{11} , C_{22} , C_{33} , C_{44} , C_{55} , C_{12} , C_{13} , and C_{23} .

The combined numerical and experimental data presented in this thesis are of significant importance for many reasons. Firstly, our numerical data indicates that inelastic electronic experiments (such as Raman, neutron, and x-ray scattering) performed on overdoped high- T_c superconducting systems requires probing much higher energies when compared to underdoped systems. Secondly, data from our Brillouin scattering experiments which indicates Bi-2212 is comprised of two individual sublattices will be extremely useful for researchers studying the electronic structure of cuprates and those modelling high- T_c superconductivity as the presence of two individual sublattices will drastically alter the phonon structure and in turn coupling between electrons and phonons. Lastly, our experimental data on Bi-2212 will be of general use to those studying aperiodic crystallography as it can be used to fine tune currently employed aperiodic models.

Future work

There are several directions which could be pursued following this work. Experimentally, any additional data on general incommensurate compounds is highly valuable for the area of aperiodic crystallography as it can help refine future aperiodic models. Further, in the case of incommensurate cuprates, the incommensurate structure and its dependence on temperature should be investigated as it may hold key information regarding the unknown mechanisms behind high- T_c superconductivity. Lastly, studying the branch crossing regimes at smaller wavevectors using high-resolution light scattering techniques like Brillouin scattering would be very interesting as the phonon behaviour in these regions is still not understood.

From a theoretical perspective, repeating the dynamical susceptibility calculations

presented in this thesis which include electron-phonon interactions may prove interesting as it could give further insight regarding the role of phonons in high- T_c superconductivity. Moreover, the derivation of a function relating the sublattice and bulk transverse acoustic phonon velocities would be extremely useful in further developing the theory of incommensurate composite crystals.